



NRL Memorandum Report 6459

AD-A210 611

**Design and Operating Characteristics of a CW
Relevant Quasi-Optical Gyrotron with Variable
Mirror Separation**

A.W. FLIFLET, T.A. HARGREAVES,* W.M. MANHEIMER, R.P. FISCHER,
M.L. BARSANTI,** B. LEVUSH† AND T. ANTONSEN††

*High Power Electromagnetic Radiation Branch
Plasma Physics Division*

**Mission Research Corporation, Newington, VA*

***JAYCOR, Inc., Vienna, VA*

†University of Maryland, College Park, MD

*††Science Applications International Corporation, McLean, VA
also
University of Maryland, College Park, MD*

June 26, 1989

DTIC
ELECTF
JUL 28 1989
S B D
cb

REPORT DOCUMENTATION PAGE				Form Approved OMB No 0704-0188	
1. REPORT SECURITY CLASSIFICATION UNCLASSIFIED			1b. RESTRICTIVE MARKINGS		
2a. SECURITY CLASSIFICATION AUTHORITY			3. DISTRIBUTION / AVAILABILITY OF REPORT Approved for public release; distribution unlimited.		
2b. DECLASSIFICATION / DOWNGRADING SCHEDULE			5. MONITORING ORGANIZATION REPORT NUMBER(S)		
4. PERFORMING ORGANIZATION REPORT NUMBER(S) NRL Memorandum Report 6459			7a. NAME OF MONITORING ORGANIZATION		
6a. NAME OF PERFORMING ORGANIZATION Naval Research Laboratory		6b. OFFICE SYMBOL (If applicable) Code 4742	7b. ADDRESS (City, State, and ZIP Code)		
6c. ADDRESS (City, State, and ZIP Code) Washington, DC 20375-5000			9. PROCUREMENT INSTRUMENT IDENTIFICATION NUMBER		
8a. NAME OF FUNDING / SPONSORING ORGANIZATION Department of Energy		8b. OFFICE SYMBOL (If applicable)	10. SOURCE OF FUNDING NUMBERS		
8c. ADDRESS (City, State, and ZIP Code) Washington, DC 20545			PROGRAM ELEMENT NO	PROJECT NO	TASK NO
					WORK UNIT ACCESSION NO DN780-307
11. TITLE (Include Security Classification) Design and Operating Characteristics of a CW Relevant Quasi-Optical Gyrotron with Variable Mirror Separation					
12. PERSONAL AUTHOR(S) (See page ii)					
13a. TYPE OF REPORT		13b. TIME COVERED FROM 6/87 TO 3/89		14. DATE OF REPORT (Year, Month, Day) 1989 June 26	
				15. PAGE COUNT 88	
16. SUPPLEMENTARY NOTATION (See page ii)					
17. COSATI CODES			18. SUBJECT TERMS (Continue on reverse if necessary and identify by block number)		
FIELD	GROUP	SUB-GROUP	Gyrotron Quasi-optical Oscillator		
			Millimeter-wave tunable		
19. ABSTRACT (Continue on reverse if necessary and identify by block number)					
<p>Results from a quasi-optical gyrotron experiment with a 20-28 cm mirror separation will be presented showing operation at powers up to 150 kW and efficiencies up to 12%. The output coupling could be varied from 0.4-3% by changing the mirror separation and operating frequency. Operation was obtained over frequencies ranging from 95-130 GHz by changing the axial magnetic field, limited on the low end by waveguide cutoff in the diagnostics and at the high end by the maximum magnetic field achievable. The output power varied by approximately a factor of 2 over this range. Frequency variation of 4% was achieved by varying only the electron gun voltage; however, the output power also varied substantially due to the fact that the electron beam power was changing dramatically. Efficiency optimization by variation of output coupling and by</p> <p style="text-align: right;">(Continues)</p>					
20. DISTRIBUTION / AVAILABILITY OF ABSTRACT <input checked="" type="checkbox"/> UNCLASSIFIED/UNLIMITED <input type="checkbox"/> SAME AS RPT <input type="checkbox"/> DTIC USERS			21. ABSTRACT SECURITY CLASSIFICATION UNCLASSIFIED		
22a. NAME OF RESPONSIBLE INDIVIDUAL Arne E. Fliflet			22b. TELEPHONE (Include Area Code) (202) 767-2469		22c. OFFICE SYMBOL Code 4742

12. PERSONAL AUTHOR(S)

Fliflet, A.W., Hargreaves,* T.A., Manheimer, W.M., Fischer, R.P., Barsanti,** M.L., Levush,+ B. and Antonsen,++ T.

16. SUPPLEMENTARY NOTATION

*Mission Research Corporation, Newington, VA

**JAYCOR, Inc., Vienna, VA

+University of Maryland, College Park, MD

++Science Applications International Corporation, McLean, VA
also
University of Maryland, College Park, MD

19. ABSTRACTS (Continued)

tapering the magnetic field has been demonstrated. Regions of single-mode operation at powers up to 125 kW have been characterized and compared to recently developed theory. Details of the experimental design and its numerical modeling, along with the data obtained and its comparison to relevant theories are presented.

CONTENTS

I.	INTRODUCTION	1
II.	DESCRIPTION OF EXPERIMENT	4
III.	THRESHOLD CURRENT STUDIES	14
IV.	MULTIMODE POWER AND EFFICIENCY MEASUREMENTS	17
V.	FREQUENCY TUNING MEASUREMENTS	20
VI.	STUDIES OF NEAR-SINGLE-MODE OPERATION	20
VII.	DISCUSSION AND CONCLUSIONS	23
VIII.	ACKNOWLEDGEMENTS	27
	APPENDIX A — Calorimeter Calculations	29
	REFERENCES	31
	DISTRIBUTION LIST	77



Accession For	
NTIS GRA&I	<input checked="" type="checkbox"/>
DTIC TAB	<input type="checkbox"/>
Unannounced	<input type="checkbox"/>
Justification	
By _____	
Distribution/	
Availability Codes	
Dist	Avail and/or Special
A-1	

DESIGN AND OPERATING CHARACTERISTICS OF A CW RELEVANT QUASI-OPTICAL GYROTRON WITH VARIABLE MIRROR SEPARATION

I Introduction

There is currently a need for megawatt average power sources of 100–300 GHz radiation for electron cyclotron heating of fusion plasmas. The leading candidate for such a source, the waveguide cavity gyrotron [1], has produced output powers of 765 kW and efficiencies of 30% at 148 GHz in a CW-relevant configuration [2]. However, this gyrotron configuration is limited at high frequencies by high ohmic heating and problems with transverse mode competition, due to the highly overmoded configuration, and with beam collection, since the beam must be collected along a section of the output waveguide. The quasi-optical gyrotron (QOG), first proposed in 1980 by Sprangle, Vomvoridis and Manheimer [3], features an open resonator formed by a pair of spherical mirrors instead of a waveguide cavity and has the potential for overcoming each of these limitations. The resonator mirrors can be well removed from the beam-wave interaction region, allowing a large volume for the interaction and low ohmic heating densities at the mirrors. The beam direction is transverse to the cavity so that beam collection is separate from the output waveguide. This geometry is particularly well suited to the use of a depressed collector for electron beam energy recovery. The QOG operates in the lowest-order transverse (TEM_{001}) Gaussian mode of the resonator, higher-order transverse modes being effectively suppressed by higher diffraction losses. Output coupling is via diffraction around the mirrors and can be controlled independently of other interaction parameters. The axial mode separation is small compared to the interaction bandwidth in CW-relevant configurations so that multimode effects are important.

The theory of multimode operation was developed by Bondeson, Manheimer and Ott [4]. The theory of quasi-optical gyro-klystrons and of operation at the harmonics of the electron cyclotron frequency has also been examined [5,6]. The first QOG experiment was carried out in 1984 by Hargreaves *et al.* [7] and used a resonator with a 4 cm mirror separation. Consistent with the relatively low axial mode density of this resonator, single-mode operation was observed at powers up to 80 kW at a frequency of 110 GHz and an efficiency of 11%. The first experiment with large mirror separation (81 cm) was conducted in 1986 by

Read *et al.* [8] and achieved an output power of 50 kW at a frequency of 115 GHz and an efficiency of 7%.

The QOG is currently under investigation by several different groups. Alternate resonator configurations have been proposed and analyzed by Zhonghai, Shenggang and Kongyi of the People's Republic of China [9,10] and an experimental study of different output structures has been performed by Morse and Pyle [11]. Itoh *et al.* have utilized yet another resonator design to produce 20 kW of RF power at an efficiency of 16% and a frequency of 120 GHz [12]. This experiment utilized a relatively low power electron beam ($V = 30$ kV, $I = 3.5$ A). Experiments similar to those described here are being performed by Tran *et al.* [13]. With limited experimental time, powers and efficiencies as high as 85 kW and 10% have been observed from a cavity with a mirror separation of 34 cm.

A resonator mirror separation of 81 cm is much larger than necessary for a CW device and therefore has many more cavity modes than necessary within the interaction bandwidth of the device. The limiting factor on reducing the mirror separation is the ohmic heating of the mirrors. To be relevant to a CW device, the ohmic losses must be kept below a few kW/cm². To investigate the operation of a QOG with a minimum mode density consistent with a CW device, experiments have been performed utilizing a resonant cavity with a mirror separation of 20–28 cm.

A consequence of the use of a spherical mirror cavity with diffraction output coupling is that the output coupling can be a sensitive function of the mirror separation while the gyrotron interaction length, which depends on the radiation beam waist, remains approximately constant. This feature has been exploited for the first time in this experiment by using mirror holders which are adjustable over a wide range. The ability to vary the separation of the resonator mirrors from 20 to 28 cm allowed the resonator output coupling to be optimized with respect to the electron beam power. It also allowed new tests of the gyrotron scaling theory. The coupling of the annular electron beam to the standing-wave radiation in the cavity could be varied by translating the cavity transversely to the electron beam. Finally, precise mirror alignment—needed for optimum cavity Q —was easily maintained.

Several other aspects of this experiment have been upgraded from past experiments as well. The vacuum window that the output radiation passes through which is used here is made of thin ($\sim \lambda/10$) mylar. Thus, the window is essentially completely transparent over the complete frequency range of the experiment, making the measurement of the relative amplitudes of the different modes possible. Also, the possibility of the RF being reflected from the window back into the resonant cavity and affecting the electron beam-RF interaction is minimized. The new superconducting magnet used in this experiment was much more reliable than the magnet used in the past and also produced a much more uniform axial magnetic field. Essentially the electrons now have a much lower magnetic field bump to pass over as they travel into and out of the resonant cavity.

This paper presents results from a thorough and extensive experimental study of the first QOG to operate at powers over 100 kW using a CW-relevant resonator. The QOG was tunable from 95–130 GHz and operated at powers up to 148 kW and output efficiencies up to 12%. The peak electronic efficiency is estimated to be $16 \pm 2\%$. The main effect responsible for the difference between the output and electronic efficiency is ohmic heating of the mirrors which can be a significant fraction of the total output at low output coupling. This effect becomes small at MW output power levels due to larger output coupling. Single-mode operation was observed at powers up to 125 kW. Conditions for single-mode operation in the highly overmoded system have been characterized and compared with theoretical predictions. Efficiency optimization by variation of output coupling and by tapering the magnetic field have been demonstrated. These results point the way to the realization of megawatt level devices with output efficiencies of $\sim 20\%$.

A detailed description of the experimental configuration and diagnostic systems is given in Section II. Section III describes an investigation of threshold current behavior. Section IV describes power and efficiency, and the frequency tuning measurements are discussed in Section V. Section VI describes an investigation of single-mode or nearly single-mode operation and the comparison of this data with new theoretical results. Section VII presents additional discussion and conclusions drawn from the experiment. The technique used for calibrating the calorimeter used in the power measurements is analyzed in the Appendix.

II Description of Experiment

II-A Experimental Setup

A schematic diagram of the experiment is shown in Figure 1. The gyrating electron beam is generated by the MIG-type electron gun at the bottom of the superconducting magnet and propagates up through the drift tube and cavity before being absorbed in the collector. The microwave fields interact with the electron beam between the collector and drift tube where electrostatic space charge depression can affect the beam electrons' energy. The microwave power diffracted around each mirror is collected as output and propagated through the thin mylar window out of the vacuum. Design details of each of the experimental components are given in the following sections.

II-B Microwave Cavity

The microwave cavity utilized in these experiments consisted of the Fabry-Perot type open resonator shown in Figure 2. The spherical cavity mirrors formed an azimuthally symmetric cavity about the cavity axis. The mode structure and stability of this type of resonator is discussed by Yariv [14] who finds that the x -component of the electric field of the transverse electric and magnetic (TEM _{m,n}) modes in the cavity is given by:

$$E_x^{m,n}(x,y,z) = E_0 \frac{w_0}{w(z)} H_m \left(\frac{\sqrt{2}x}{w(z)} \right) H_n \left(\frac{\sqrt{2}y}{w(z)} \right) \exp \left\{ -\frac{(x^2 + y^2)}{w^2(z)} \right\} \sin \{kz + \varphi(x,y,z)\} \cos \omega t \quad (1)$$

where H_m is a Hermite polynomial of order m , w_0 is the radiation beam waist,

$$\varphi = \frac{k(x^2 + y^2)}{2R_w(z)} - (m + n + 1) \tan^{-1}(z/z_0) \quad (2)$$

is the wave phase shift,

$$w^2(z) = w_0^2 \left(1 + z^2/z_0^2 \right), \quad (3)$$

$$R_w(z) = z \left(1 + z_0^2/z^2 \right), \quad (4)$$

$z_0 = \pi w_0^2/\lambda$ is the Rayleigh length, k is the wave number, λ is the wavelength and ω is the angular frequency of the radiation, and R_w is the radius of curvature of the spherical

wavefront. As can be seen from Eq.(1), the electric field of the TEM₀₀ mode decreases more rapidly as a function of radius than that of the higher order modes. Therefore it may be expected that an appropriate choice of mirror diameter may yield a cavity where modes other than the TEM₀₀ are relatively unimportant due to their larger diffraction losses. For an electron beam located near the center of the cavity ($z \ll z_0$), and with dimensions small compared to the radiation beam waist, then $\varphi \simeq 0$ and

$$E_x^{m,n}(x, y, z) = E_0 \exp \left\{ -\frac{y^2}{w_0^2} \right\} \sin kz \cos \omega t. \quad (5)$$

The experimental cavity utilized 5 cm diameter mirrors with a 38.7 cm radius of curvature and were separated by 20–28 cm. These values place the cavity well into the stable region of parameter space as can be seen in Figure 3. A numerical code was used to calculate the electric field profiles at the surface of each mirror and thus the diffractive Q factor of the cavity. The details of the scalar theory on which these calculations are based are discussed in Ref. [15]. The calculated diffraction losses are lowest for the TEM₀₀ mode, giving that mode the highest Q value as expected. The diffractive output coupling for the TEM₀₀ mode calculated by the code is plotted as a function of mirror separation for frequencies of 110, 120, and 130 GHz in Figure 4. The corresponding calculated total Q factors including ohmic losses for gold-coated mirrors (assumed conductivity: $\sigma = 4.5 \times 10^7$ siemens/m) are plotted in Figure 5. Other calculated parameters for the cavity are shown in Table I for various mirror separations.

The total ohmic losses in the cavity for a given electric field amplitude in the electron beam interaction region are independent of mirror separation for constant output coupling and are essentially independent of output coupling for constant mirror separation. Therefore, the fractional power lost to ohmic heating increases as the output coupling decreases. The ratio of power lost through ohmic heating of the mirrors (P_o) to the diffraction output power (P_d) is given by

$$\frac{P_o}{P_d} = \sqrt{\frac{32\omega}{Z_0 c \sigma T}}, \quad (6)$$

where c is the speed of light, T is the total round trip cavity diffraction loss, and $Z_0 = 377$ is the free space impedance. The ratio of ohmic heating to radiated output power is plotted

as a function of mirror separation for frequencies of 110, 120, and 130 GHz in Figure 6. This figure shows that at 120 GHz and 20 cm mirror separation, the ohmic heating is over 40% of the radiated power. As shown in Eq. (6), this ratio would decrease to a much smaller value in a higher power device with several times larger output coupling. The peak heating density at the center of the mirrors can be expressed in the form

$$\rho \text{ (kW/cm}^2\text{)} = 4.1 \times 10^{-22} \sigma^{-0.5} \omega^{2.5} \gamma^2 \beta_{\perp}^6 (1 + g) F^2, \quad (7)$$

where γ is the electron beam relativistic factor, β_{\perp} is the transverse velocity normalized to the speed of light, $g = 1 - d/R$, where d is the mirror separation and R is the mirror radius of curvature, and F is the peak normalized wave amplitude at the beam defined by

$$F = \frac{E_0}{B_0 c \beta_{\perp}^3}, \quad (8)$$

where B_0 is the applied axial magnetic field. The heating density can be controlled by allowing the parameter g to approach -1 , that is, by moving the mirrors further apart. Using the radius of the phase front, given by Eq. (4), it is readily verified that at $z = d/2$, $g > -1$, but approaches the unstable limit $g = -1$ as $d \rightarrow \infty$. As shown in Figure 3 the limit $g = -1$ corresponds to the concentric resonator which is on the boundary between stable and unstable configurations. In the present configuration $0.3 < g < 0.5$, which is well within the stable region. To a good approximation, the average heating density on the mirrors for a Gaussian resonator mode is obtained by dividing the peak heating density by $\ln T_m^{-1}$, where T_m is the output coupling per mirror.

A final value calculated by the mirror cavity code is the amount of the diffracted power that is actually collected as output compared to that diffracted around the outside of the output collecting waveguide. In general, this fraction is highest for high output coupling and when the output is collected off of both mirrors. A second reason for collecting output from both mirrors is that it makes possible a completely symmetric system and simplifies the analysis.

II-C Cavity Mirror Holders

It is well known with cavity gyrotrons that the cavity alignment with the electron beam is critical for optimum performance of the gyrotron. In the QOG, the cavity fields at the electron beam form essentially a standing plane wave. The position of the the annular electron beam (diameter: 3.2 mm) is not as critical, although there is a loss in coupling efficiency with single-mode theory predicting a reduction of approximately 30% in the output efficiency of the device relative to the case of a pencil beam. An overlay of the electron beam with the cavity electric field for the case of the beam axis on the field maximum is shown in Figure 7. On the other hand, alignment of the two cavity mirrors with each other is critically important. For this reason, the cavity mirror holders were designed so that each mirror could be individually aligned with the other mirror. The mirror holders are shown in Figure 8. Each mirror can move 4 cm axially, allowing the cavity to be translated as a unit relative to the electron beam as well as allowing for as much as an 8 cm variation in mirror separation.

II-D Microwave Transmission System

The output waveguide system is an integral part of the mirror holder design shown in Figure 8. The fact that each mirror must be able to move relative to its mounting flange forces the output waveguide to be discontinuous, a less than desirable trait. The result of this discontinuity may be some reflection of the output microwave power back toward the resonant cavity, although the reflected power is expected to be relatively small due to the large diameter of the waveguide compared to the operating wavelength.

The output waveguide has a diameter of 10 cm at the surface of the cavity mirror, maximized to collect as much of the output radiation as possible, and limited only by the size of the magnet cross-bore. A cone is attached to the back of the mirror, so that the output system which begins as coaxial waveguide slowly tapers down to cylindrical waveguide. The cylindrical waveguide then undergoes a series of gradual tapers and two discontinuities as shown in the figure, with the final discontinuity occurring at the vacuum window. The tapers and discontinuities in the output waveguide are not expected to cause

large reflections since the waveguide diameter is always large compared to the radiation wavelength ($d \approx 20\lambda$). The vacuum window used in these experiments was 0.013 cm thick mylar. Its dielectric constant is estimated to be approximately 3.2, making the window thickness $< 0.1\lambda$ at 120 GHz. Therefore the window possessed the admirable quality of being essentially transparent to any of the radiation produced in the experiment.

The two waveguide outputs were typically terminated in different diagnostics. The microwaves from one were allowed to radiate from the open end of the waveguide toward a modified laser calorimeter placed approximately 5 cm away. The microwaves from the other output waveguide were allowed to radiate into a box lined with microwave absorber. The open end of a piece of fundamental waveguide was inserted through the end of the box into the radiation pattern and used as a pickup to measure the characteristics of the microwave radiation.

II-E Electron Gun

The electron gun used in this experiment was a Varian VUW-8010 magnetron injection gun originally designed for use at 35 GHz [16]. Two trim coils in the gun region augmented the superconducting magnet coils. These coils were operated with opposing currents and were used to vary the magnetic compression of the beam and to avoid beam interception in the gun region. The fact that the QOG is relatively insensitive to the size of the electron beam and its axial velocity spread eased the requirements on the gun, making the VUW-8010 gun usable.

The electron gun was modeled using the Hermannsfeldt electron trajectory code [17]. Modeling the electron trajectories from the gun into the cavity is a fairly time consuming computational task due to the relatively large dimensions of the gun and beam drift tube compared to the electron gyroradius. For this reason the electrons were followed into the microwave cavity in only a few cases. Instead, the parameter space was experimentally explored, essentially by optimization of the trim coil currents, with the electron trajectory code being used to model specific experimental settings. The geometry modeled is shown in Figure 9, and the results of the calculation are plotted in Figure 10. This run was stopped

slightly after the position of maximum magnetic field. If the electron trajectories are then adiabatically scaled down to the cavity field, the average α value is reduced from 1.4 to 1.3. The 37% spread in α calculated means that some of the electrons in the beam are close to being reflected by the compressing magnetic field. This yields a beam with the largest α and is consistent with the experiment, which tended to produce the best results when the electron gun was operated on the edge of stability.

II-F Electron Beam Path

The electron beam is produced by the electron gun in a relatively low ($B = 0.29$ T) magnetic field. As the electrons travel toward the cavity, they are compressed by the strengthening magnetic field which peaks at 5.4 T (for a 5.0 T magnetic field in the microwave cavity). As the electron beam is compressed, the electron energy is essentially transferred from motion parallel to the magnetic field into motion perpendicular to the magnetic field. It is the perpendicular motion that mainly interacts with the microwave fields in the cavity to produce radiation.

As the electrons emerge from the electron gun, they enter the drift tube shown in Figure 11, the first section of which is a tapered piece of graphite. Since the magnetic field and hence the electron beam velocity pitch ratio α is low, the chance of exciting gyrotron modes in this section is minimal. This danger increases as the electron beam travels toward the cavity and is compressed by the magnetic field. For this reason, dielectric rings (with a large loss tangent) are used to heavily load any possible microwave cavity in the remainder of the drift tube. The dielectric rings are alternated with copper "scraper" rings designed both to prevent the electrons from hitting the dielectric and also to ensure that excessive charge is prevented from building up on the surface of the dielectric, reducing the potential and affecting the beam propagation. The second (inner) dielectric ring shown in this figure has an intermediate dielectric constant to minimize reflections of the microwaves from the surface of the lossy medium. The peak magnetic field experienced by the electrons (where the electrons have their largest perpendicular momentum and, hence, free energy) is actually inside the drift tube.

In the QOG the electron beam experiences space-charge effects in the drift tube between the gun and the cavity and in the open region between the end of the beam drift tube and the collector. An estimate for the space-charge depression of the beam voltage in the drift tube is [18,19]

$$\Delta V_{sc} = \frac{60I}{\beta_{||}} \ln(R_d/r_b) \quad (9)$$

where I is the beam current, $\beta_{||}$ is the axial velocity normalized to the speed of light, r_b is the beam radius, and R_d is the drift tube radius which is 0.5 cm in the present experiment. For typical parameters of 75 kV and $\alpha = 1$, this leads to a voltage depression in the drift tube of $\Delta V = 2$ kV at 10 A. An accurate calculation of space-charge depression in this region involves two-dimensional effects, but a simple estimate for the space-charge depression of the beam voltage in this region can be obtained by replacing drift tube wall radius in Eq. (9) by half the drift tube-collector separation L . Although this choice is somewhat arbitrary and should be considered a temporary replacement for more accurate calculations, the result depends only logarithmically on the ratio of beam radius to half the length of the open space. A length of 5 cm was used in the present experiment. Cold tests showed that at this separation the presence of the beam guiding structures had no measurable effect on the cavity Q . The voltage depression of the beam due to space charge is plotted up to the space-charge-limited current for several beam voltages in Figure 12. This figure suggests that the highest currents at which the experiment was operated (which corresponded to the highest output powers) were near the space-charge limit. This prescription leads to an estimated space-charge depression of the beam in the optical resonator of $\Delta V = 4.8$ kV at 10 A which is more than twice the space-charge depression occurring in the drift-tube.

As soon as the electrons have exited the cavity fields, they enter the collector. The second peak of the magnetic field is inside the collector, which also serves to diminish space charge effects. Once past the magnetic field peak, the electrons essentially follow the magnetic field lines as they expand. Eventually, the magnetic field lines intersect the collector wall and the electrons are absorbed by the collector.

II-G Diagnostics

A schematic diagram of the experimental diagnostics is shown in Figure 13. Standard millimeter-wave wafer diodes were used to measure the RF pulse shape. The diodes were terminated in 50 ohms to keep the response time of the diodes short compared to the radiation pulse width. Diodes from both Baytron and Hughes were used during these experiments with no inconsistencies observed.

The harmonic heterodyne system shown in Figure 14 was used to measure the frequency of the output radiation. The gyrotron radiation was inserted into the RF port of a harmonic mixer, and the power-leveled output of a frequency-locked 12-18 GHz YIG-tuned oscillator was applied to the LO port. The radiation out of the IF port was then measured through one of several bandpass filters used to vary the resolution of the device. The three frequencies are related by

$$f_{RF} = n f_{LO} \pm f_{IF}, \quad (10)$$

where n is the number of the harmonic of the local oscillator (frequency f_{LO}) that is mixed with the RF frequency from the experiment. The different bandpass filters each have a center frequency of 160 MHz so that for a given RF frequency, IF signals (frequency f_{IF}) will be measured for two different LO frequencies. The harmonic number may be determined from the frequency difference between the two LO frequencies,

$$n = 320 \text{ MHz} / \Delta f_{LO}. \quad (11)$$

Once the harmonic number has been determined, it is straightforward to calculate the experimental operating frequency from Eq. (10) above. The accuracy of this instrument depends mainly on the accuracy of the LO frequency measurement and the bandpass filter accuracy. Relative measurements depend only on the bandpass filter chosen so that accuracies of approximately ± 10 MHz were possible. This was more than sufficient to differentiate between longitudinal cavity modes which have a frequency spacing of $\Delta\nu = c/(2d)$ or approximately 500 MHz at the maximum separation of 28 cm. A second method of measuring the frequency was to use the Fabry-Perot interferometer shown in Figure 15. The core of this device is a mirror cavity similar to the resonant cavity used in the experiment. The

electric fields in the interferometer are again given by Eq. (1), with modes other than the TEM₀₀ modes being effectively suppressed by the application of absorbing material around one of the mirrors to decrease its effective diameter. The phase of the RF field at position z in the cavity is given by

$$\phi = \frac{2\pi z}{\lambda} - \tan^{-1} \left(\frac{z}{z_0} \right) \quad (12)$$

where $z_0 = 40$ cm is the Rayleigh length for this cavity. As the mirror separation is increased, successive resonances occur as ϕ is increased by π . To a good approximation, this occurs as the separation is increased integral numbers of half (free space) wavelengths. Thus by carefully measuring the distance that the mirror separation changes between successive resonances, the radiation wavelength can be measured to approximately 0.1%.

The main power diagnostic was the laser calorimeter shown in Figure 16. The absorbing surface was coated with several extra layers of paint, with its absorbancy being measured between each coat at 120 GHz. The absorbancy is plotted in Figure 17 as a function of paint thickness. Figure 18 shows the measured absorption of the calorimeter as a function of microwave frequency after the additional paint had been added. The problem of a plane electromagnetic wave incident on a dielectric layer backed by a conductor can be solved analytically. The geometry relevant to the quasi-optical gyrotron (electric field parallel to the boundary surface) is shown in Figure 19. The details of the calculation are given in Appendix A, where it is shown that the power reflection-coefficient is $R = |(1-D)/(1+D)|^2$. The quantity D is given by

$$D = \frac{\cos \theta_t}{\cos \theta_i} \sqrt{\frac{\epsilon_2}{\epsilon_0}} \left[\frac{1 + e^{-2ik_2\tau \cos \theta_i}}{1 - e^{-2ik_2\tau \cos \theta_i}} \right], \quad (13)$$

where θ_i is the angle of incidence; θ_t is the angle of transmittance; $\epsilon_2 = \epsilon_{r2}\epsilon_0(1 - i \tan \delta)$ is the dielectric constant of the paint; ϵ_{r2} , $\tan \delta$ and k_2 are the associated real part of the dielectric constant relative to vacuum, loss tangent and complex wave number, respectively; and τ is the thickness of the paint. Plots of the experimental data and the analytic calculations are shown in Figures 17 and 18. For these calculations the real part of the dielectric constant (ϵ_{r2}) was 5 and the loss tangent was 0.25. These values result in reasonably good agreement once one realizes that the actual thickness of each layer of paint is unknown and probably

varied. For the data plotted, however, each paint layer is assumed to be of equal thickness.

The voltages applied to both the cathode and the intermediate anode were measured by capacitive dividers. Sample traces of each waveform are shown in Figure 20. The peak-to-peak voltage ripple is approximately 4% over the 12 μ sec flat top of the cathode voltage pulse. The 10-90% rise time of the cathode pulse was 3.5 μ sec, and the 90-10% fall time was 4 μ sec. The intermediate anode voltage waveform was adjustable in steps of 1% of the cathode voltage. The shape (flatness and rise time) of the intermediate anode voltage trace could be controlled within limits by varying the capacitance in parallel with the voltage divider.

The collector and body currents were separately monitored by Pearson probes. These probes had a rise time of 10 nsec and a low frequency cutoff of 140 Hz, making them suitable for our purposes. The current trace is typically much longer than the flat-top of the voltage trace, due to the use of a thermionic electron gun with a voltage pulse that rises and falls somewhat slowly.

II-H Magnetic Fields

The magnetic field is produced by a pair of superconducting coils and modified in the region of the electron gun by a pair of normal trim coils. The separation of the two superconducting coils is set by the cross-bore diameter necessary for the microwave cavity and radiation output structure. The presence of the cross-bore results in a magnetic field axial profile that is less than ideal. To achieve the necessary magnetic field strength in the cavity together with an appropriate cross-bore diameter, the superconducting coils had to be separated slightly more than a Helmholtz pair. This extra separation resulted in the cavity magnetic field being approximately 6.5% lower than the peak magnetic field along the magnet axis. A plot of the axial magnetic field is shown in Figure 21.

The effect of the pair of trim coils is localized near the position of the electron gun. The coil furthest from the superconductors acts to lower the magnetic field near the cathode thus increasing the magnetic field compression ratio and the beam α in the cavity. The second trim coil increases the axial field locally to compress the electron beam in order to

prevent it from being intercepted by the electron gun electrodes. The superconductor and trim coil positions relative to the cathode position are shown in Figure 22.

II-I High Voltage Modulator

The modulator used to supply the high voltage to the electron gun is a standard capacitive-discharge type followed by a pulse-forming network and a step-up transformer. The modulator is capable of producing 50 A at voltages up to 90 kV. Most of the current is dissipated in an oil-filled load box via a resistive shunt in parallel with the electron gun. This serves to maintain a constant load impedance for the modulator despite the fact that the electron gun impedance changes radically throughout the pulse. A straight resistive divider is used to supply the necessary voltage to the intermediate anode. A schematic diagram of the high-voltage source is shown in Figure 23.

III Threshold Current Studies

The threshold current for single-mode oscillation at the fundamental harmonic can be derived using single particle theory in the small signal approximation. The result in MKS units is [20]

$$I_{thr} = \frac{2\pi^4 m_e c \gamma \beta_{\perp}^4}{\mu_0 e} \frac{d}{Q} \left(\frac{w_0}{\lambda} \right)^2 \frac{2}{1 \pm J_0(2kr_b)} \hat{I}(\Delta, \mu), \quad (14)$$

where m_e and e are the mass and charge (magnitude) of an electron, μ_0 is the free space permittivity, Q is the resonator quality factor, and J_0 is a regular Bessel function. The beam waist for the TEM₀₀ Gaussian mode of the resonator is given by

$$w_0 = \sqrt{\frac{d\lambda}{2\pi}} \left(\frac{1+g}{1-g} \right)^{1/4}. \quad (15)$$

The normalized threshold current \hat{I} is given by [21]

$$\hat{I}(\Delta, \mu) = \frac{8}{\pi \mu^2} \frac{e^{\Phi^2/2}}{\mu \Phi - 2}, \quad (16)$$

where $\Phi = \mu\Delta/2$ is the kinematic phase-slip angle of the electrons transiting the resonator,

$$\mu = 2\pi\alpha\beta_{\perp}w_0/\lambda \quad (17)$$

is the normalized interaction length, and

$$\Delta = \frac{2}{\beta_1^2} \left(1 - \frac{eB_0}{\gamma m_e \omega} \right) \quad (18)$$

is the resonance detuning parameter. The factor $2/(1 \pm J_0(2kr_b))$ in Eq. (14) accounts for the annular beam geometry [22]. The $+$ ($-$) sign corresponds to placing the electron beam axis on a maximum (null) of the wave field as illustrated in Figure 7.

A comparison between the theoretical and measured threshold oscillation currents as a function of magnetic field is shown in Figures 24–26 for mirror separations of 25 and 20 cm. The beam accelerating voltage is 57 kV, $r_b = 1.6$ mm, and the operating frequency is near 110 GHz in both cases. The data in these figures was obtained by varying the magnetic field trim coils near the gun to minimize the threshold oscillation current. The theoretical curves are based on a momentum pitch ratio $\alpha = 1.5$ which is considered achievable in the present experiment at currents up to a few amperes based on previous operating experience with the electron gun and simulations of the gun. At higher currents the best estimate is $\alpha \sim 1$ with some drop-off expected for currents above 15 A. Near the minimum threshold current only a single-mode was observed to be present. Multimode operation was observed when the current exceeded 2–3 times the minimum threshold current. Thus the single-mode theory is valid only near the minimum oscillation current.

Results for a mirror separation of 25 cm are shown in Figure 24. For frequencies near 110 GHz the calculated resonator Q factor including ohmic losses and the diffraction output coupling is $Q = 38,000$. The transmission coefficient $T = 2.8\%$ for this separation and the separation between adjacent longitudinal modes is 600 MHz. The measured frequency of the data denoted by the solid dots is 109.8 ± 0.1 GHz. This data was obtained by translating the mirrors while holding the separation constant to minimize the threshold current and thus place the beam on the microwave electric field maximum for this mode as shown in Figure 7. This had the effect of raising the threshold current of adjacent modes as expected and, at currents below 1.5 A, the adjacent modes could not be excited. The data shown by the open circles corresponds to the next lower frequency mode—which should also have its E-field maximum at the beam axis. The measured frequency of this mode is 108.7 ± 0.1 GHz.

A frequency of 109.8 GHz was used in obtaining the theoretical result denoted by the solid curve which is closest to the solid dot data. The other solid curves correspond to other longitudinal modes of the resonator with frequencies shifted by multiples of 1200 MHz. Consistent with the data, the solid curves correspond to modes for which the beam axis falls on a field maximum. Theoretical results for the intermediate modes, for which the beam axis falls on a field null, are shown by the dashed curves. Given the experimental uncertainties, the agreement between theory and experiment near the minimum threshold current is remarkably good. Probably the least well-known parameter is the beam α . The sensitivity of the theoretical results to varying α is shown in Figure 25 which shows the 109.8 GHz data from Figure 24 compared with the corresponding theoretical results for $\alpha = 1, 1.5$, and 2. The best fit is clearly obtained for $\alpha = 1.5$.

Figure 26 shows data obtained for a mirror separation of 20 cm. The resonator Q factor and output coupling are calculated to be 82,000 and 0.9% for frequencies near 110 GHz. The measured oscillation frequencies are 109.8 ± 0.1 GHz (solid dot data) and 109.2 ± 0.2 GHz (open circle data). The expected frequency separation for this mirror separation is 750 MHz. This data was obtained without minimizing either mode threshold current with respect to electron beam position. The fact that these adjacent modes have essentially equal minimum threshold currents indicates that the electron beam axis does not coincide with an E-field maximum for either mode. To account for this; the theoretical threshold currents plotted in Figure 26 represent an average of the threshold current obtained for the beam axis at a field maximum and the threshold current obtained for the beam axis at a field null. The theoretical curve closest to the solid dot data corresponds to a frequency of 109.8 GHz, and the other curves represent the other nearby longitudinal modes for this mirror separation.

The threshold current dependence on the beam axis position is shown explicitly in Figure 27. The data was obtained by translating the mirrors perpendicularly to the beam, holding the separation fixed at 20 cm. This is equivalent to translating the beam relative to the standing-wave pattern in the resonator. The resonator magnetic field ($B = 43$ kG), the electron beam voltage ($V = 52.4$ kV), and the cathode magnetic field were held constant during these measurements. Operation was single-moded at a frequency of 111 ± 0.1 GHz.

The solid sinusoidal curve shown in Figure 27 is proportional to the standing-wave E-field pattern in the resonator. The first maximum of this curve has been adjusted to coincide with the beam position which gives the minimum threshold current. The positions of measured threshold current maxima are then found to fall on nulls of the wave field. The ratio of minimum to maximum measured threshold current is 0.6. This is in good agreement with the theoretical ratio of 0.57 for an annular beam with $r_b = 1.6$ mm and provides further evidence that the electron beam is interacting with the TEM_{00l} modes of the resonator.

IV Multimode Power and Efficiency Measurements

Output power measurements were carried out as a function of beam current and mirror separation. A preliminary investigation of output power and efficiency showed that for currents of less than 8 A, output power was a decreasing function of mirror separation. Power measurements for a gun voltage of 66.7 kV and a current of 8 A at three mirror separations are shown by the solid square data points in Figure 28. Consequently, initial power and efficiency measurements were taken at the minimum mirror separation of 20 cm. This minimizes the output coupling and so leads to the optimum saturated efficiency at the lowest current, where beam quality should be highest. Mirror alignment and translation were optimized by minimizing the threshold current for a magnetic field of 50 kG and a beam voltage of 66.7 kV. A minimum threshold current of 0.25 A at a frequency of 125.8 GHz was obtained. For these conditions the calculated total resonator Q factor is 160,000 and the theoretical minimum threshold current for $\alpha = 1.5$ is 0.12 A, or about half the measured value. This discrepancy suggests that the experimental total Q factor may be $\sim 80,000$, i.e, only half the predicted value, however, the calculated minimum threshold current depends on α which is not well characterized in the experiment. Using the total Q inferred from the threshold measurement and the theoretical ohmic Q leads to an estimate of the diffraction Q of 96,000. The calculated diffraction Q is 250,000.

The output power was obtained by multiplying the calorimeter power measurement by two, dividing by the repetition rate and the pulse width, and correcting for the absorption efficiency of the calorimeter. The radiation pulsewidth was found to be equal to a good

approximation to the beam voltage flat-top pulse width of 13 μsec under most conditions and this pulse width was used in the peak power calculation. The power output through the two windows was checked and found to be equal within measurement accuracy. As shown in Figure 18, the calorimeter absorptivity was measured to be 94% at 120 GHz and to decrease with decreasing frequency to $\sim 60\%$ at 90 GHz.

The output power as a function of beam current is shown in Figure 29 for magnetic fields of 44, 47, and 50 kG and a constant gun voltage of 71.5 kV. Based on the calorimeter reflectivity measurements, a calorimeter efficiency of 95% was used in the output power computations for the magnetic fields of 47 and 50 kG; an efficiency of 88% was used for the 44 kG results. The corresponding output efficiency is shown in Figure 30. The observed maximum output efficiencies for these magnetic fields and conditions was 12% at 50 kG, 11.9% at 47 kG, and 11% at 44 kG. In obtaining this data no attempt was made to promote single-mode operation and, consequently, operation was generally multimoded. Typical multimode frequency spectra are shown in Figures 31(a)–(c). The spectra correspond to magnetic fields of 44, 47, and 50 kG, respectively, and a gun voltage of 71.5 kV. The beam current in Figures 31(a) and (c) is 8 A and is 14 A in Figure 31(b).

To obtain the electronic efficiency for a given output efficiency, it is necessary to correct for ohmic heating losses according to

$$\eta_{el} = (1 + Q_d/Q_o)\eta_{out}, \quad (19)$$

where η_{el} and η_{out} are the electronic and output efficiencies, and Q_d and Q_o are the diffraction and ohmic quality factors.

As discussed above the ratio Q_d/Q_o depends sensitively on the diffraction Q factor, which has not been directly measured. For operation at 50 kG, $Q_d/Q_o = 0.2$ based on Q_d inferred from the threshold current measurement, whereas $Q_d/Q_o = 0.55$ based on Q_d calculated using scalar diffraction theory. The corresponding electronic efficiencies are plotted as functions of IQ/d in Figure 32. Using the value of Q_d inferred from the threshold current measurement leads to a maximum electronic efficiency of 14%; using the value of Q_d calculated with scalar diffraction theory leads to a maximum electronic efficiency of 18%. The

figure also shows theoretical results based on a nonlinear, multimode simulation [4] using parameters corresponding to the 50 kG data and assuming $\alpha = 1$. These calculations yield a maximum efficiency of 17.7%. The theoretical optimum value of $QI/d \sim 2.0 \times 10^6$ which is in good agreement with the experimental results based on the Q factor inferred from the threshold current measurement but not with the results obtained using the theoretical Q factor.

The electronic efficiency was not corrected for the space-charge depression of the beam voltage, because the free energy for the interaction is associated mainly with the transverse momentum of the electrons which is not greatly affected by the presence of space charge. Space charge does limit the maximum beam power which can be propagated in the resonator and reduces the achievable velocity pitch ratio.

As shown in Figure 30, for a magnetic field of 50 kG and a mirror separation of 20 cm, the output efficiency decreases as the current is increased beyond 6 A. This effect of over-driving the resonator is well known from cavity gyrotrons. Increased power and efficiency at currents above 6 A can be obtained in the QOG by increasing the output coupling by increasing the mirror separation until the optimum RF field amplitude is re-established in the cavity. This effect is illustrated by the solid data in Figure 28 which shows output power optimization by variation of the mirror separation for a constant beam current of 13.5 A and a constant gun voltage of 71.5 kV.

The output power and efficiency as a function of beam current for a magnetic field of 50 kG, gun voltage in the range 71–75 kV, and beam currents up to 24 A are shown in Figure 33. Operation was generally multimoded with 4–6 modes being excited. The frequency of the strongest modes was ~ 125 GHz. The data indicated by the squares corresponds to the minimum mirror separation of 20 cm and a gun voltage of 71.5 kV. The calculated diffractive output coupling at this separation is 0.4% for 125 GHz radiation. The data indicated by the triangles and dots correspond to a mirror separation of 23 cm and a calculated 0.8% diffraction output coupling. The highest measured power, shown by the solid dots, was 148 kW and was obtained at a mirror separation of 23 cm, a beam voltage and current of 78 kV and 24 A, and a negative taper in the magnetic field of 2%

across the interaction region. This current is estimated to be near the space-charge limit for this voltage and $\alpha = 1$. No evidence of oscillation in higher order transverse modes was observed from the frequency measurements at 50 kG or other magnetic fields.

V Frequency Tuning Measurements

In the QOG the operating frequency is approximately Ω_c/γ , where Ω_c is the nonrelativistic electron cyclotron frequency, so that the operating frequency can be tuned by varying either the magnetic field or the gun voltage. Figure 34 presents frequency and power measurements for magnetic fields from 38 to 50 kG with fixed gun voltage (66.7 kV) and current (~ 12 A). Operation was usually multimoded as indicated in the figure which shows frequency variation from 95 to 130 GHz. Significantly, the power varied by < 3 dB for this frequency variation. The QOG could have operated at still lower frequencies (at lower magnetic fields), but such frequencies were below the cutoff frequency of the waveguide used in the heterodyne frequency diagnostic.

Frequency variation with electron gun voltage was also investigated. Frequency measurements were obtained several voltages between 43 and 72 kV for a magnetic of 50 kG and a current of ~ 10 A. As shown in Figure 35, a 4% frequency increase was measured for this variation in gun voltage. A disadvantage of this method of frequency tuning is that power scales strongly with voltage and decreased from 70 to 25 kW as the voltage was decreased.

VI Studies of Near-Single-Mode Operation

Since the longitudinal mode density of the QOG resonator is high, it might be thought that the device is inherently multimoded, but this is not the case. The operating parameter space was characterized by regions of stable single-mode or near-single-mode operation. Single-mode operation was most common at lower powers but was also observed at powers up to 125 kW. At a current near threshold, a single-mode having the highest growth rate can be excited. It was found that if the current was then increased holding the magnetic

field and gun voltage fixed, the cavity would oscillate in a sequence of higher frequency modes as shown in Figure 36. The data plotted in this figure was obtained for a gun voltage of 71.5 kV, a mirror separation of 23 cm, and a magnetic field of 47 kG in the middle of the interaction region. The magnetic field had a negative 2% taper across the interaction region. Alternatively, it was possible to vary the voltage while increasing the current (keeping the magnetic field fixed) so as to maintain single-mode operation in the mode initially excited. Figure 37 shows a region of single-mode operation in $V - I$ space obtained using the latter procedure. An untapered magnetic field of 47 kG was used to obtain this data at an operating frequency of 119 GHz. The area of single-moded operation is denoted approximately by the line thickness; voltage changes of ~ 0.5 kV led to observable changes in the mode spectrum. The maximum power of the data in this figure is 55 kW. Figure 38 shows the output power obtained during single-mode or near-single-mode operation for mirror separations of 23, 25.5 and 28 cm. The magnetic field was 47 kG and the oscillation frequency was 119–120 GHz in all cases. Here, output powers as high as 125 kW were obtained while maintaining nearly single-mode operation. At least 90% of the output power was in a single-mode, with most of the remaining power in the two adjacent modes. Relative mode power was measured using the amplitude response of the heterodyne frequency diagnostic.

As the current was increased above threshold, it was found that single-moded operation corresponded to progressively higher resonance frequency mismatches $(\omega - \Omega_c/\gamma)$. Figure 39(a) shows frequency mismatch uncorrected for the space-charge effect versus the beam current normalized to the oscillation threshold current for the data shown in Figure 38. Figure 39(b) illustrates the frequency mismatch obtained by correcting the electron cyclotron frequency for space-charge depression of the beam as discussed in Section II-F.

To compare the theoretically predicted stable, single-mode operating regime [23] with the experimental data, it is convenient to express the data in terms of the normalized RF electric field amplitude, \hat{E} , and the kinematic phase parameter for the interaction, Φ , which

are given by

$$\Phi = \frac{2\pi}{\beta_{||}} \left(1 - \frac{\Omega}{\omega}\right) \frac{w_0}{\lambda} \quad (20)$$

$$\hat{E} = \frac{8\pi}{B_0\lambda} \frac{1 + \alpha^2}{(1 - \gamma^{-2})\alpha} \sqrt{\frac{Z_0 P}{\pi c^2 T}}, \quad (21)$$

where P is the diffraction output power. The parameter \hat{E} can be expressed in terms of the normalized interaction parameters F and μ according to $\hat{E} = F\mu$, and as discussed above, $\Phi = \mu\Delta/2$. An advantage of the new parameters is their relative insensitivity to α which is not well determined in the experiment. Theoretically, the stable operating regime for a fixed μ corresponds to an area in \hat{E} - Φ space. Uncertainty in the beam velocity pitch ratio α leads to a range of possible μ values from 5-10. The region of stable, single-mode operation predicted by theory corresponds to the area bounded by the solid curves in Figures 40(a) and (b) which were obtained assuming $\alpha = 0.65$ ($\mu = 5$) and $\alpha = 1$ ($\mu = 10$), respectively. These plots were made for an annular beam of radius 1.6 mm centered on the electric field maximum of the equilibrium mode. Equilibria with values of \hat{E} , Φ outside the stable region are unstable with respect to the growth of neighboring modes (sidebands). The use of an annular beam configuration has an important effect on the size and shape of the stability boundary [23]. In particular, the stable region for an annular beam is much smaller than that for a pencil beam. This reduction occurs because, unlike the pencil beam, an annular beam couples to both the odd and even symmetry modes of the resonator. If beam-RF coupling is optimized for the desired operating mode, coupling to the two adjacent modes, which have opposite symmetry, will be weaker. The weaker coupling of the principal competing modes inhibits saturation of their gain by the main mode, an important factor in determining the region of stable operation. Comparison of the Figures 40(a) and (b) shows that the predicted stable area is smaller for $\mu = 10$ than for $\mu = 5$. The reduction in stable region with increase in μ is a general feature of the theory for both pencil and annular beams. The experimental single-mode data for mirror separations of 23, 25.5 and 28 cm, assuming either $\alpha = 0.65$ or 1, is also shown in Figures 40(a) and (b). The data indicates single-mode operation occurs for $\hat{E} \leq 2$. This is consistent with the theoretical results for $\mu = 5$ but not $\mu = 10$. However, nonlinear, time

dependent, multimode simulations for $\mu = 10$ show that the unstable sidebands saturate at a sufficiently low level that the resulting equilibrium appears single-moded within the resolution of the experimental data (90% of power in main mode). Thus, the theoretical results regarding single-mode operation are not inconsistent with $\mu = 10$ ($\alpha = 1$) in the experiment. The experimental data is primarily limited to the lower halves of the stable regions, whereas theory predicts that all points should be accessible. Simulations modeling the finite rise time of the voltage pulse indicate that this is not a factor which limits the accessible region. The inability to tune the gyrotron within the stable region without loss of single-modedness is not understood, but may be related to the 4% ripple of the voltage pulse which corresponds to a variation in the detuning parameter Φ .

The measured electronic efficiency corrected for ohmic effects is compared in Figure 41(a) and (b) with the theoretical annular beam single-mode efficiency for $\mu = 5$ and 10 and using the measured detuning. The agreement is much better for $\mu = 5$ than 10. The calculated efficiency for $\mu = 10$ is about 60% greater than the measured efficiency. In addition, the calculated efficiency peaks at a value of \hat{E} lower than that suggested by the data. The calculated efficiency for $\mu = 5$ ($\alpha = 0.65$) is in better agreement with the data both in maximum value and dependence on \hat{E} .

VII Discussion and Conclusions

Extensive results have been obtained for a CW-relevant QOG which demonstrate for the first time many of the advantages of this configuration at output powers up to 148 kW. A peak output efficiency of 12% was obtained which is estimated to correspond to an electronic efficiency of 14-18%. The difference between output and electronic efficiency is due mainly to ohmic heating losses which can dominate at low output coupling but would not be a factor in a 1 MW device, which would typically have a much larger output coupling. Single-mode operation was observed at powers up to 125 kW, and the frequency was tunable from 95 to 130 GHz by varying the magnetic field. Frequency tuning of 4% was obtained by gun voltage variation. Efficiency optimization by variation of the output coupling and by tapering the magnetic field has been demonstrated. The region of single-

mode operation of a highly overmoded quasi-optical cavity has been characterized for the first time.

The use of resonator mirror holders allowing flexible and precise adjustment of mirror separation, translation, and alignment has enabled the investigation of many interesting features of the quasi-optical gyrotron, especially the ability to vary the output coupling independently of other parameters. This allowed the output efficiency of the device to be optimized over a range of beam currents and operating frequencies.

The theory of stable, single-mode QOG operation based on sideband suppression by the dominant mode has been compared to experimental data for the first time. The theory extends previous theoretical work on the stability of free electron lasers [24] to the QOG with an annular beam [23]. The data confirms the prediction of significant regions of single-mode operation in a highly overmoded system without the application of mode stabilization or selection techniques. The annular beam geometry was found to have a strong effect on the single-mode stability: the stable parameter region is reduced relative to the pencil beam case due to the less effective sideband suppression by the main mode. The mode density in the present configuration is moderate: the mode frequency separation of $\sim 0.6\%$ leads to about 5 modes within the interaction bandwidth. Nevertheless, the region of stable operation is not expected to be greatly affected for configurations with much greater mode density, as may be needed in higher-frequency, megawatt-average-power systems.

As is the case for many high-power millimeter-wave experiments, the greatest unknown here is the value of the electron beam velocity pitch ratio, α , and its spread. Numerical modeling is difficult at best, and actual experimental measurements are even more so and have not been made. The achievable value of α is typically limited in this experiment by arcing in the electron gun circuit. This can be caused by magnetic mirroring of a portion of the electron beam, or by some of the beam electrons intercepting the focusing electrodes in the gun. Each of these causes may be controlled by varying the magnetic field (amplitude and shape) in the electron gun region which is accomplished by varying the currents in the two trim coils. When maximum power was desired, the trim coils were varied accordingly and operation was limited by arcing. Usually the spectrum obtained in this manner was not

single-moded, although occasionally at high beam current it was. To obtain single-mode operation it was frequently necessary to adjust the trim coil currents to a region of reduced operating power and presumably lower α . Consistent with the threshold current data, α values of 1.5 are considered to be achievable at low currents. However, due to the spread in α , the average α must be decreased as the current is increased to prevent arcing. The amount of this decrease in average α is certainly debatable; however $\alpha = 1$ seems to yield reasonably good agreement between theory and experiment at currents above 15 amps. For some of the single-mode operation at these high currents, α values as low as 0.65 yield consistency between theory and experiment.

The accuracy of the theoretical modeling of the experiment is limited by the uncertainty in the resonator Q factor as well as the uncertainty in the beam α . Cold tests are currently in progress which should yield accurate data for the resonator Q as a function of mirror separation. This data should resolve the discrepancy, discussed in Section IV, between the Q factor inferred from threshold current measurements and the scalar diffraction theory result.

Although the fraction of the total power lost which is dissipated in ohmic heating is high in the present configuration, the ohmic heating density is relatively low. In the case of operation at 125 kW and a frequency of 120 GHz—demonstrated in this experiment with a 23 cm mirror separation and a 47 kG magnetic field—the average heating density (during the pulse) on the mirrors was 0.6 kW/cm². This is well within the ohmic heating limit of a few kW/cm² for CW applications. The peak heating density (at the center of the mirror) for this case was 3 kW/cm². The resonator used in this experiment has $g \sim 0.3$. The ohmic heating density could be reduced by a factor of four without changing the interaction parameters (except for mode density) by decreasing g to -0.65 and increasing the mirror separation to 75 cm.

In conclusion, a CW relevant quasi-optical gyrotron experiment has been performed that substantiates many of the pertinent theories and demonstrates an understanding of the basic physics of the QOG. The model used for the annular beam predicted very well the change in the threshold current as the electron beam was translated relative to the cavity

standing wave pattern. Threshold currents themselves were also in good agreement with calculated values, with differences attributable to the imprecise knowledge of some of the relevant parameters such as the α value of the electron beam. Frequency measurements were obtained for several widely varied values of the magnetic field, electron beam current, electron gun voltage, mirror separation, and electron beam alignment relative to the cavity fields. With the exception of a few observed frequencies attributable to oscillations in the drift tube region (i.e. near the peak of the magnetic field), each frequency measurement was consistent with a TEM_{00} mode oscillating in the resonant cavity. Essentially, the higher-order TEM modes were effectively suppressed due to their higher diffraction losses. As discussed above, regions of single-mode operation and efficiency are well predicted by a relatively recently developed theory. Finally, efficiency optimization as a function of current and mirror separation has been demonstrated. To within the limits that α is known, if the value of $QI/d \sim I/T$ is held constant, the efficiency remains unchanged.

A series of several experiments are planned for the future. Immediate plans include the incorporation of a higher-power electron gun capable of producing 50 amps at 80 kV. This electron beam has a diameter of 1 cm in the resonant cavity, necessitating modification of the drift tube, and the collector will also be modified to handle the higher-power beam. During these modifications, a probe will be added to measure any buildup of charge that may be trapped between the two peaks of the magnetic field. One benefit of using this electron gun will be a better characterized electron beam, with average values of $\alpha \approx 1.5$ considered accessible at high currents, implying a much lower spread in α than in the experiment described here. The higher input power from the electron gun will make possible the use of a resonator with larger output coupling, again to keep the product $I/T \sim QI/d$ the same as the lower-power experiments. Since the ohmic losses remain nearly constant, the total Q value for the cavity will be essentially unaffected by the ohmic Q , resulting in the measured efficiency being essentially equal to the electronic efficiency. This fact will make interpretation of the data and comparison to theory more straightforward. One value to be determined by the experiment will be the maximum value of current that can be propagated through the resonant cavity. To enhance this value, provision has been

made to add a DC electric field parallel to the magnetic field, possibly increasing the amount of current that can be propagated through the cavity. A gyrokystron experiment is also planned, incorporating a quasi-optical prebunching cavity with low mode density (essentially single-moded) in addition to the overmoded output cavity. The circulating power in the prebunching cavity will be low, allowing the use of a short mirror separation while maintaining CW relevance.

VIII Acknowledgements

We thank Drs. Steven Gold, Victor Granatstein, Robert McCowan, and John Burke for helpful discussions, and we thank Robert Lee for carrying out many of the computer calculations. This work was supported by the Office of Fusion Energy of the Department of Energy and by the Office of Naval Research.

A Appendix: Calorimeter Calculations

The calorimeter described here consisted of a conducting plate covered with a layer of lossy dielectric material (paint). The analysis of this situation is given here for the case of a general dielectric material. The geometry is shown in Figure 19 for the case of the electric field of the incident radiation perpendicular to the plane of incidence. The electric fields of the plane wave incident (\vec{E}_1^+) on and reflected (\vec{E}_1^-) by the dielectric as well as the forward (\vec{E}_2^+) and reflected (\vec{E}_2^-) waves in the dielectric are given by:

$$\vec{E}_1^\pm = \hat{y} E_1^\pm e^{i(\omega t - \vec{k}_1^\pm \cdot \vec{r})} \quad (1)$$

$$\vec{E}_2^\pm = \hat{y} E_2^\pm e^{i(\omega t - \vec{k}_2^\pm \cdot \vec{r})} \quad (2)$$

where $\omega = 2\pi f$ is the angular frequency of the radiation, \vec{k} is the wave number, \vec{r} is the position vector, \hat{y} is the unit vector in the y direction and:

$$\vec{k}_1^\pm \cdot \vec{r} = k_1(x \sin \theta_i \pm z \cos \theta_i) \quad (3)$$

$$\vec{k}_2^\pm \cdot \vec{r} = k_2(x \sin \theta_t \pm z \cos \theta_t) \quad (4)$$

where θ_i is the angle of incidence and θ_t is the angle of transmittance shown in Figure 19. In region 1 (free space), the wave number is real, but \vec{k} is complex in the lossy dielectric of region 2:

$$k_2 = \omega \sqrt{\mu_2 \epsilon_2} \quad (5)$$

$$\epsilon_2 = \epsilon_{r2} \epsilon_0 (1 - i \tan \delta) \quad (6)$$

where the permeability of the dielectric, μ_2 , is assumed equal to μ_0 , the permeability of free space, ϵ_0 is the permittivity of free space, ϵ_{r2} is the real part of the dielectric constant relative to free space, and $\tan \delta$ is the loss tangent of the dielectric. The total electric fields in regions 1 and 2 are given by:

$$\vec{E}_1 = \vec{E}_1^+ + \vec{E}_1^- \quad (7)$$

$$\vec{E}_2 = \vec{E}_2^+ + \vec{E}_2^- \quad (8)$$

and E_i^\pm are the peak electric field strengths of the waves travelling in the $\pm z$ direction. Here we desire to calculate the reflection coefficient of the dielectric layer, i.e. we wish to calculate E_1^-/E_1^+ , and do so by applying the appropriate boundary conditions.

First note that the tangential electric field is zero at $z = d$, leading to the equation

$$E_2^+ = -E_2^- e^{i2k_2 d \cos \theta_t}. \quad (9)$$

The fact that the tangential electric field is continuous across the boundary at $z = 0$ leads to Snell's Law,

$$k_1 \sin \theta_i = k_2 \sin \theta_t, \quad (10)$$

and

$$E_1^+ + E_1^- = E_2^+ + E_2^-. \quad (11)$$

The tangential part of the magnetic intensity (\vec{H}_{tan}) is also continuous at $z = 0$, which implies

$$E_1^- - E_1^+ = \left(\frac{\cos \theta_t}{\cos \theta_i} \right) \frac{\epsilon_2}{\epsilon_o} (E_2^- - E_2^+). \quad (12)$$

Using Eq.(9) and performing some algebra yields an equation for the complex reflection coefficient,

$$\frac{E_1^-}{E_1^+} = \frac{1 - D}{1 + D}, \quad (13)$$

where

$$D = \left(\frac{\cos \theta_t}{\cos \theta_i} \right) \sqrt{\frac{\epsilon_2}{\epsilon_o}} \left\{ \frac{1 + e^{-i2k_2 d \cos \theta_t}}{1 - e^{-i2k_2 d \cos \theta_t}} \right\}. \quad (14)$$

The power reflection coefficient is

$$R = \left| \frac{1 - D}{1 + D} \right|^2. \quad (15)$$

A similar calculation for the electric field of the incident radiation parallel to the plane of incidence yields

$$R = \left| \frac{1 - D'}{1 + D'} \right|^2, \quad (16)$$

where

$$D' = \left(\frac{\cos \theta_i}{\cos \theta_t} \right) \sqrt{\frac{\epsilon_2}{\epsilon_o}} \left\{ \frac{1 + e^{-i2k_2 d \cos \theta_t}}{1 - e^{-i2k_2 d \cos \theta_t}} \right\}. \quad (17)$$

B References

- [1] K. Felch *et al.*, *Int. J. Elec.* **61**, 701 (1986).
- [2] K.E. Kreischer and R.J. Temkin, *Phys. Rev. Lett.* **59**, 547 (1987); K.E. Kreischer, *Bull. Amer. Phys. Soc.* **33**, 1913 (1988).
- [3] P. Sprangle, J. Vomvoridis and W.M. Manheimer, *Phys. Rev. A* **23**, 3127 (1981).
- [4] A. Bondeson, W.M. Manheimer and E. Ott, *Infrared and Millimeter Waves*, ed. by K.J. Button, Vol. 7, Chapter 7, Academic Press (1983).
- [5] B. Levush and W.M. Manheimer, *Int. J. Infrared and Millimeter Waves* **4**, 877 (1983).
- [6] B. Levush *et al.*, *Int. J. Elec.* **54**, 749 (1983).
- [7] T.A. Hargreaves *et al.*, *Int. J. Elec.* **57**, 977 (1984).
- [8] M.E. Read *et al.*, *Int. J. Elec.* **65**, 309 (1988).
- [9] Y. Zhonghai and L. Shenggang, *Int. J. Elec.* **57**, 1003 (1984).
- [10] X. Kongyi and L. Shenggang, *Int. J. Elec.* **57**, 1019 (1984).
- [11] E.C. Morse and R.V. Pyle, *J. Vacuum Sci. and Tech. A* **3**, 1239 (1985).
- [12] Y. Itoh *et al.*, *Conference Digest of the Thirteenth International Conference on Infrared and Millimeter Waves*, Honolulu, HI (December 1988).
- [13] Presented at the Thirteenth International Conference on Infrared and Millimeter Waves, Honolulu, HI (December 1988).
- [14] A. Yariv, *Optical Electronics*, CBS College Publishing (1985).
- [15] A. Perrenoud, T.M. Tran, M.Q. Tran, C. Rieder, M. Schleipen, and A. Bondeson, *Int. J. Elec.*, **57**, 985, (1984).

- [16] J.L. Seftor, A.T. Drobot and K.R. Chu, *IEEE Trans. on Elec. Dev.* **ED-26**, 1609 (1979).
- [17] W.B. Herrmannsfeldt, *SLAC Report 226*, (1979).
- [18] K.E. Kreischer, B.G. Danly, J.B. Schutkeker, and R.J. Temkin, *IEEE Trans. on Plasma Science* **PS-13**, 364 (1985).
- [19] A.K. Ganguly and K.R. Chu, *Int. J. Infrared and Millimeter Waves* **5**, 103 (1984).
- [20] B.G. Danly and R.J. Temkin, *Phys. Fluids* **29**, 561 (1986).
- [21] T.M. Tran, B.G. Danly, K.E. Kreischer, J.B. Schutkeker, and R.J. Temkin, *Phys. Fluids* **29**, 1274 (1986).
- [22] M.Q. Tran, A. Bondeson, A. Perrenoud, S. Alberti, B. Isaak, and P. Muggli, *Int. J. Elec.* **61**, 1029, (1986).
- [23] T. Antonsen, B. Levush and W.M. Manheimer, to be published.
- [24] T.M. Antonsen, Jr. and B. Levush, *Phys. Rev. Lett.* **62**, 1488 (1989).

TABLE I

Mirror Diameter ($2a$)	5.0 cm		
Radius of Curvature (R_c)	38.7 cm		
Mirror Separation (d)	20	24	28 cm
Frequency (f)	120 GHz		
Wavelength (λ)	0.25 cm		
Longitudinal Mode Spacing ($\Delta f/f$)	0.63	0.52	0.45 %
Radiation Waist Radius (ω_o)	1.16	1.19	1.22 cm
ω_o/λ	4.6	4.8	4.9
μ ($E = 70$ keV, $\alpha = 1.0$)	9.8	10.1	10.3
Transmission Coefficient (T , round trip)	0.5	1.5	2.2 %
Diffraction Quality Factor (Q_d)	198,000	80,000	61,000
Ohmic Quality Factor (Q_o)	354,000	400,000	470,000
Total Quality Factor (Q)	127,000	67,000	54,000
Fresnel Number ($a^2/\lambda d$)	1.25	1.04	0.89
$G ((1 - d/R_c)(a_1/a_2))$	0.48	0.38	0.28

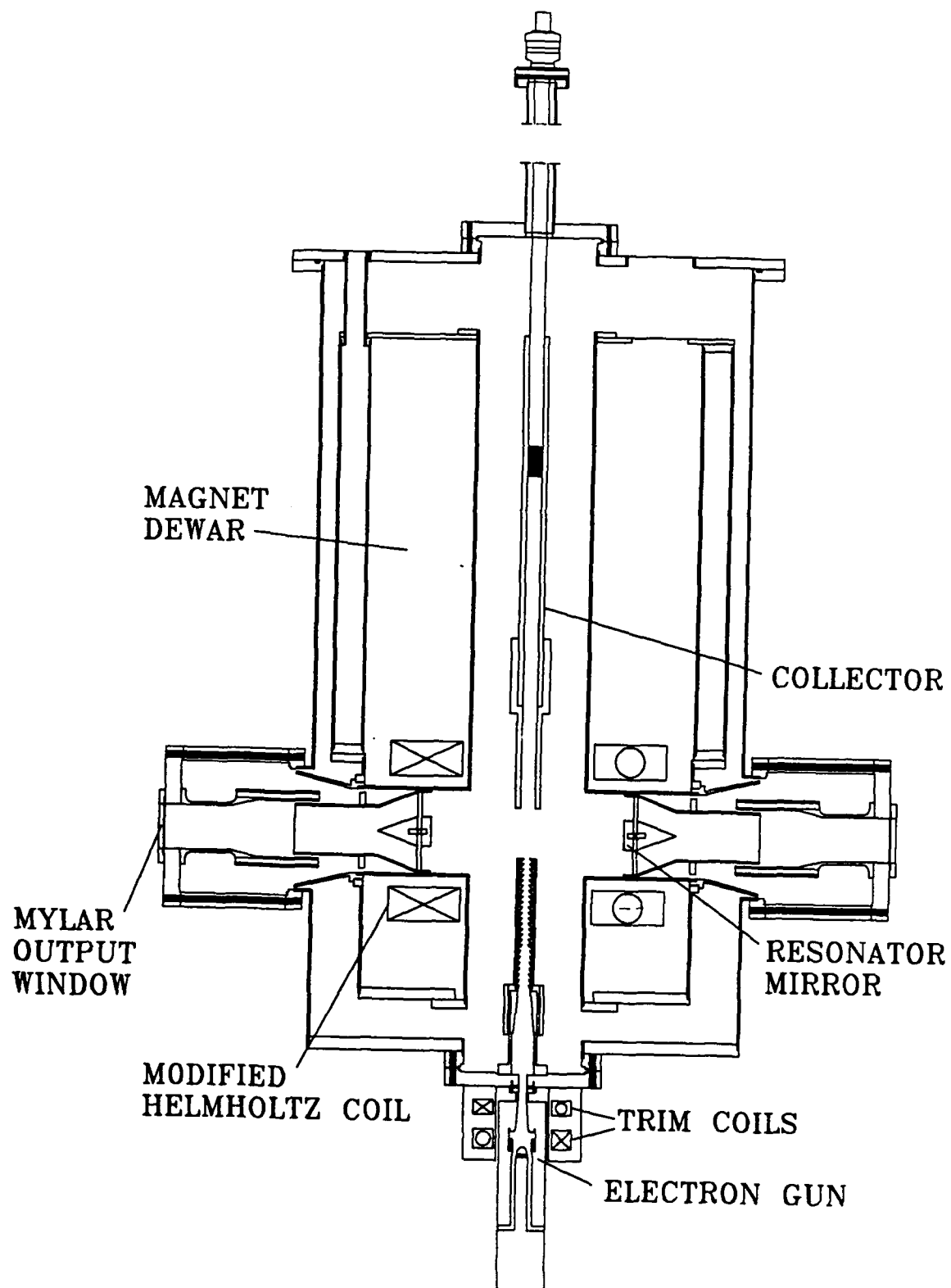


Figure 1 Schematic diagram of the NRL quasi-optical gyrotron experiment.

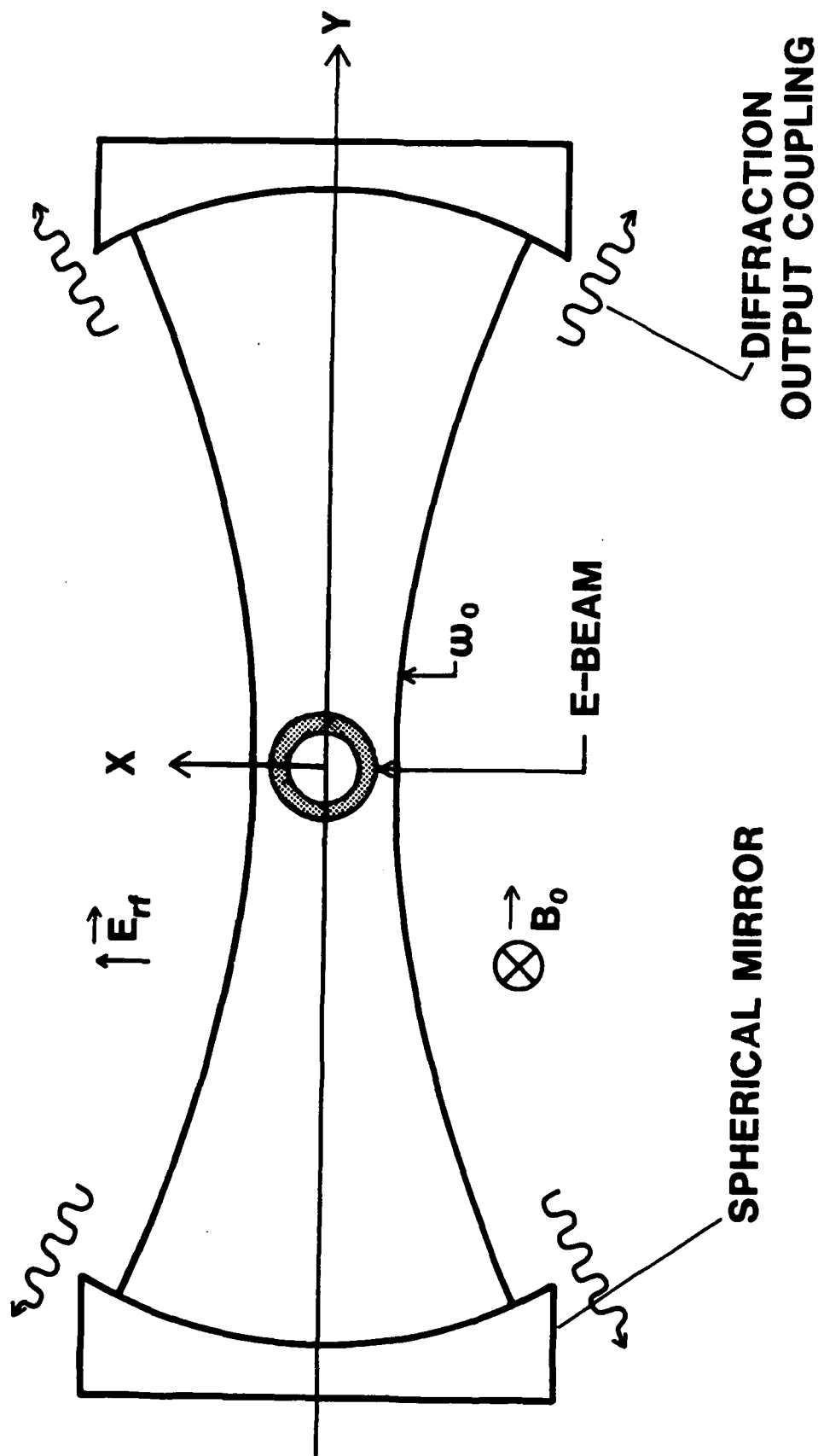


Figure 2 The quasi-optical gyrotron resonator showing the geometry of the external magnetic field (\vec{B}_0), the RF electric field (\vec{E}_{rf}), and the electron beam.

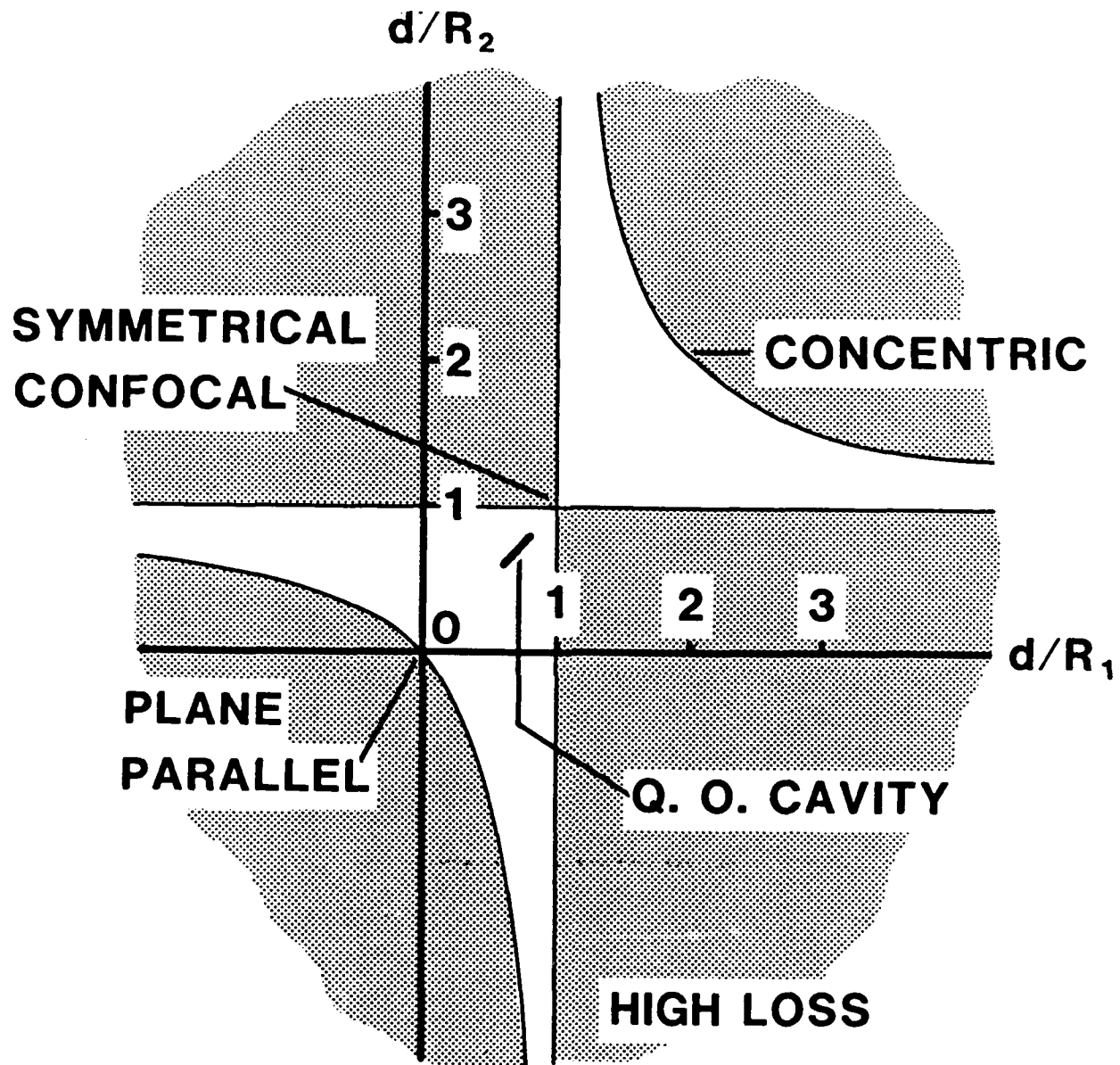


Figure 3 Open resonator stability diagram. The shaded (high-loss) areas are those in which the stability criterion $0 \leq (1 - d/R_1)(1 - d/R_2) \leq 1$ is not satisfied. Note that the experimental design lies well within the stable region.

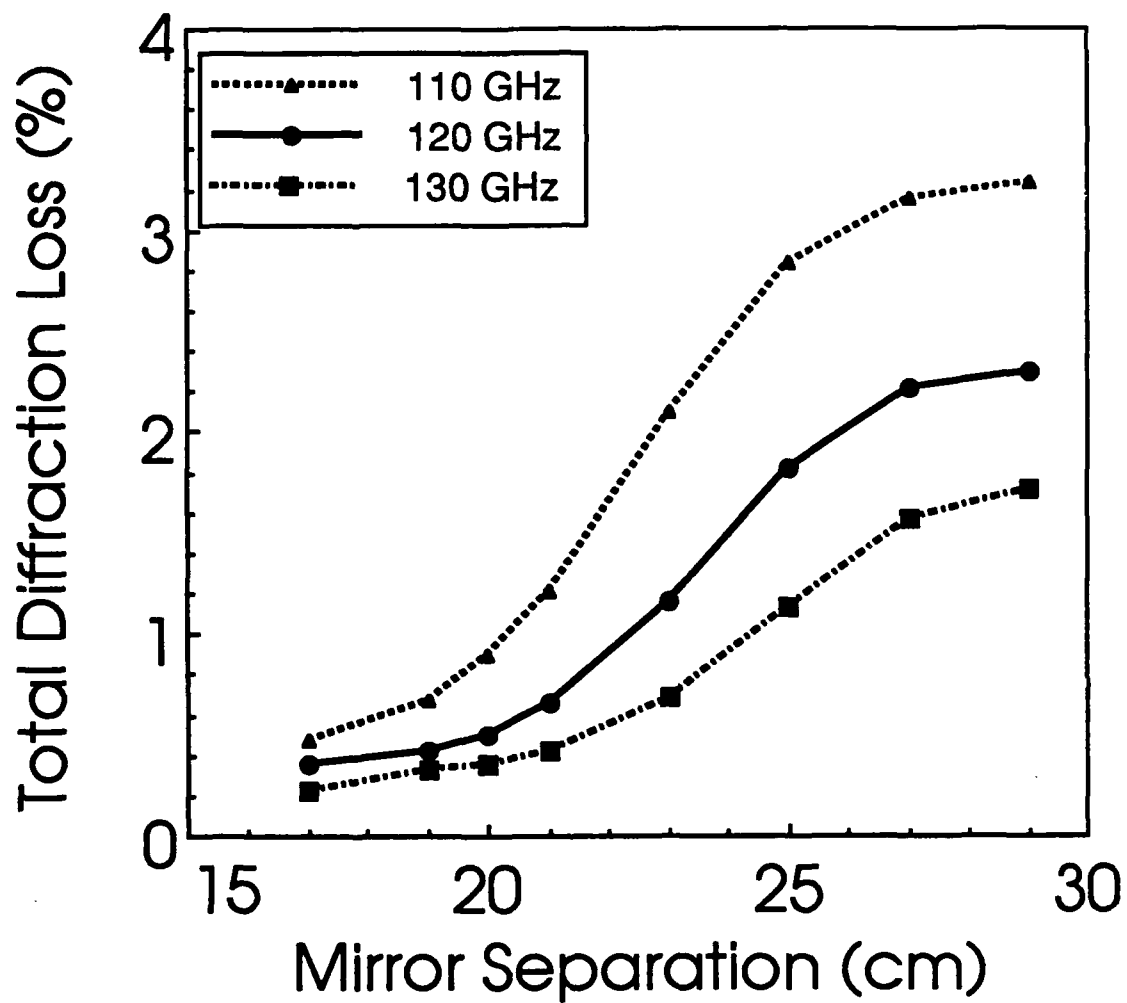


Figure 4 Cavity diffraction loss as a function of mirror separation for resonant frequencies of 110, 120 and 130 GHz. The 5 cm diameter cavity mirrors had a radius of curvature of 38.7 cm.

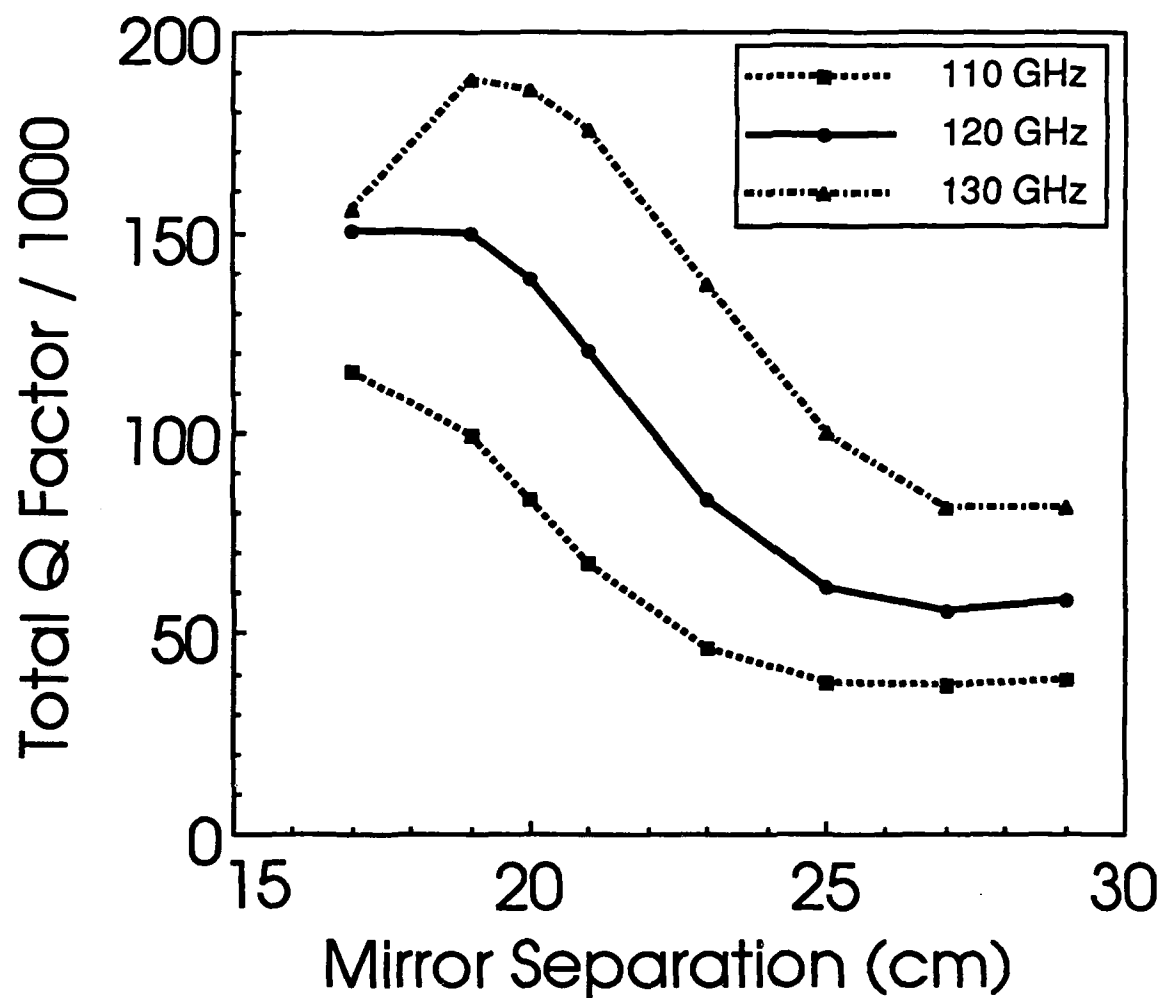


Figure 5 Resonant cavity quality factor (Q) including diffraction and ohmic losses as a function of mirror separation for resonant frequencies of 110, 120 and 130 GHz. The 5 cm diameter cavity mirrors had a radius of curvature of 38.7 cm.

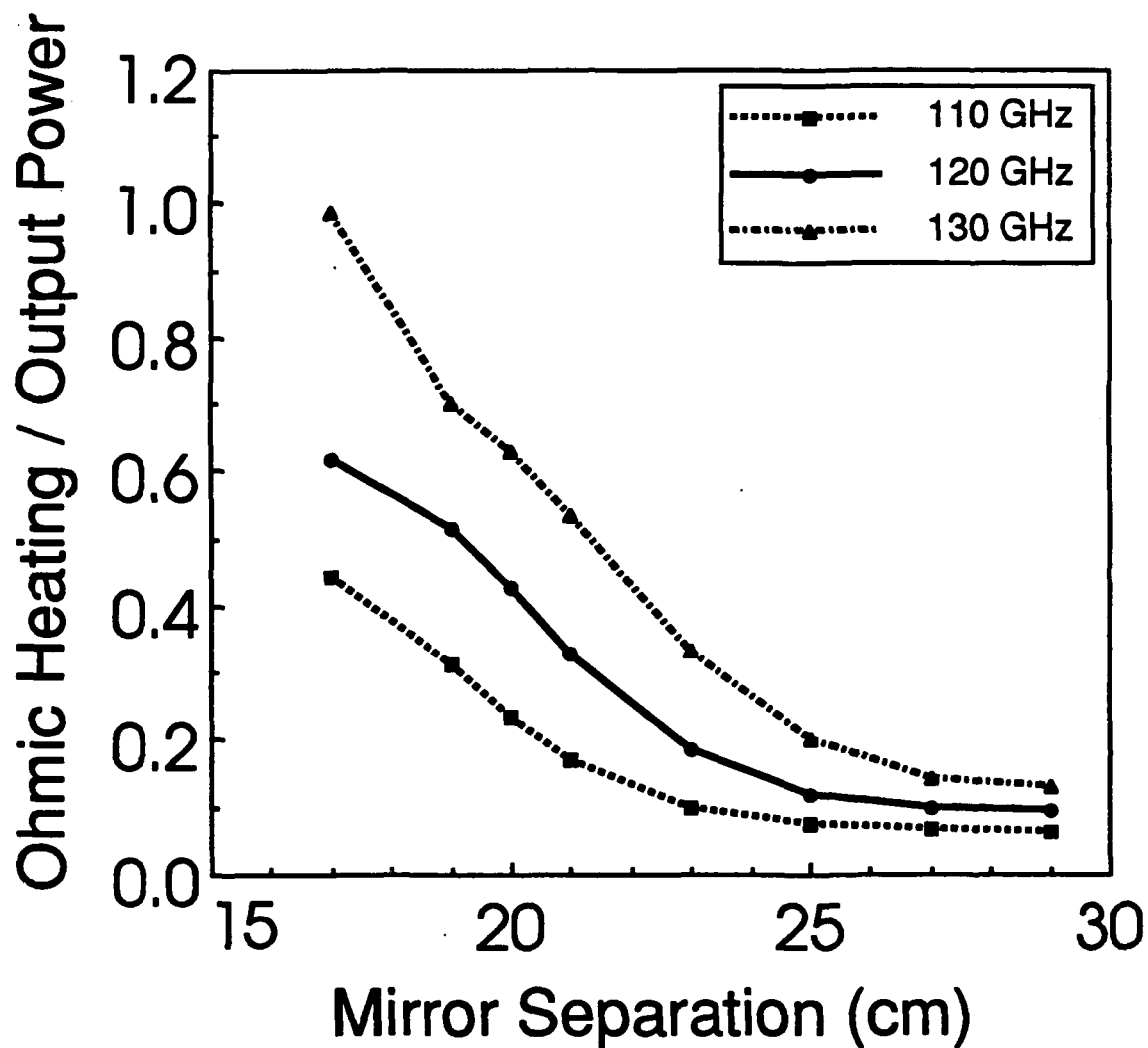


Figure 6 The ratio of power lost through ohmic heating of the cavity mirrors to the RF output power as a function of mirror separation for resonant frequencies of 110, 120 and 130 GHz. The 5 cm diameter cavity mirrors had a radius of curvature of 38.7 cm.

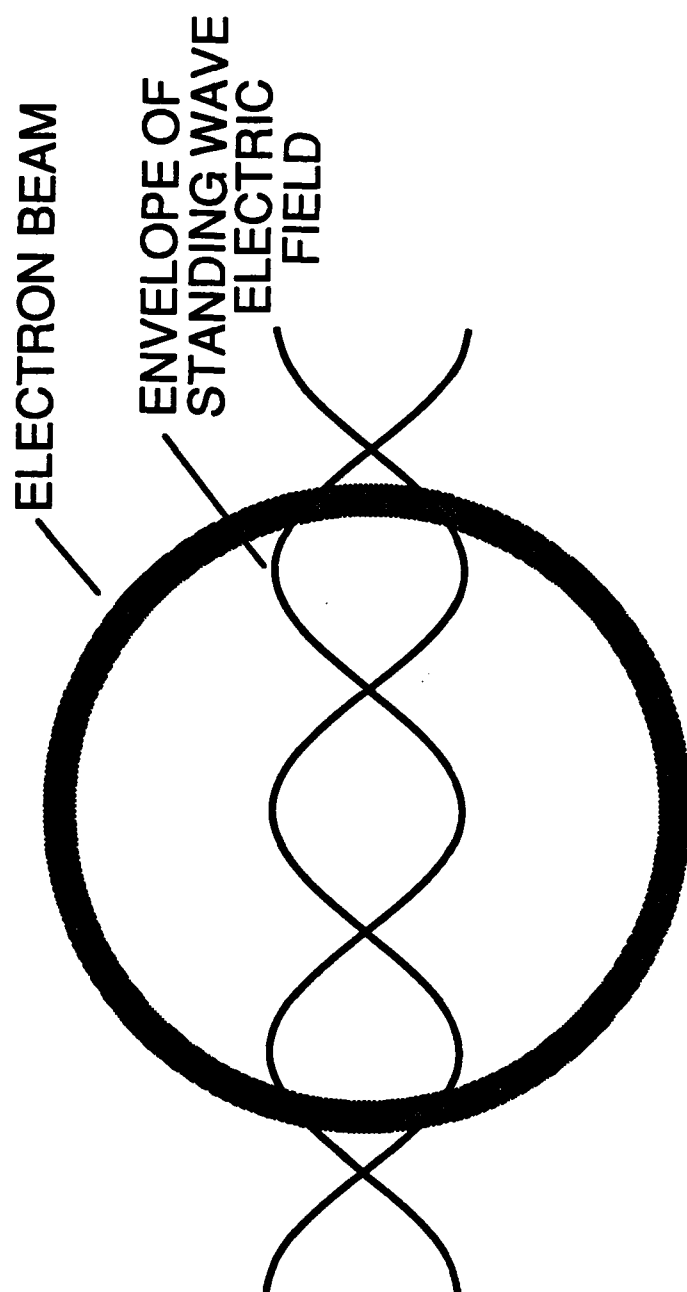


Figure 7 Geometry of the annular electron beam and the standing RF electric field (with the beam centered on the peak of the electric field).

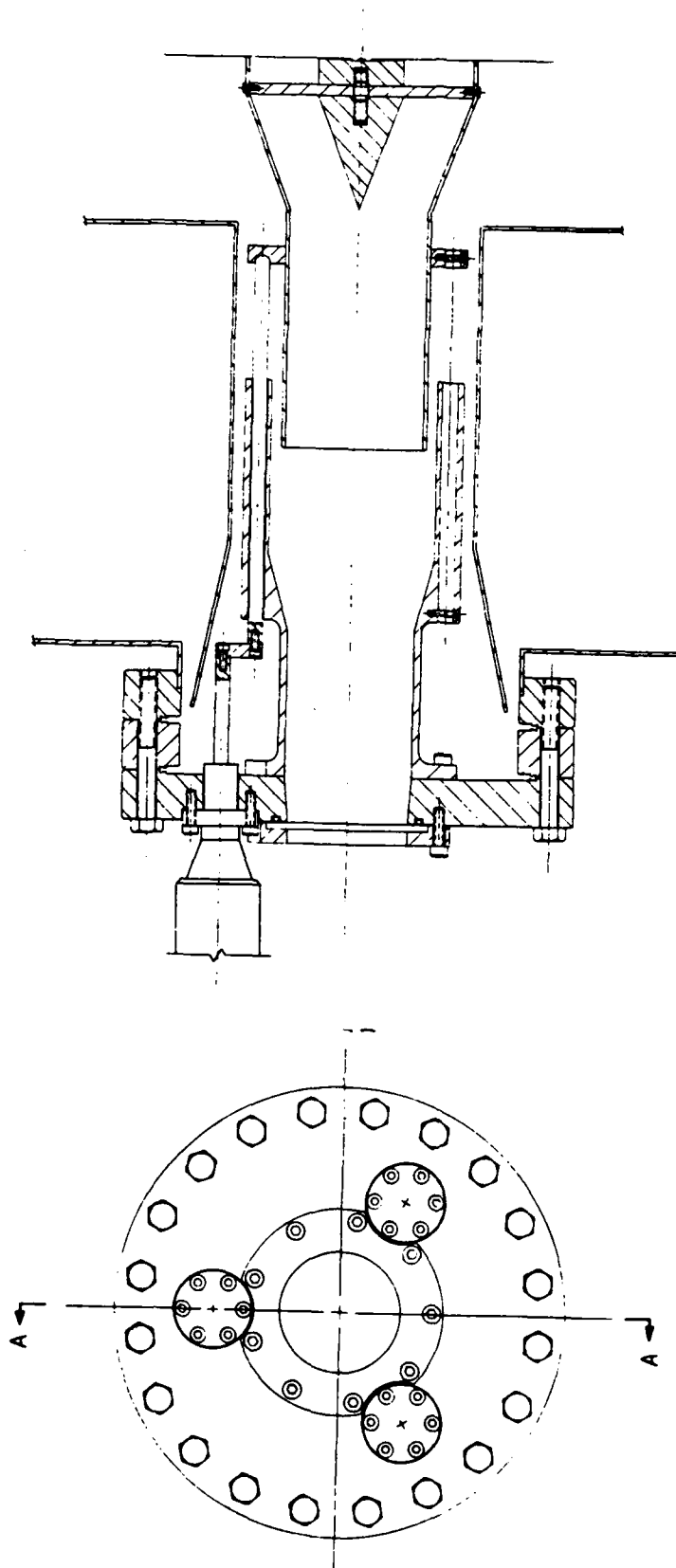


Figure 8 Adjustable resonant cavity mirror holder shown mounted in the superconducting magnet cross-bore.

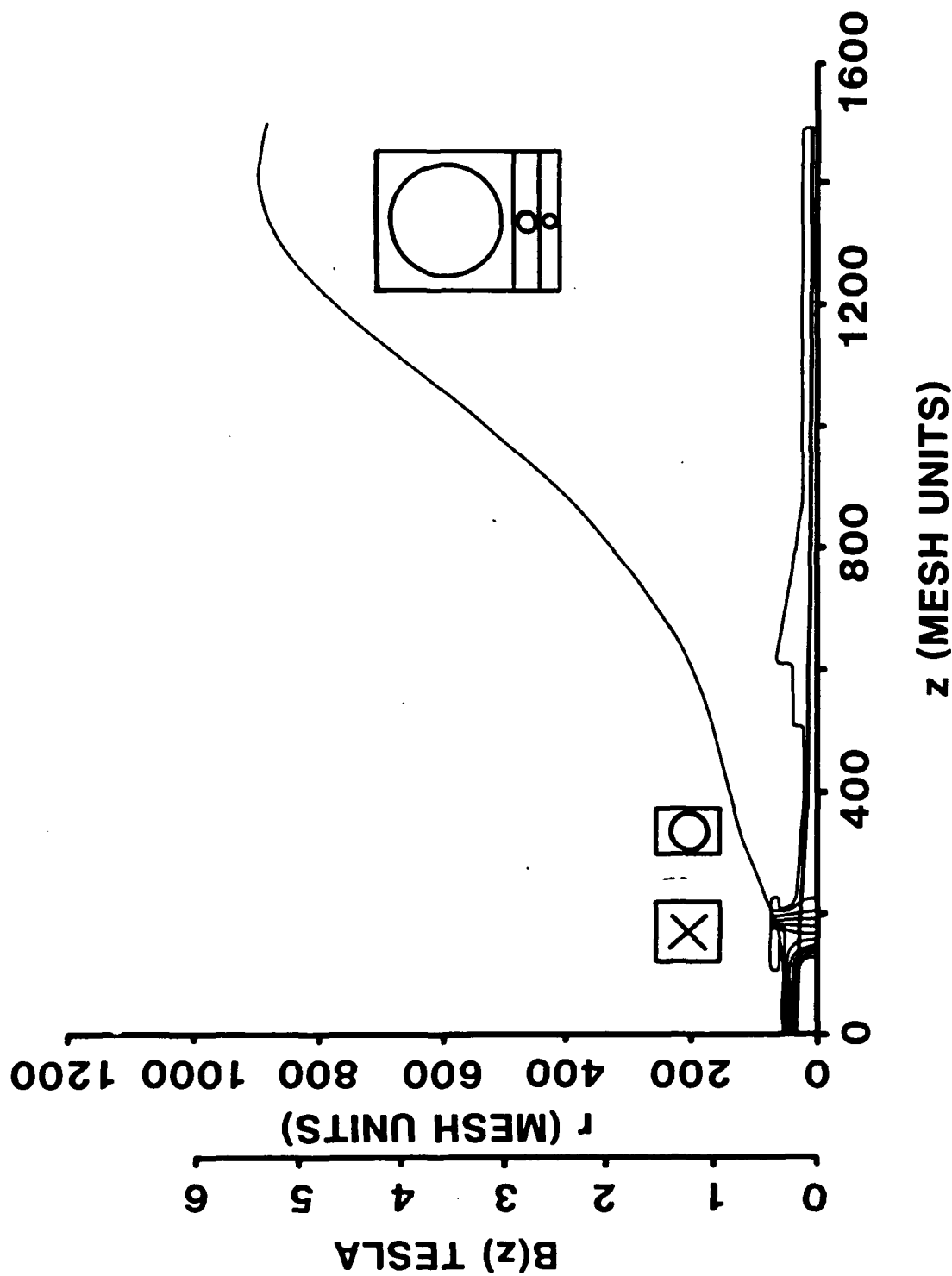


Figure 9 Electron gun geometry modeled using the Hermansfeldt electron trajectory code showing the calculated electron trajectories. Note in this calculation that 1 mesh unit = 0.25 mm.

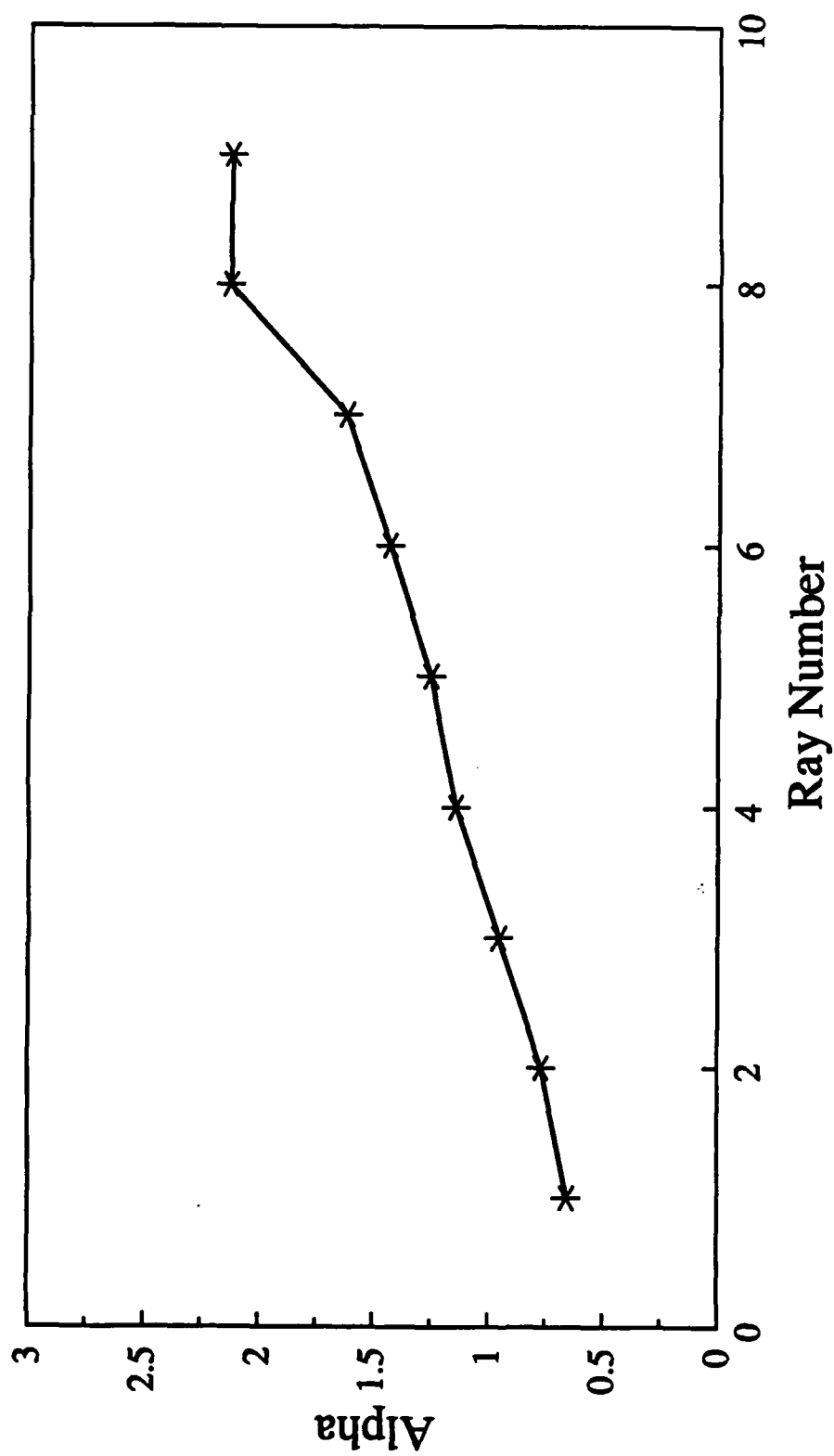


Figure 10 Alpha ($\alpha = v_{\perp}/v_{\parallel}$) values for different rays calculated by the Hermansfeldt electron trajectory code.

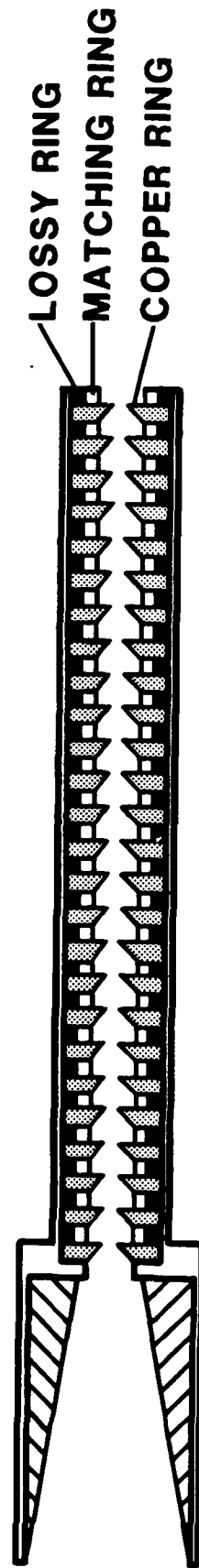


Figure 11 Drift tube design showing the lossy and matching dielectric rings and the copper scrapper rings.

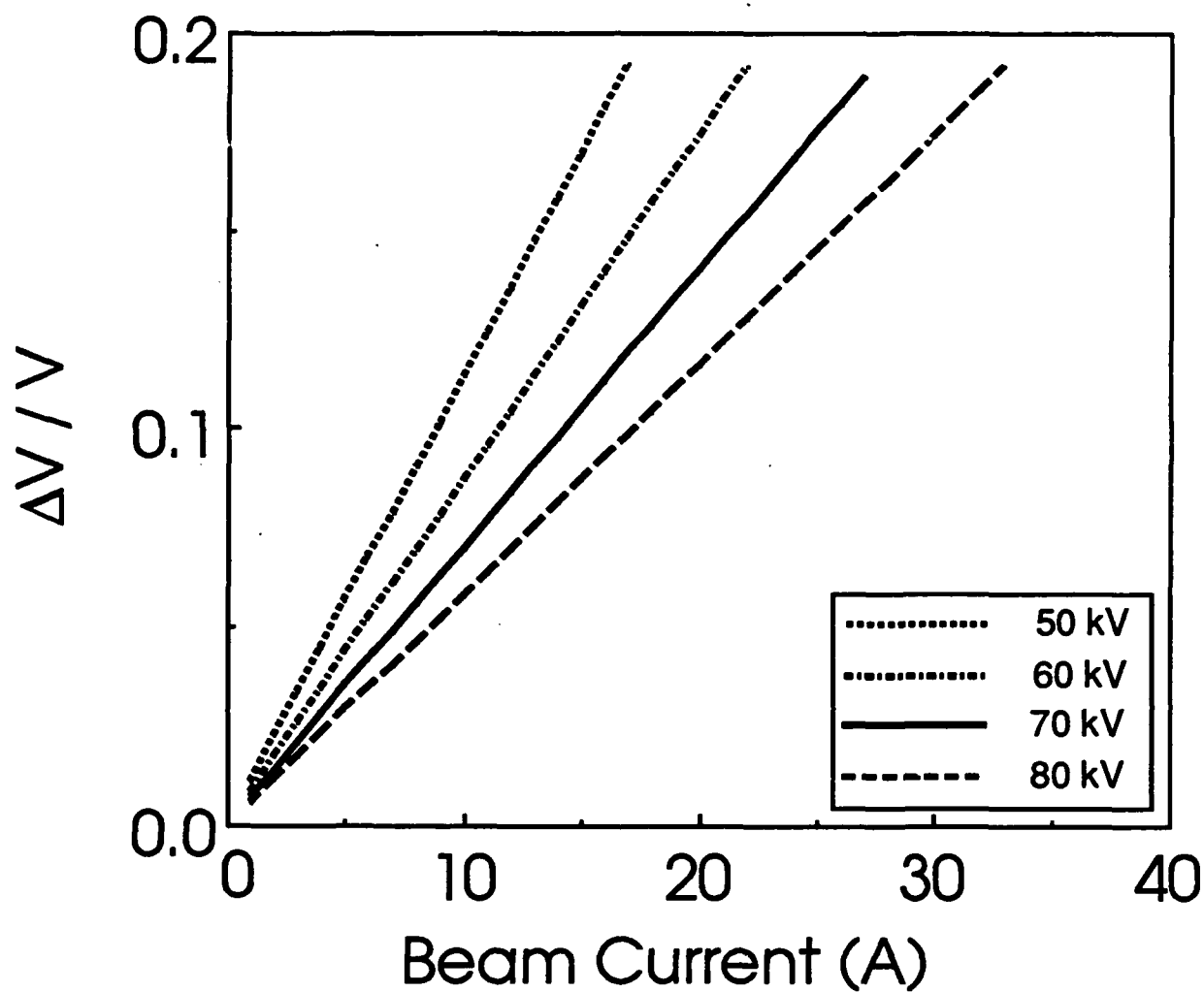


Figure 12 The space charge depression of the electron beam voltage as a function of the beam current for electron gun voltages of 50, 60, 70 and 80 kV. The momentum pitch ratio was assumed to be equal to 1.

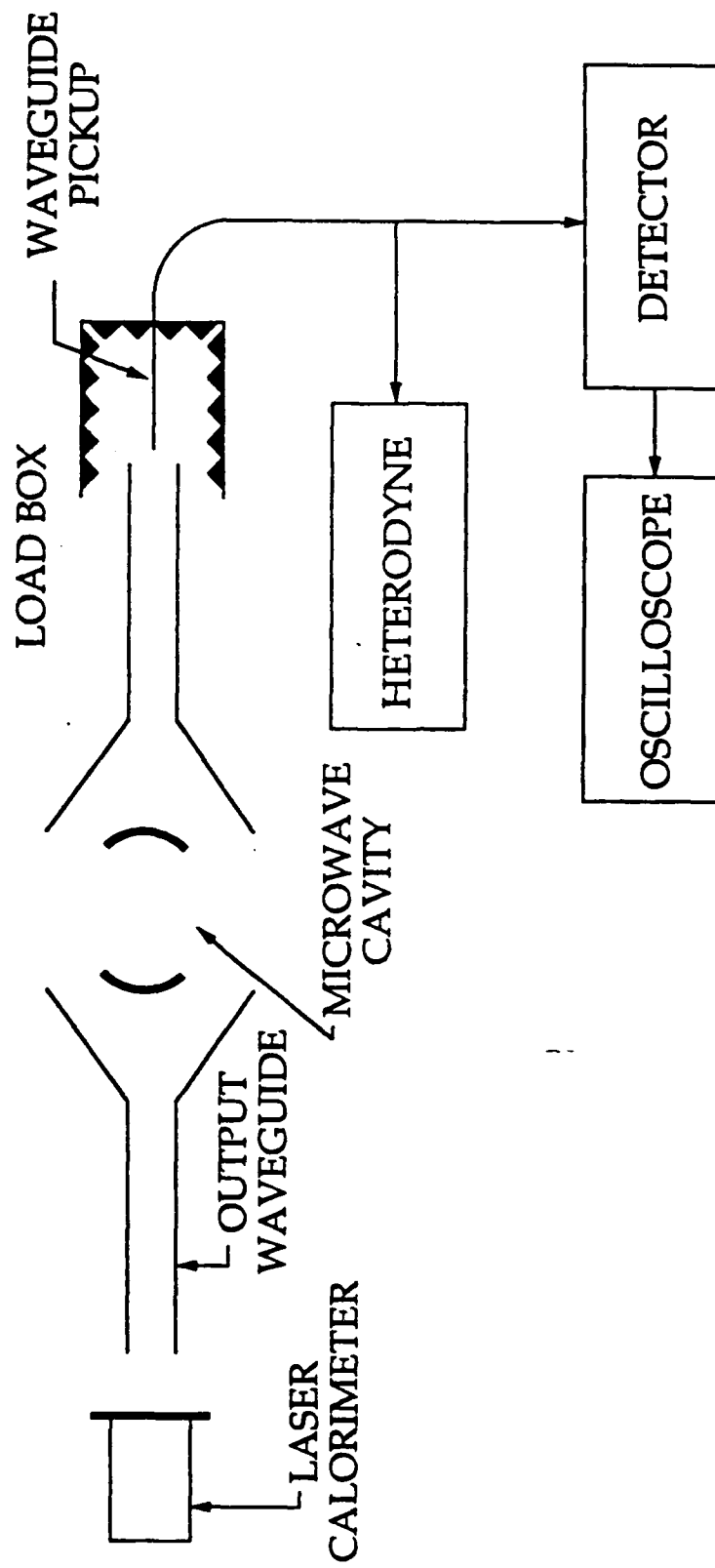


Figure 13 Resonant cavity and associated diagnostics.

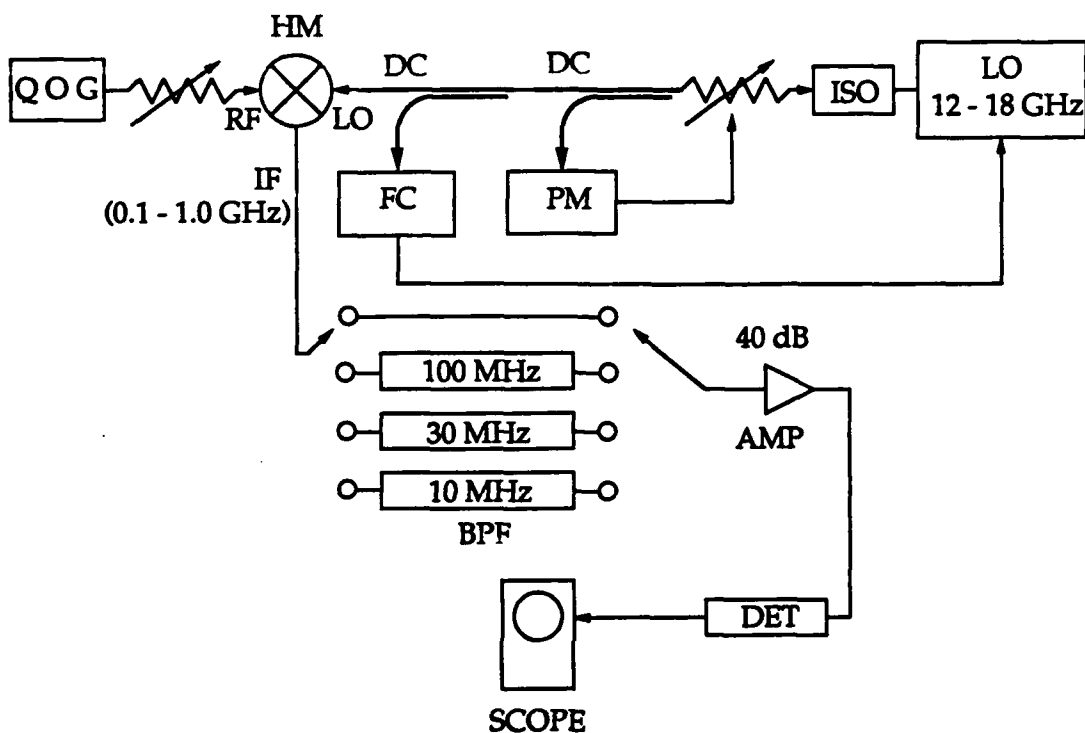


Figure 14 The heterodyne diagnostic used for frequency measurements. The local oscillator (LO) is frequency locked by the counter (FC) and power leveled by the power monitor (PM). The RF from the gyrotron (QOG) is mixed with the LO signal by the harmonic mixer (HM) and the IF signal is filtered by one of several bandpass filters (BPF) before being amplified (A), rectified (DET), and measured on an oscilloscope.

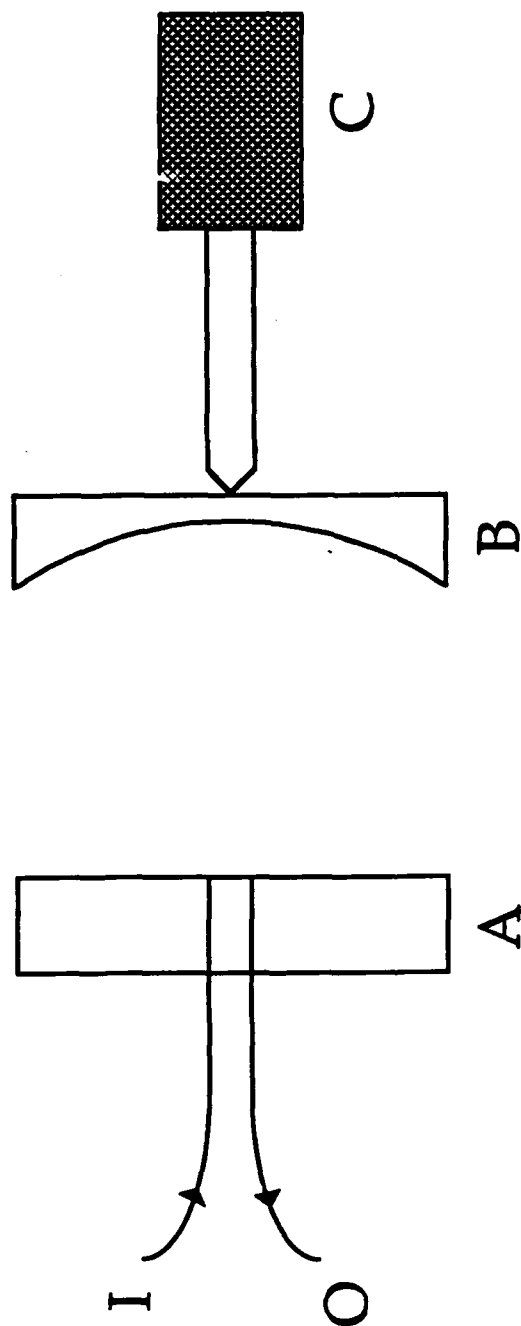


Figure 15 Schematic diagram of the Fabry-Perot interferometer used to measure the frequency. Radiation was input (I) from the experiment and coupled out (O) for detection through the planar mirror (A). The concave mirror (B) of the nearly semiconfocal resonator was movable through the use of a micrometer (C).

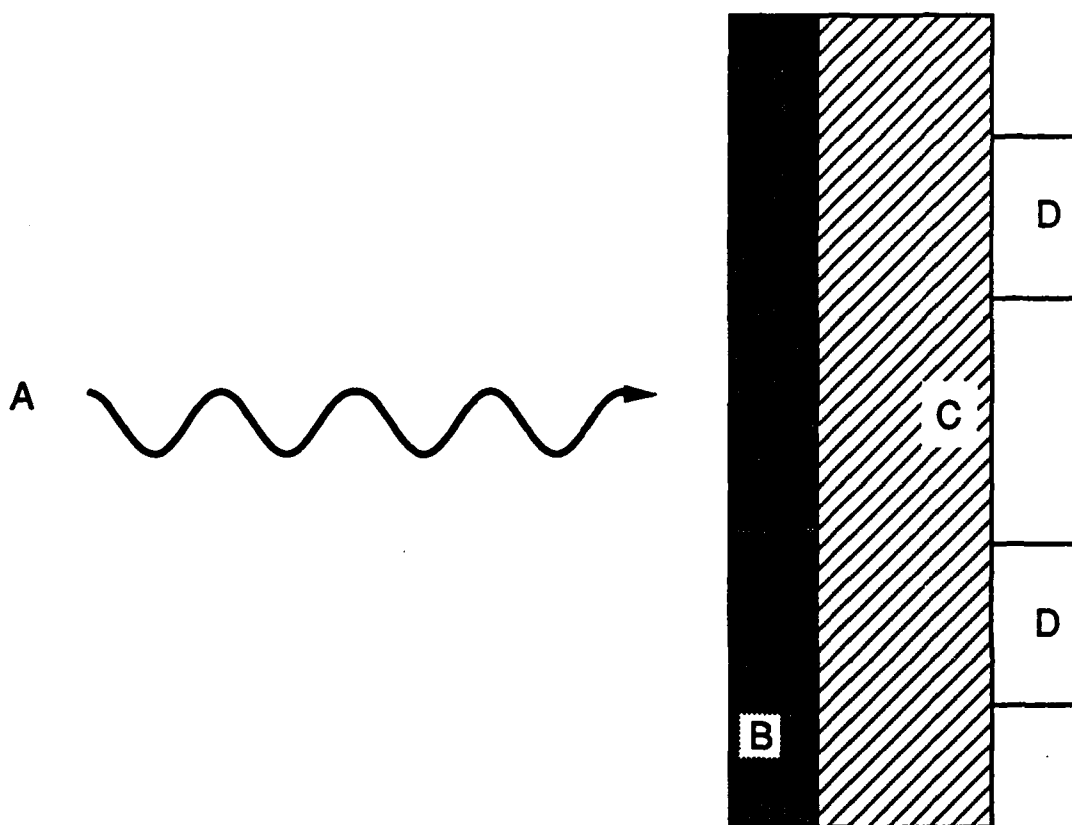


Figure 16 Modified laser calorimeter used to measure experimental output power. The incident radiation (A) is absorbed in the layer of paint (B) on an aluminum plate (C). The temperature rise is measured by thermopiles (D).

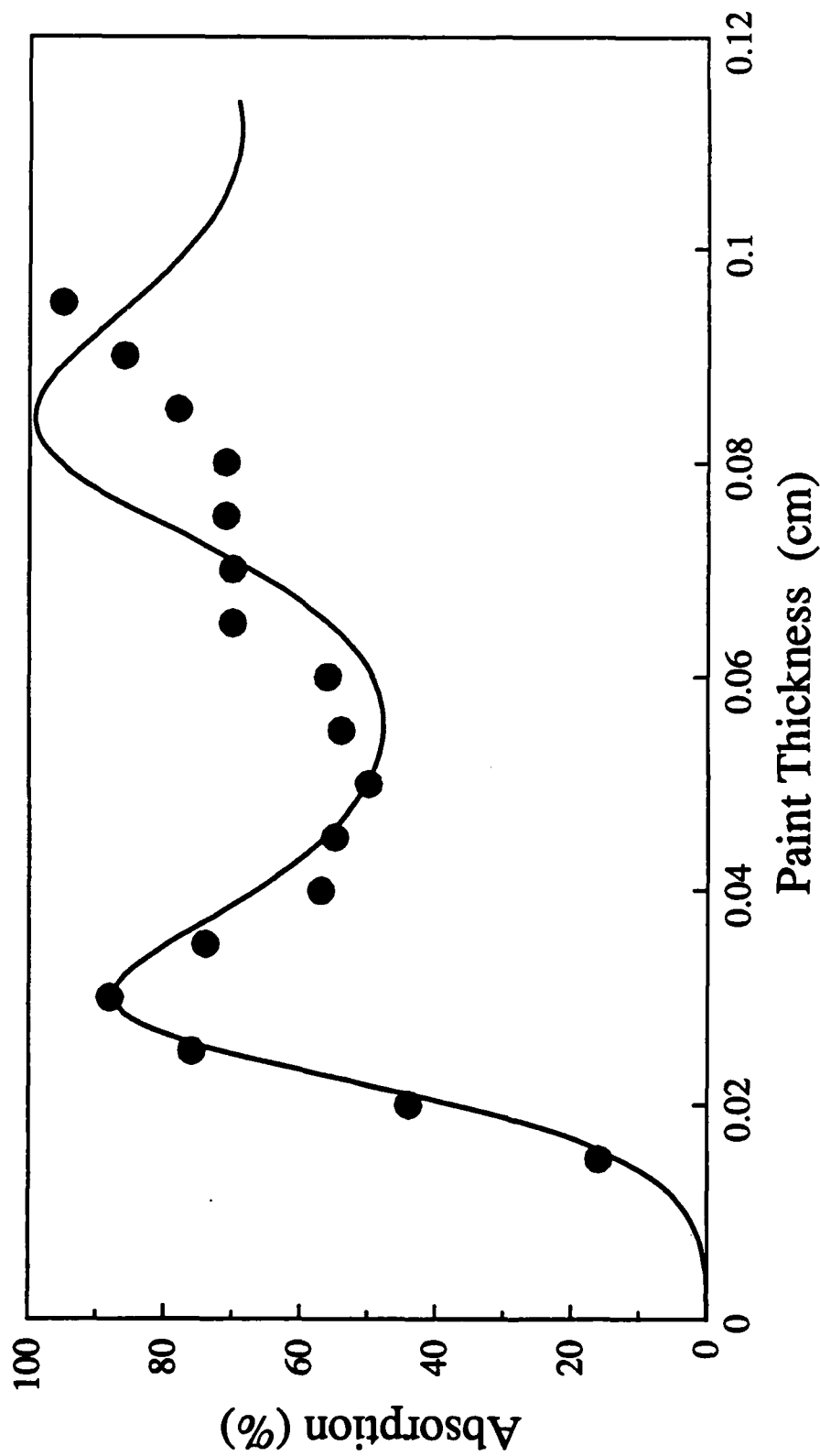


Figure 17 Measured (solid dots) and calculated (solid curve) calorimeter absorption as a function of lossy paint thickness . The calculations assumed $\epsilon_r = 5$ and $\tan(\delta) = 0.25$, and the thickness of each coat of paint was assumed to be equal.

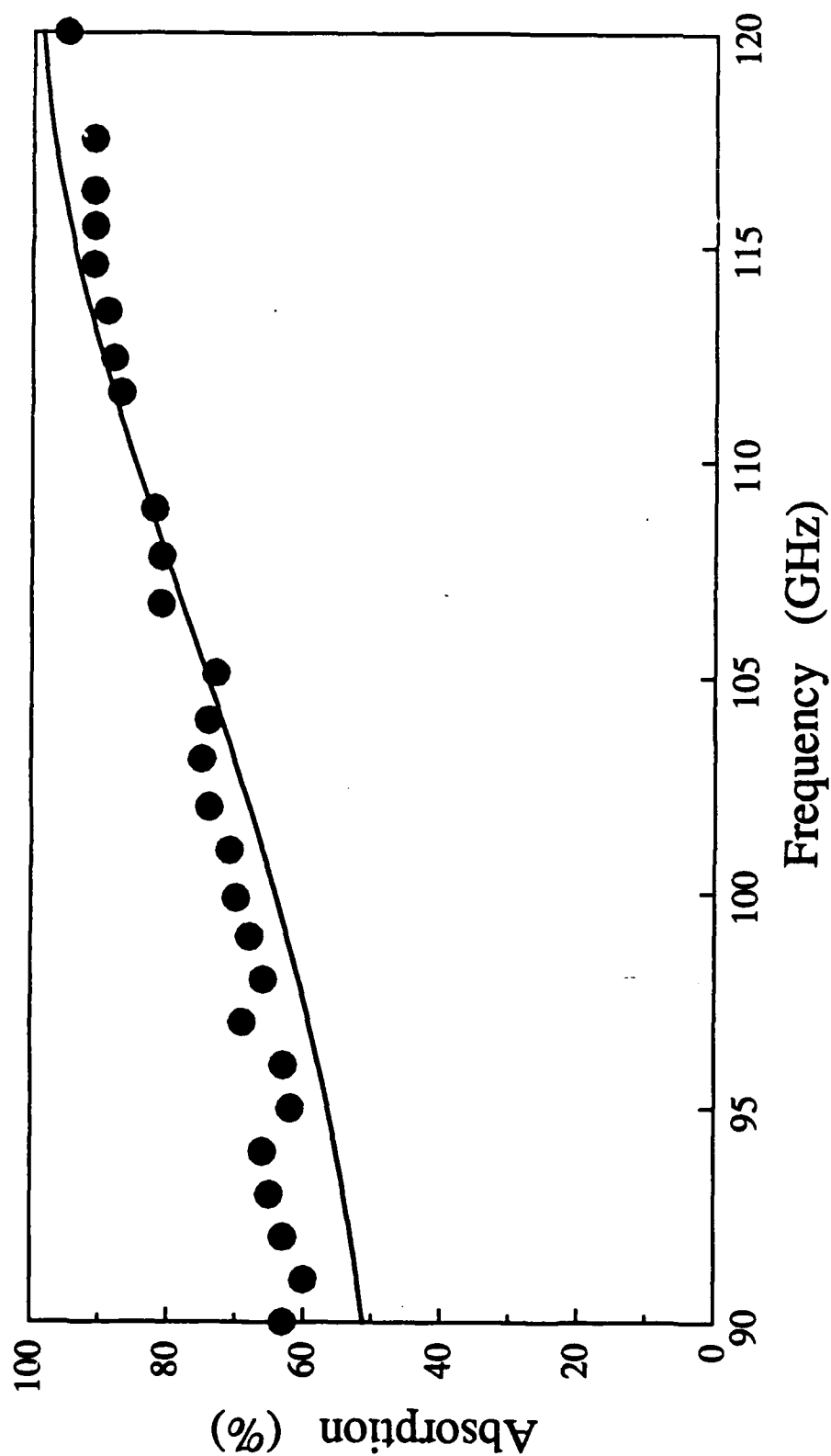


Figure 18 Measured (solid dots) and calculated (solid curve) calorimeter absorption as a function of incident RF frequency. The calculations assumed $\epsilon_r = 5$ and $\tan(\delta) = 0.25$.

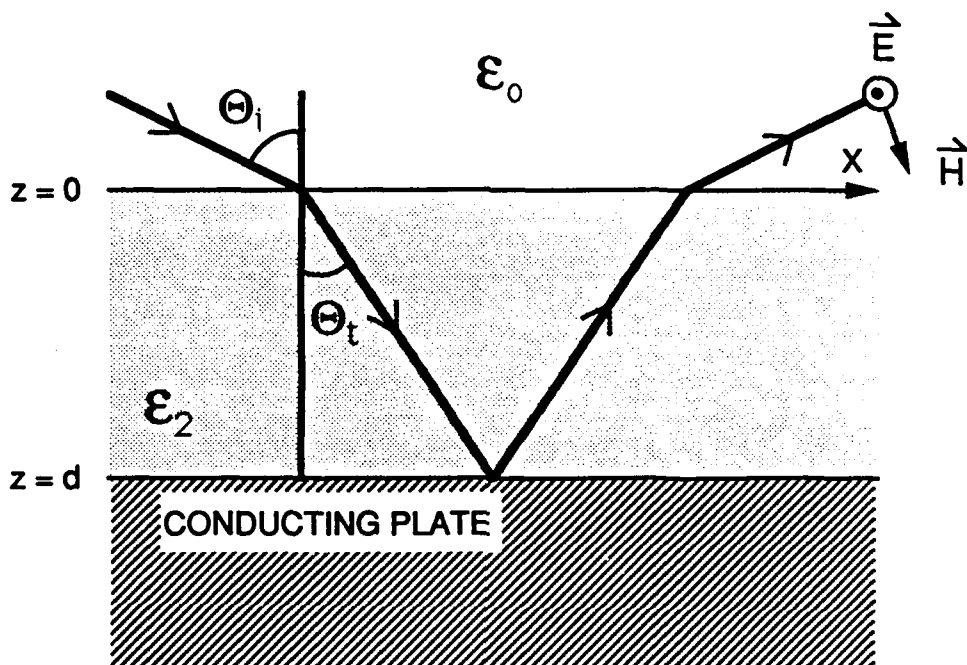


Figure 19 Geometry used to calculate the calorimeter absorption showing the angles of incidence (θ_i) and transmittance (θ_t), the dielectric constants of free space (ϵ_0) and of the absorbing paint (ϵ_2) and the RF electric (\vec{E}) and magnetic (\vec{H}) fields.

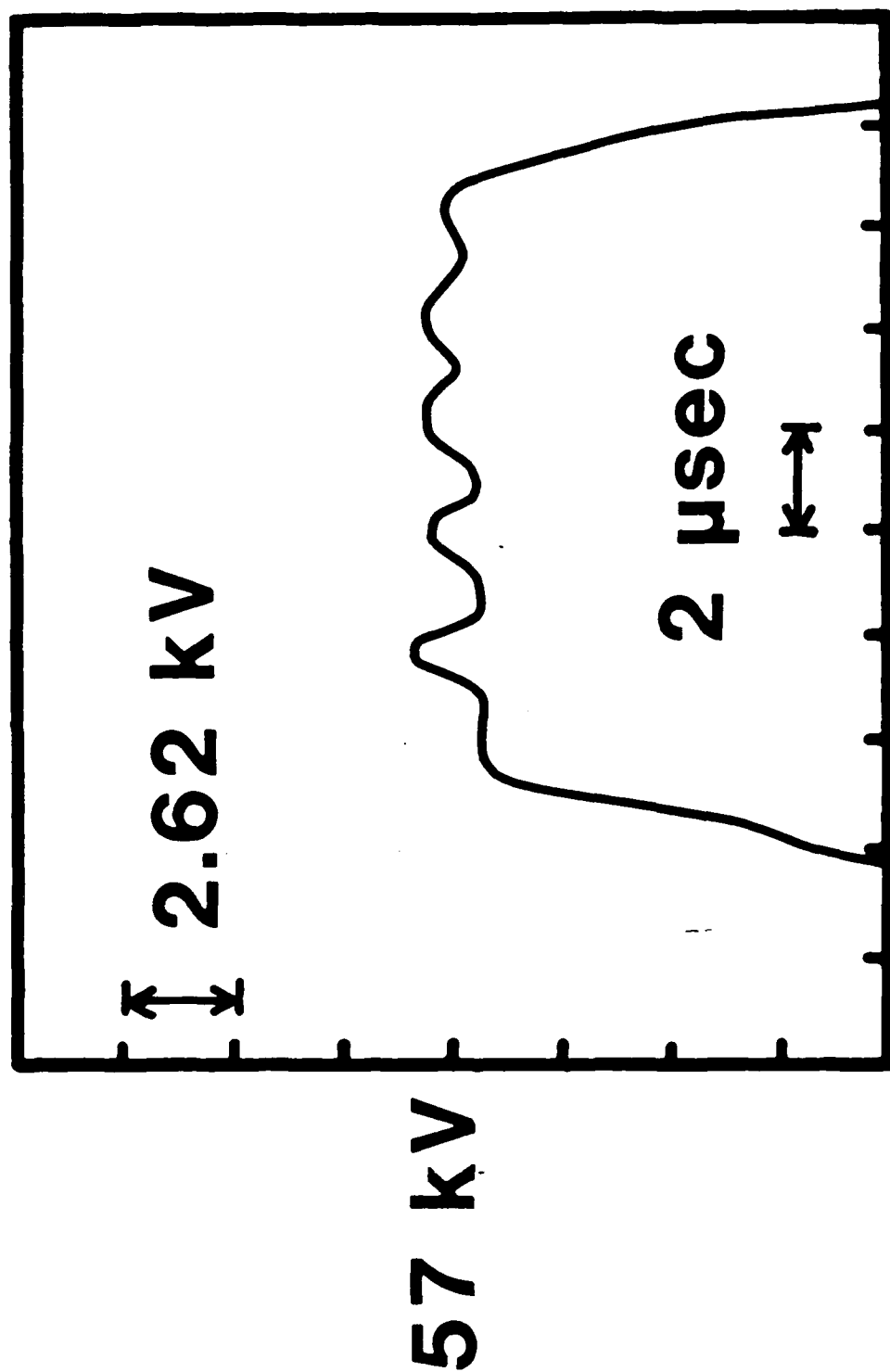


Figure 20 Voltage waveform applied to the cathode (a) and intermediate anode (b) of the electron gun.

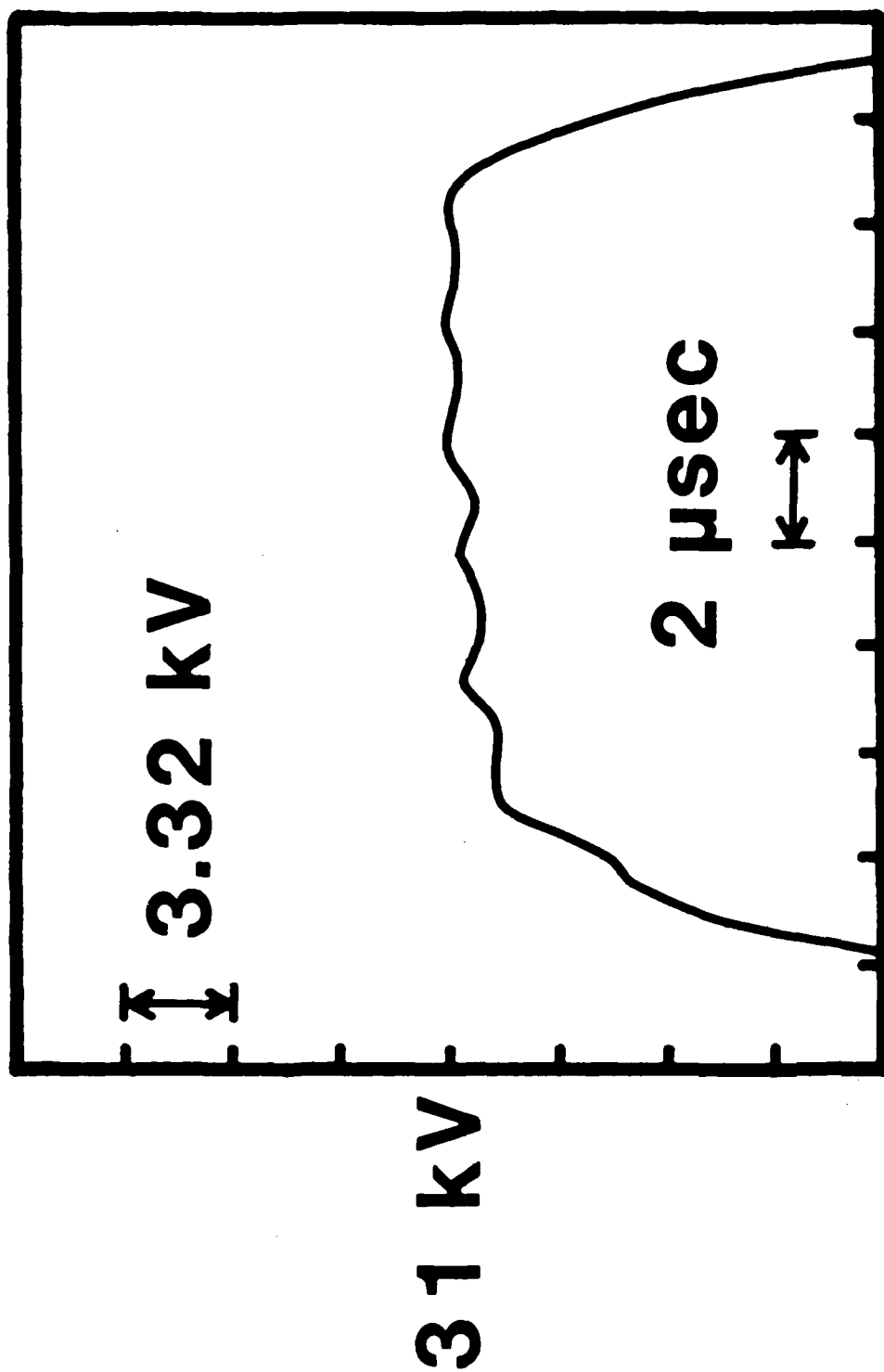


Figure 20 (Continued) Voltage waveform applied to the cathode (a) and intermediate anode (b) of the electron gun.

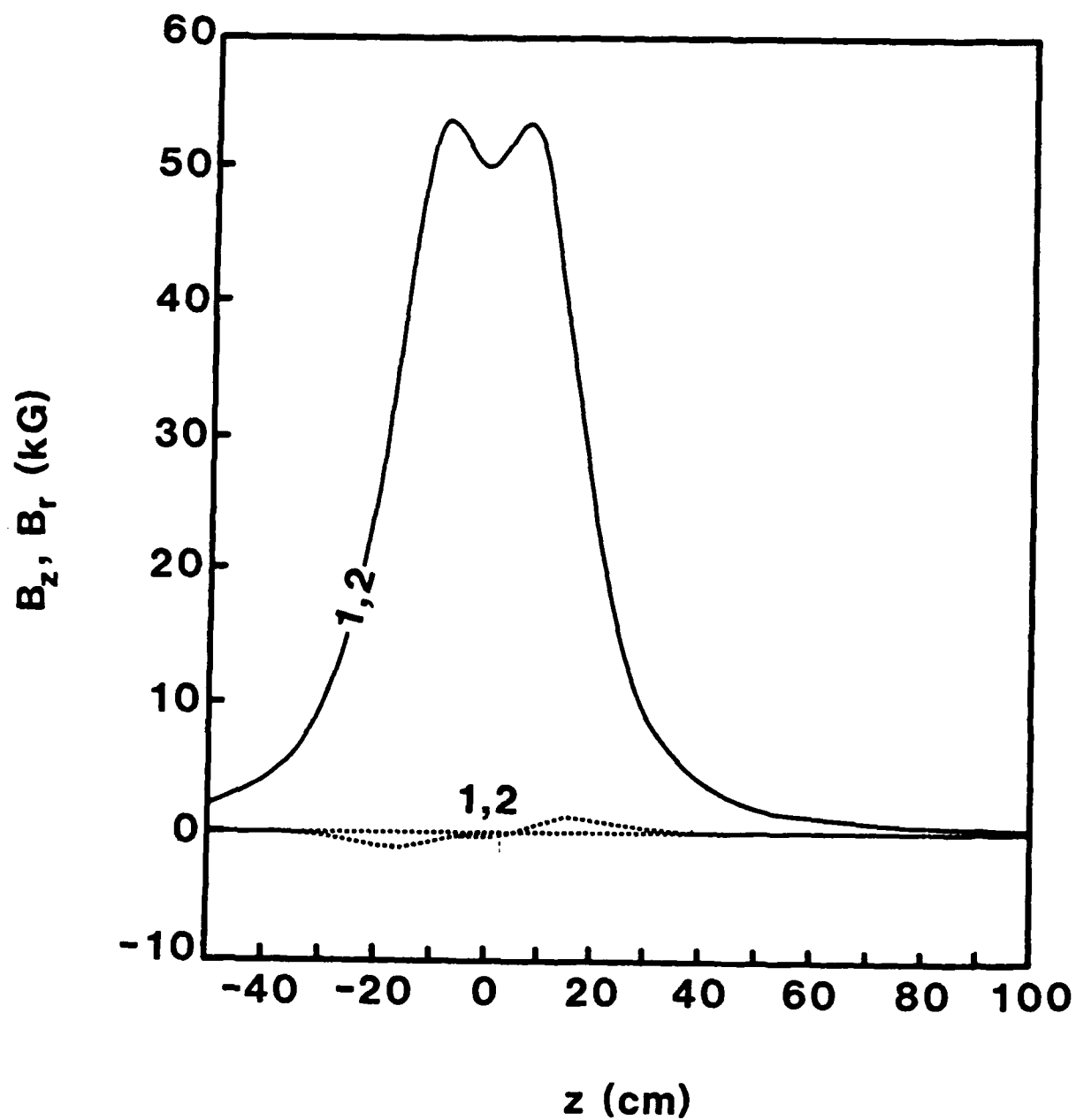


Figure 21 Profile of applied axial (B_z , solid curve) and radial (B_r , dashed curves) magnetic fields measured on axis (curve 1) and 0.7 cm off axis (curve 2).

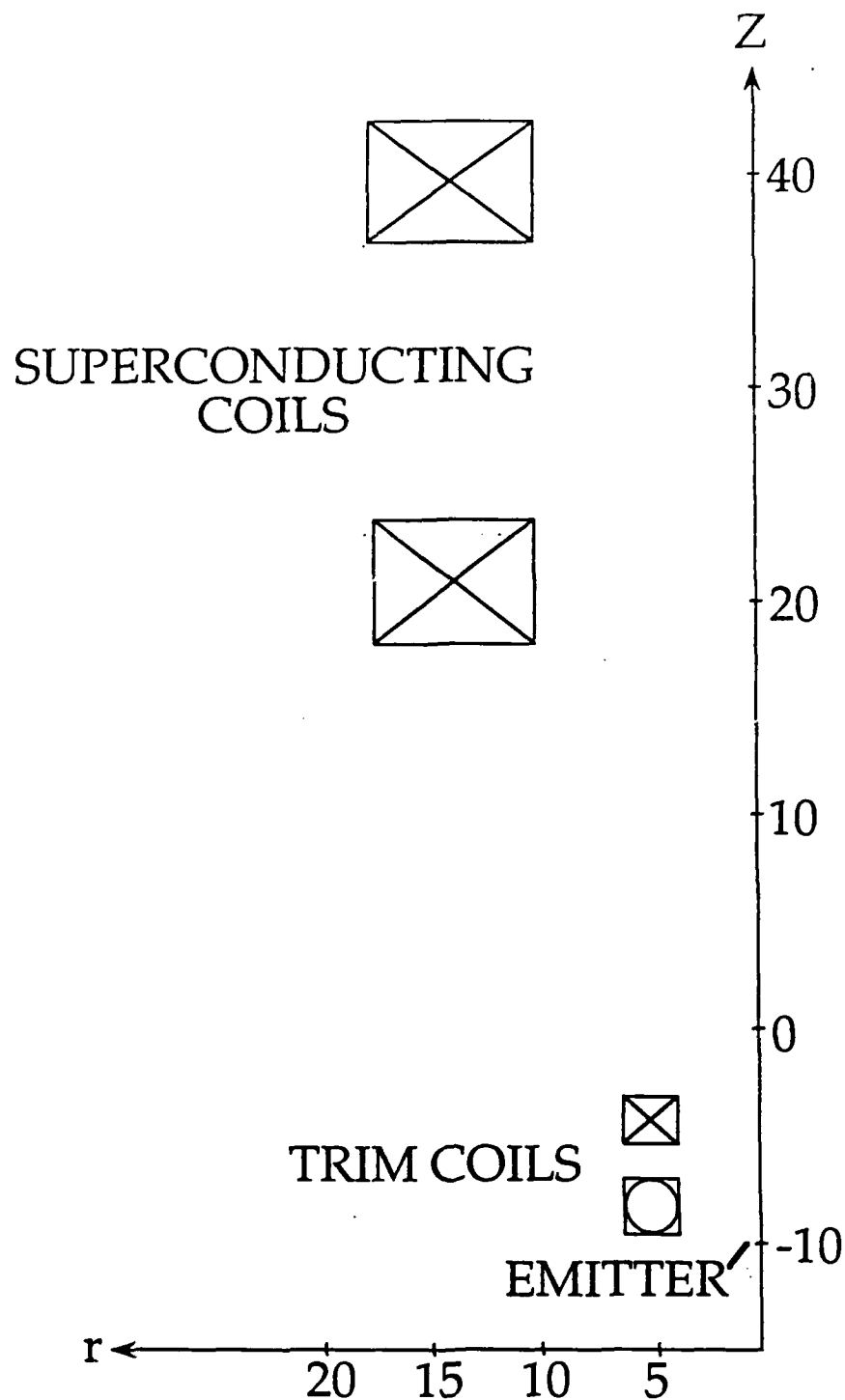


Figure 22 Configuration of the electron gun emitter and the main and trim magnetic field coils. The trim coil nearest the emitter generated a magnetic field in the direction opposite the fields of the other coils and the origin of the z-axis (axis of symmetry) indicates the bottom of the superconducting magnet dewar flange.

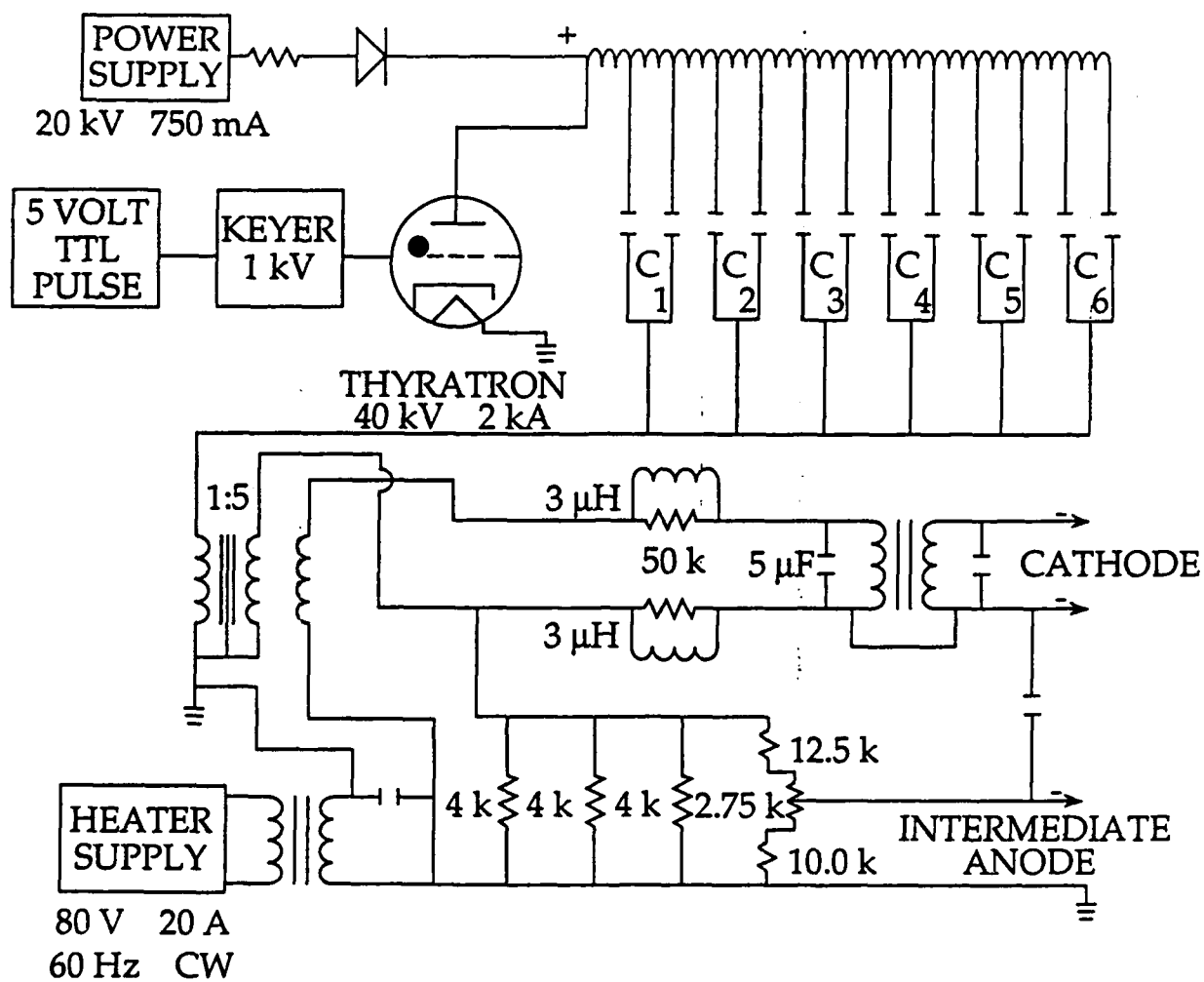


Figure 23 Schematic diagram of the 13 μ sec, high-voltage modulator used in the experiments.

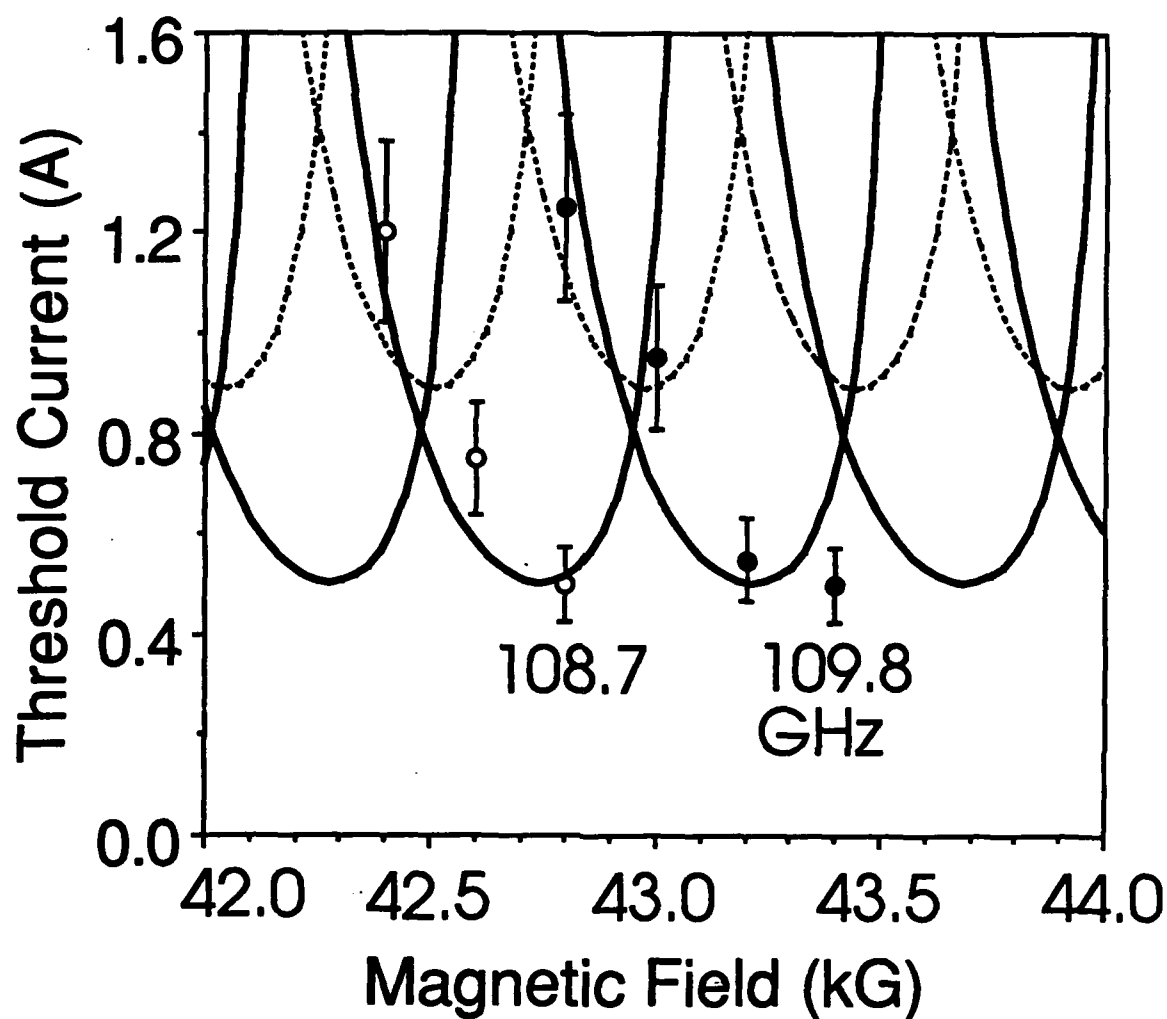


Figure 24 Threshold currents for a 25 cm mirror separation. The solid dots show data with an oscillation frequency of 109.8 ± 0.1 GHz, and the open circles show data with an oscillation frequency of 108.8 ± 0.1 GHz. The solid (dashed) curves show theoretical results based on $\alpha = 1.5$ for longitudinal modes with an electric field maximum (minimum) coinciding with the electron beam axis.

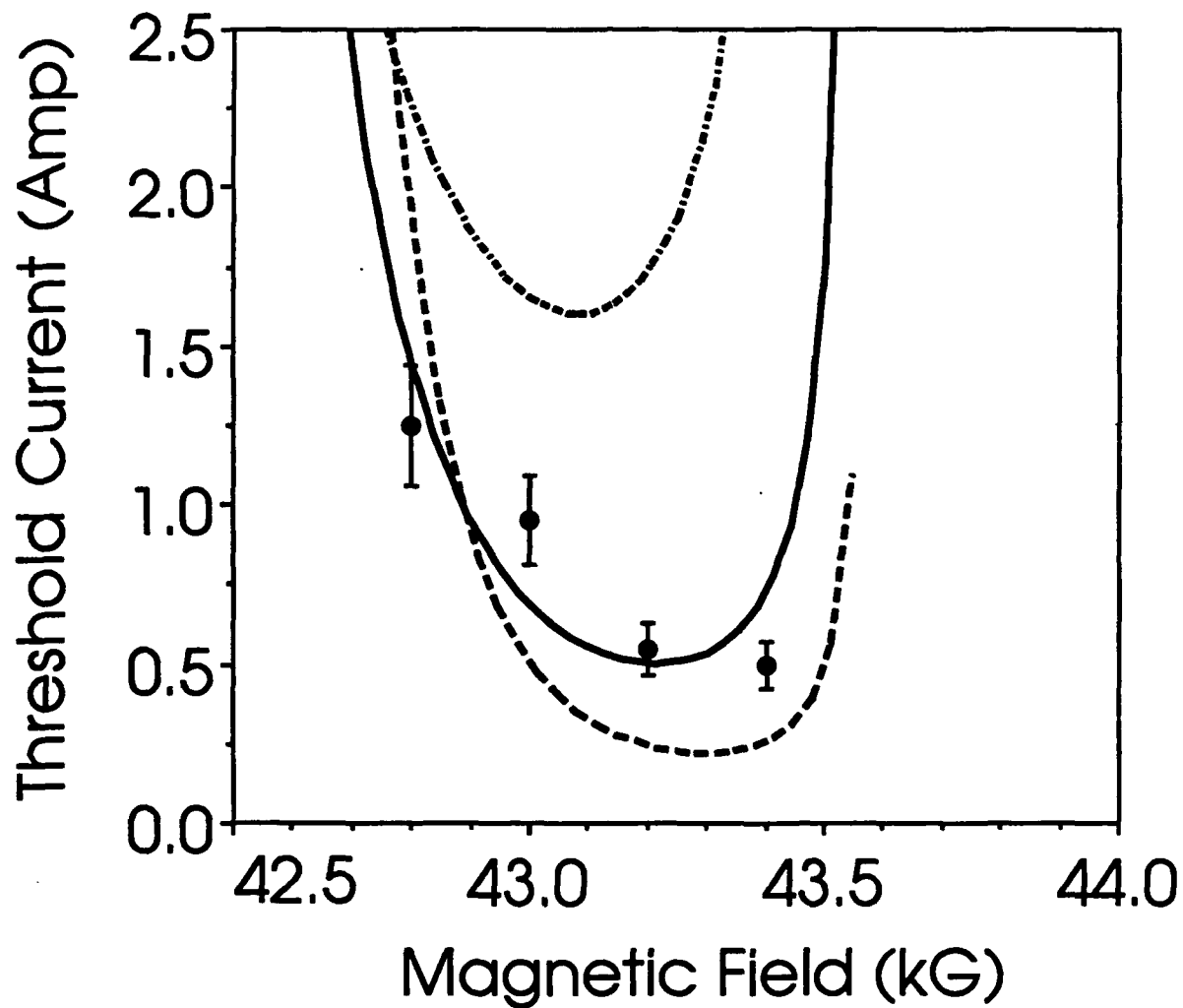


Figure 25 Threshold current dependence on α for a mirror separation of 25 cm. The solid curve shows the theoretical result for $\alpha = 1.5$, the dashed curve corresponds to $\alpha = 1$, and the dash-dot-dash curve corresponds to $\alpha = 2$. Other parameters are as given for Figure 24.

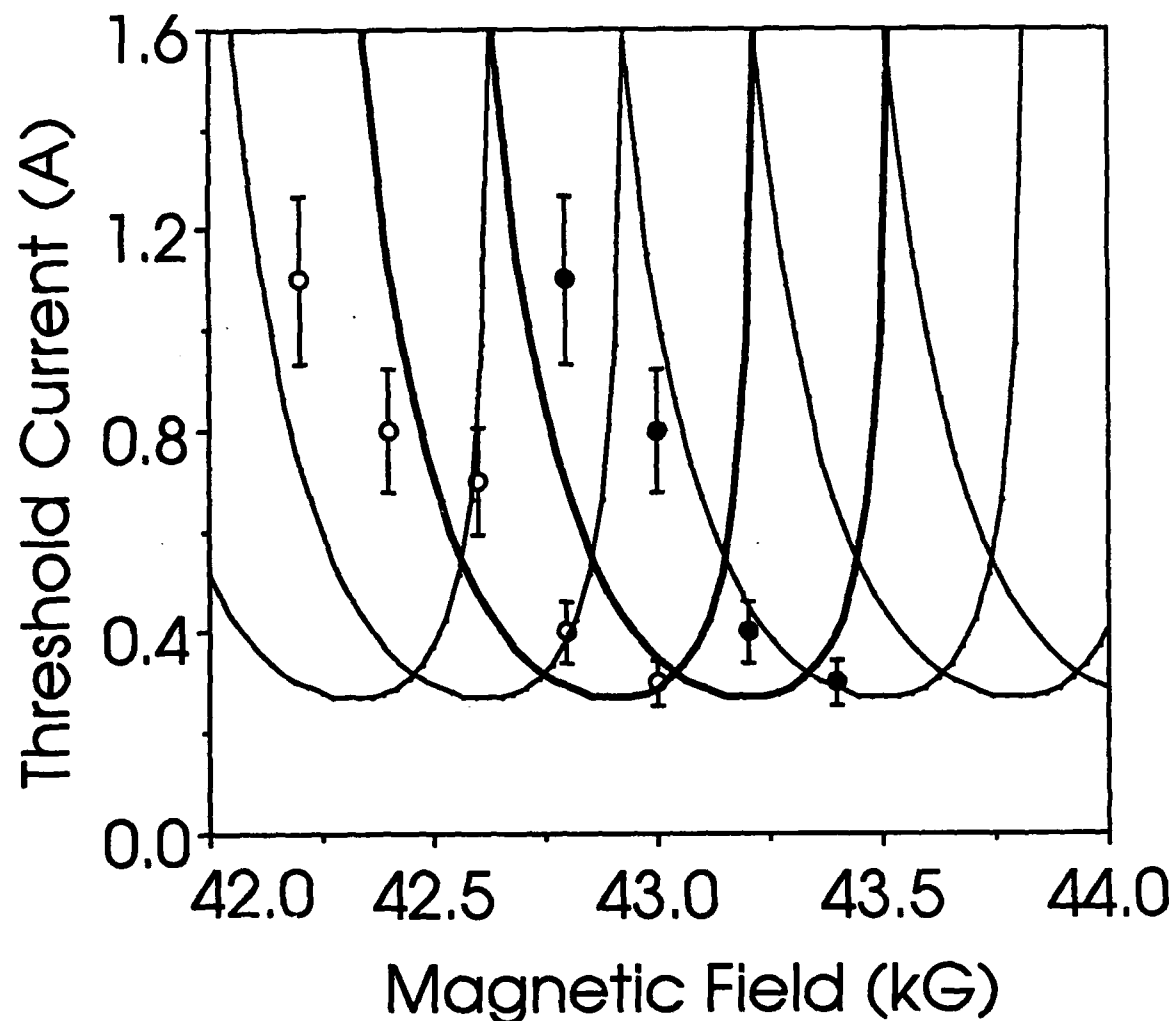


Figure 26 Threshold currents for a 20 cm mirror separation. The solid dots show data with an oscillation frequency of 109.8 ± 0.1 GHz, and the open circles show data with an oscillation frequency of 109.2 ± 0.2 GHz. The solid curves show theoretical results based on $\alpha = 1.5$ and the electron beam axis located midway between the electric field maxima for adjacent longitudinal modes of the resonator. The two thicker line theoretical curves correspond to frequencies of 109.05 (minimum oscillation current at ~ 42.8 kG) and 109.8 GHz (minimum oscillation current at ~ 43.2 kG).

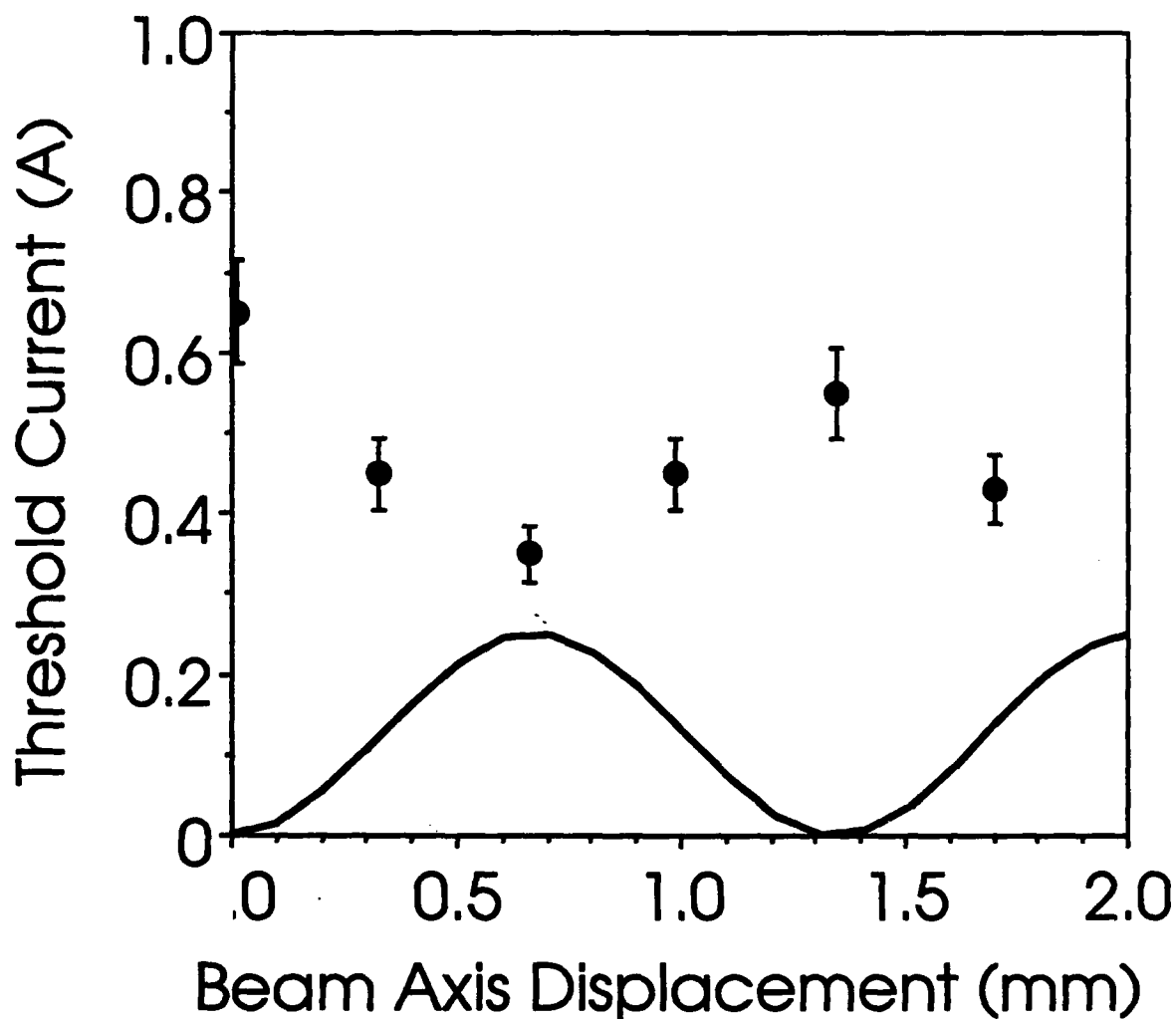


Figure 27 Threshold current dependence on beam translation. The solid dots show data for a 20 cm mirror separation, a gun voltage of 54.2 kV, a magnetic field of 43 kG, and an oscillation frequency of 111 ± 0.1 GHz. The solid curve is proportional to the amplitude squared of the standing-wave RF field of the resonator.

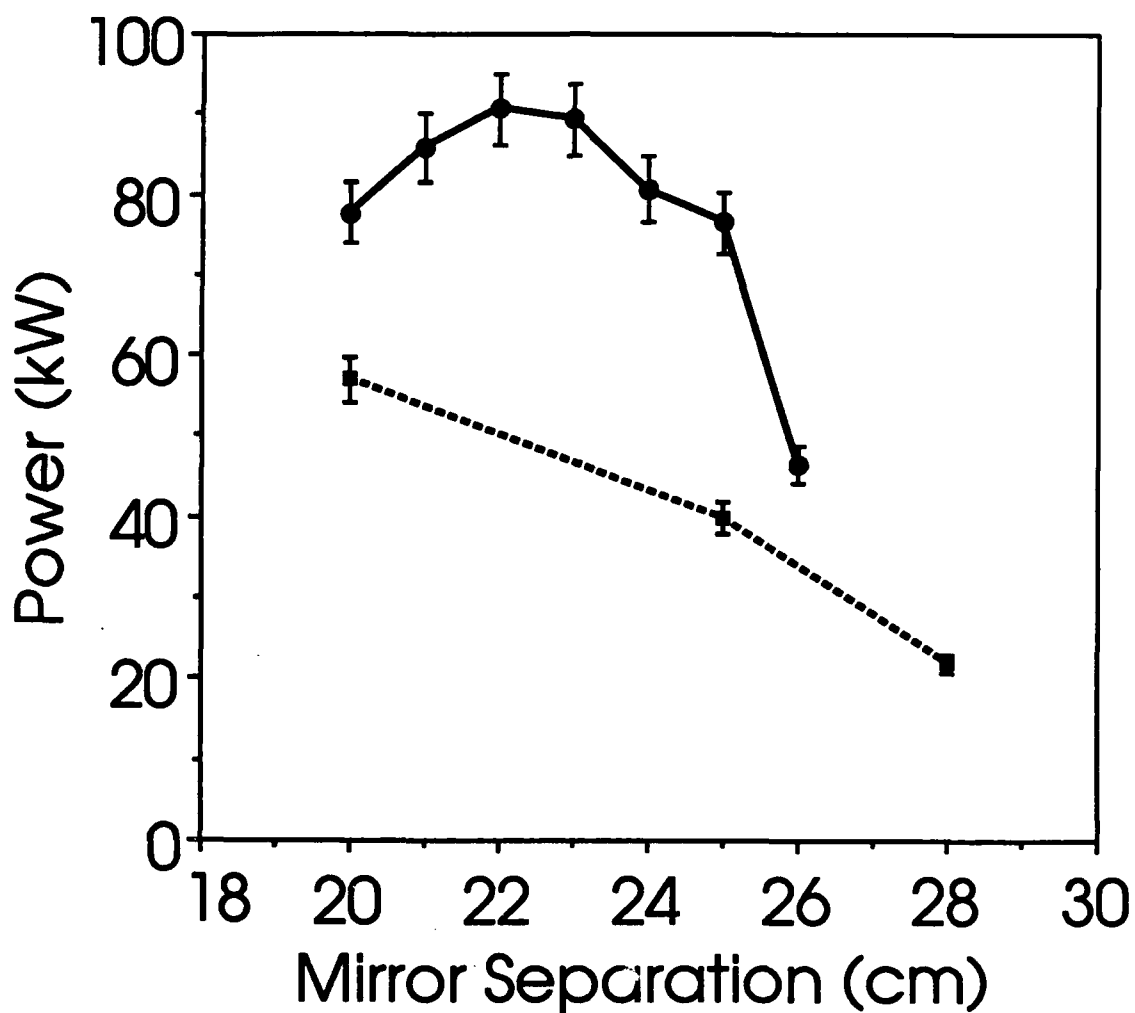


Figure 28 Output power vs. mirror separation for a 50 kG magnetic field. The solid square data corresponds to a gun voltage of $V = 66.7$ kV and a beam current of 8 A. The solid dot data corresponds to a gun voltage of $V = 71.5$ kV and a beam current of 13.5 A.

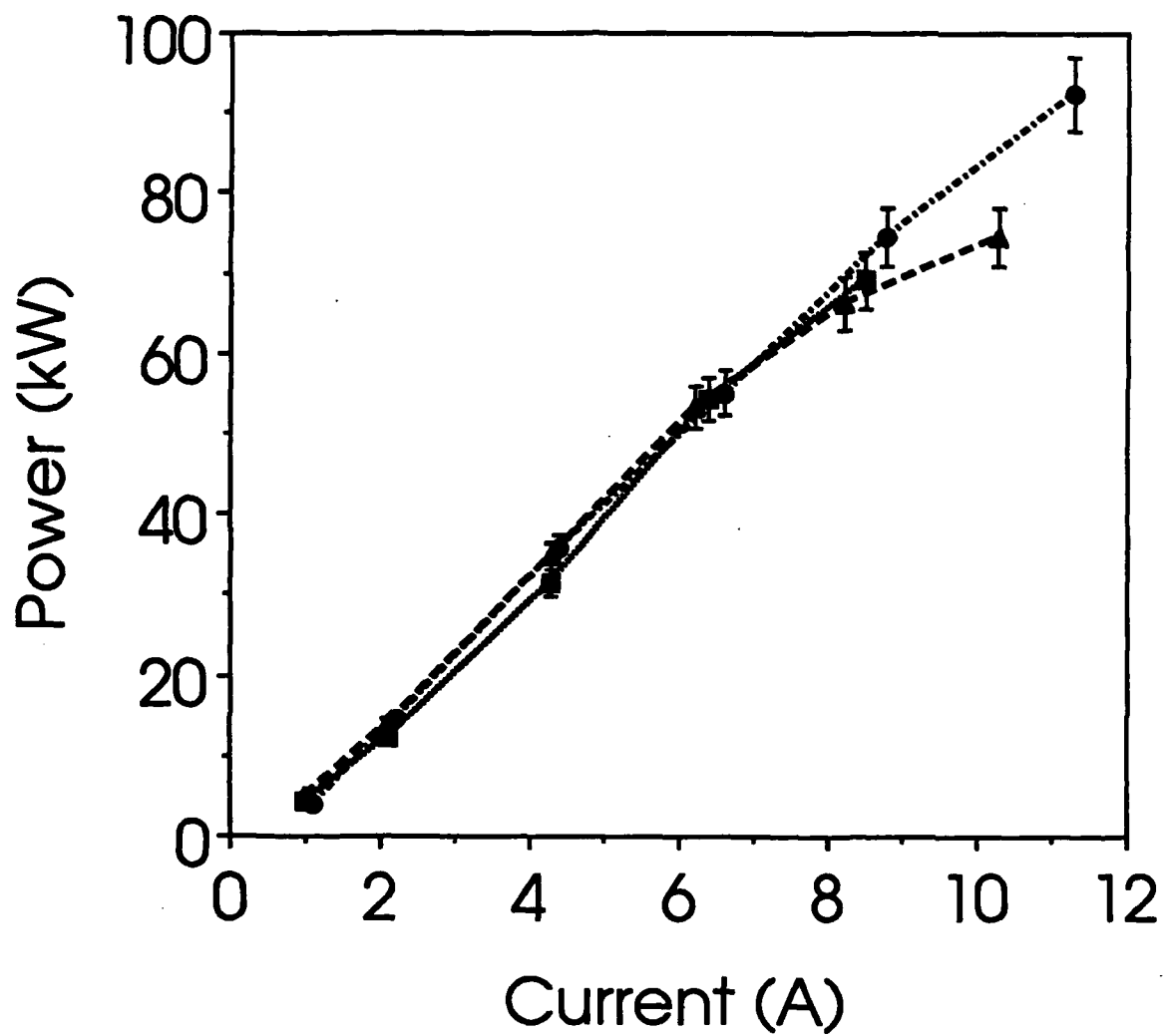


Figure 29 Output power vs. beam current for 20 cm mirror separation and a gun voltage of 71.5 kV. The magnetic field is 44, 47, and 50 kG for the solid square, solid dot, and solid triangle data, respectively.

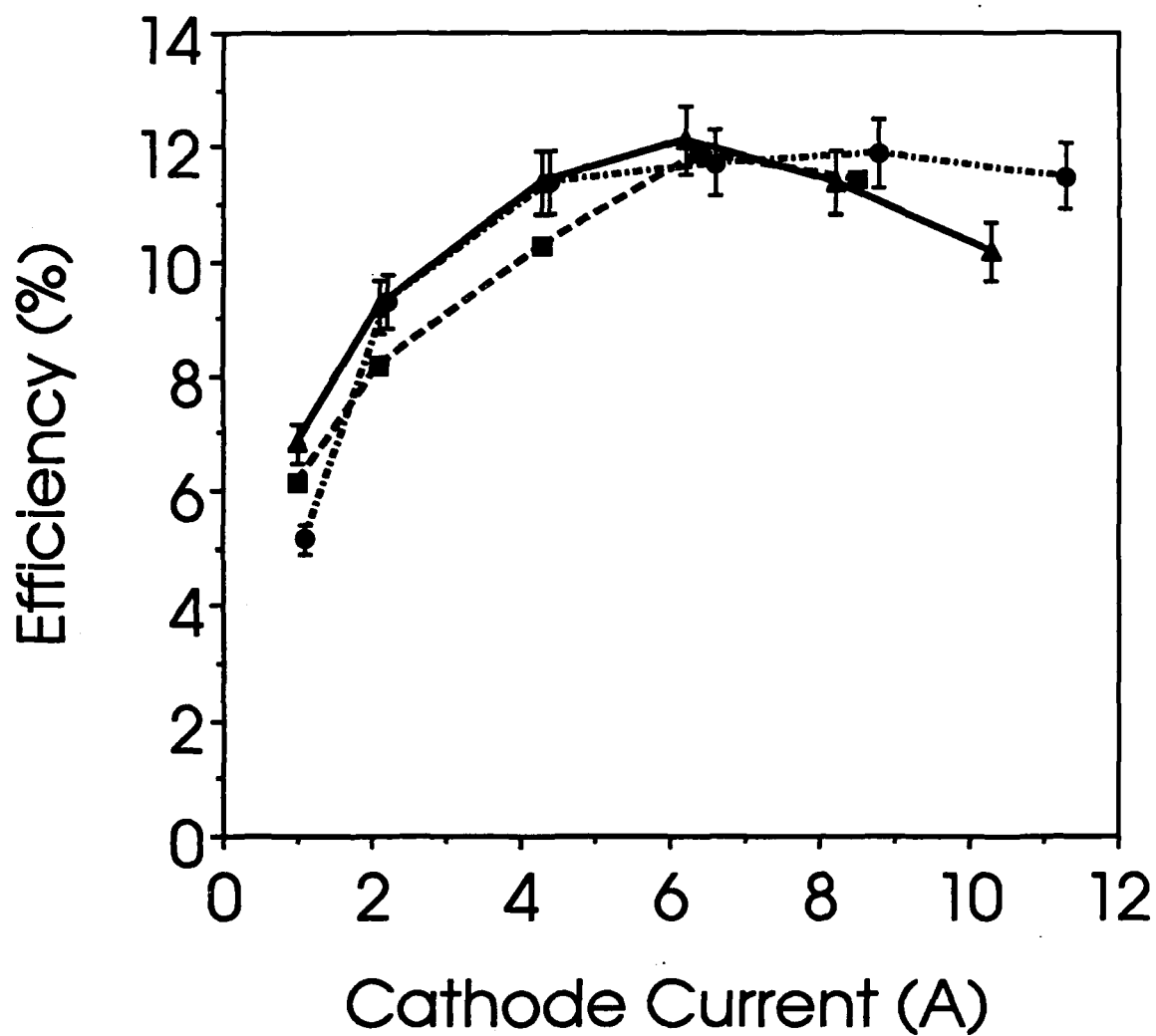


Figure 30 Output efficiency vs. beam current for 20 cm mirror separation and a gun voltage of 71.5 kV. The magnetic field is 44, 47, and 50 kG for the solid square, solid dot, and solid triangle data, respectively.

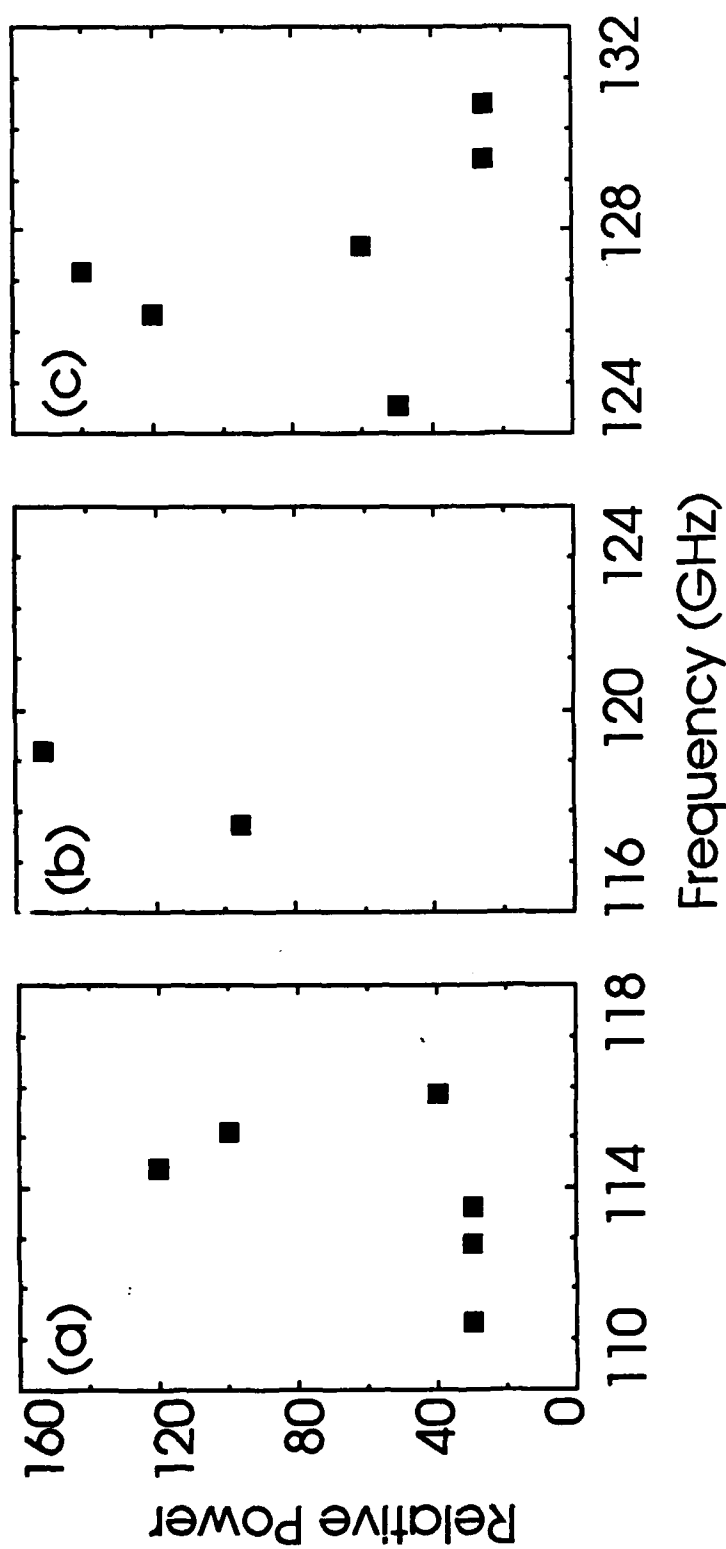


Figure 31 Typical multimode frequency spectra for a mirror separation of 20 cm and a gun voltage of 71.5 cm. (a): $B = 44$ kG, $I = 8$ A; (b): $B = 47$ kG, $I = 14$ A; (c): $B = 50$ kG, $I = 8$ A.

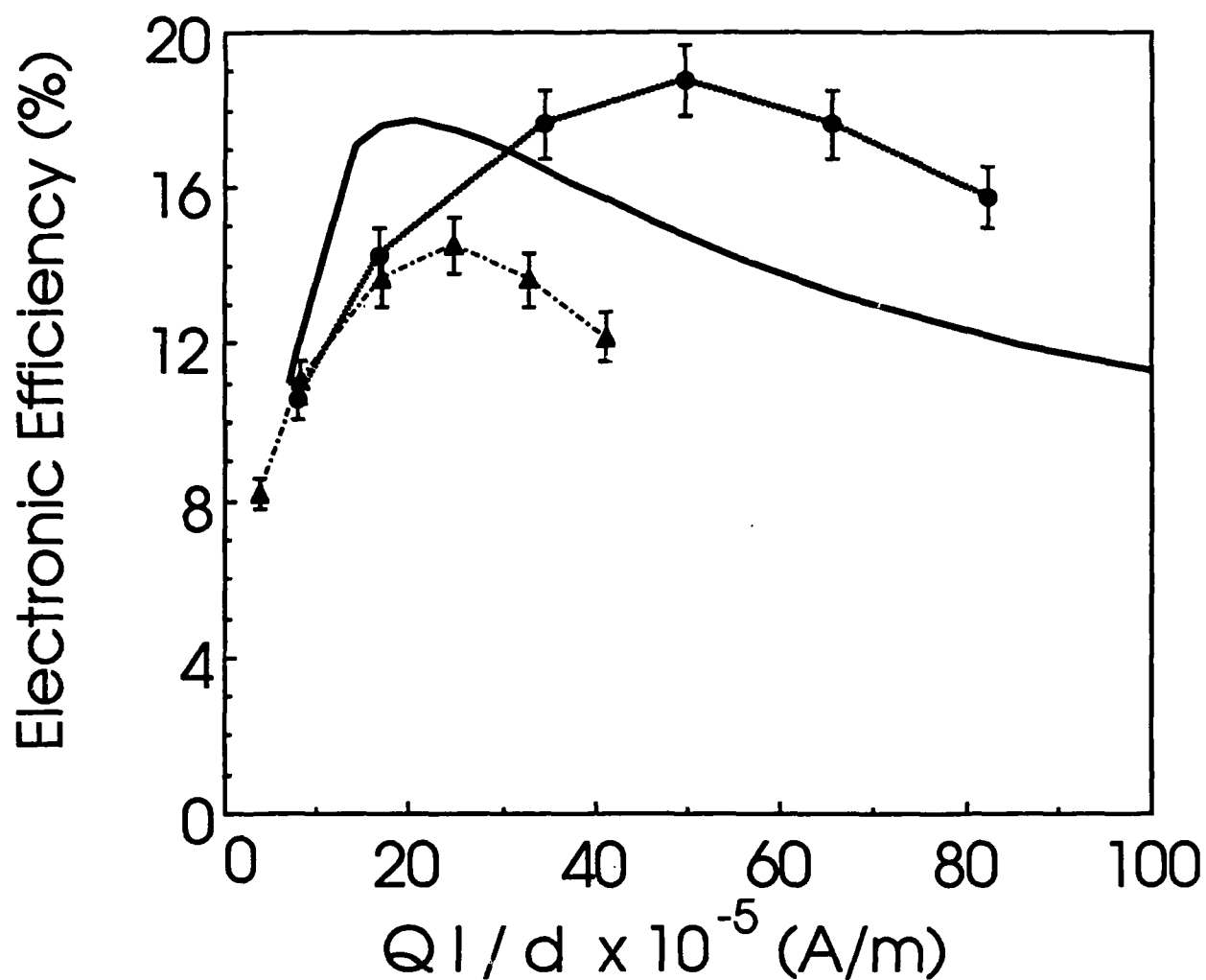


Figure 32 Electronic efficiency vs. QI/d . The solid curve shows results from a multimode, annular beam simulation. The solid dots and triangles show the estimated electronic efficiency for the 50 kG power data shown in Figure 29. The solid dots are based on the diffraction Q obtained from scalar diffraction theory, and the solid triangles are based on the Q inferred from the threshold current data.

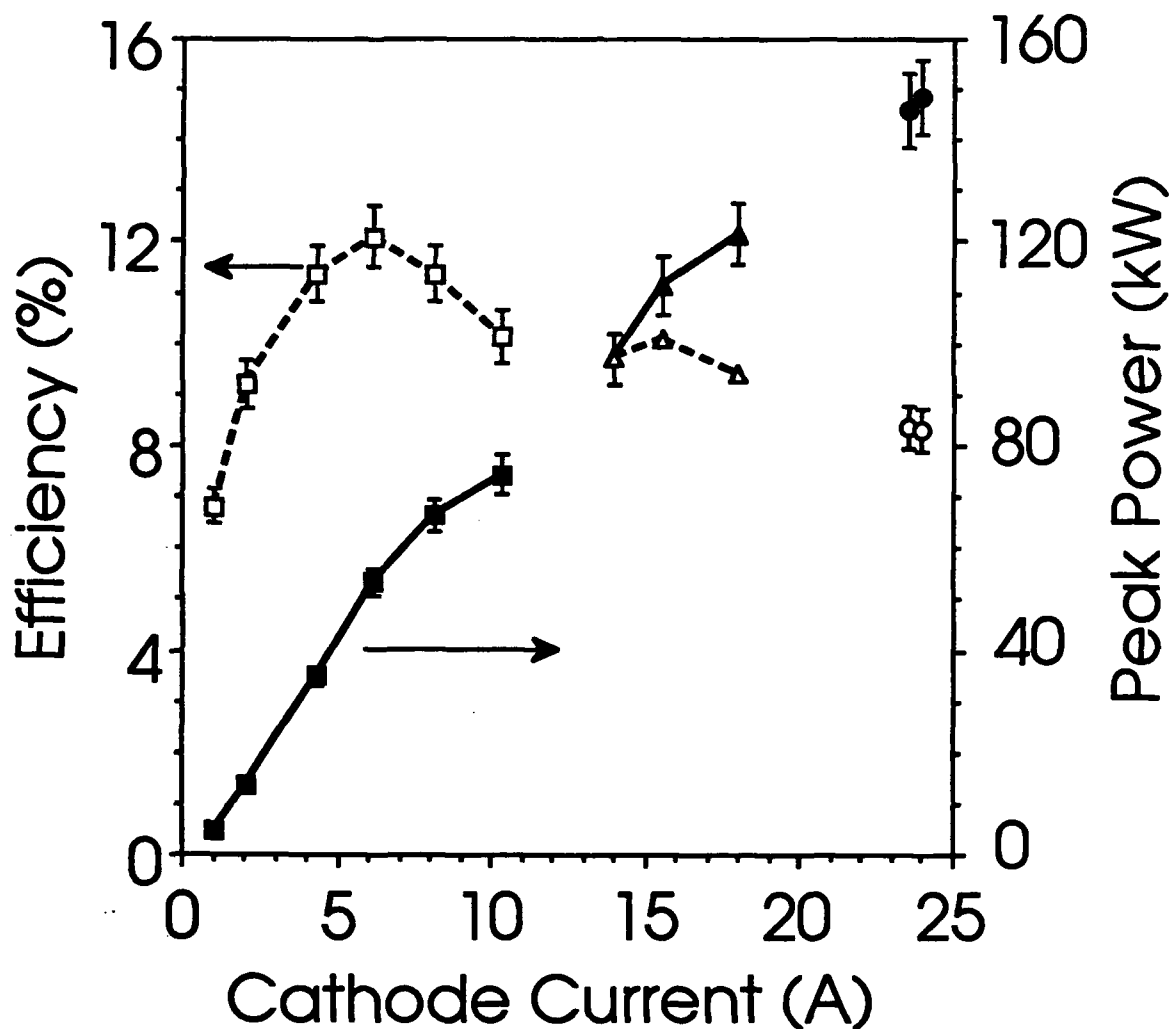


Figure 33 Output power and efficiency operation with a 50 kG resonator magnetic field and gun voltages of 71–74 kV. The mirror separation for the data shown by the solid and open squares is 20 cm, and is 23 cm for the data shown by the solid and open circles and triangles. The resonator magnetic field has a 2% negative taper for the data shown by the solid and open circles.

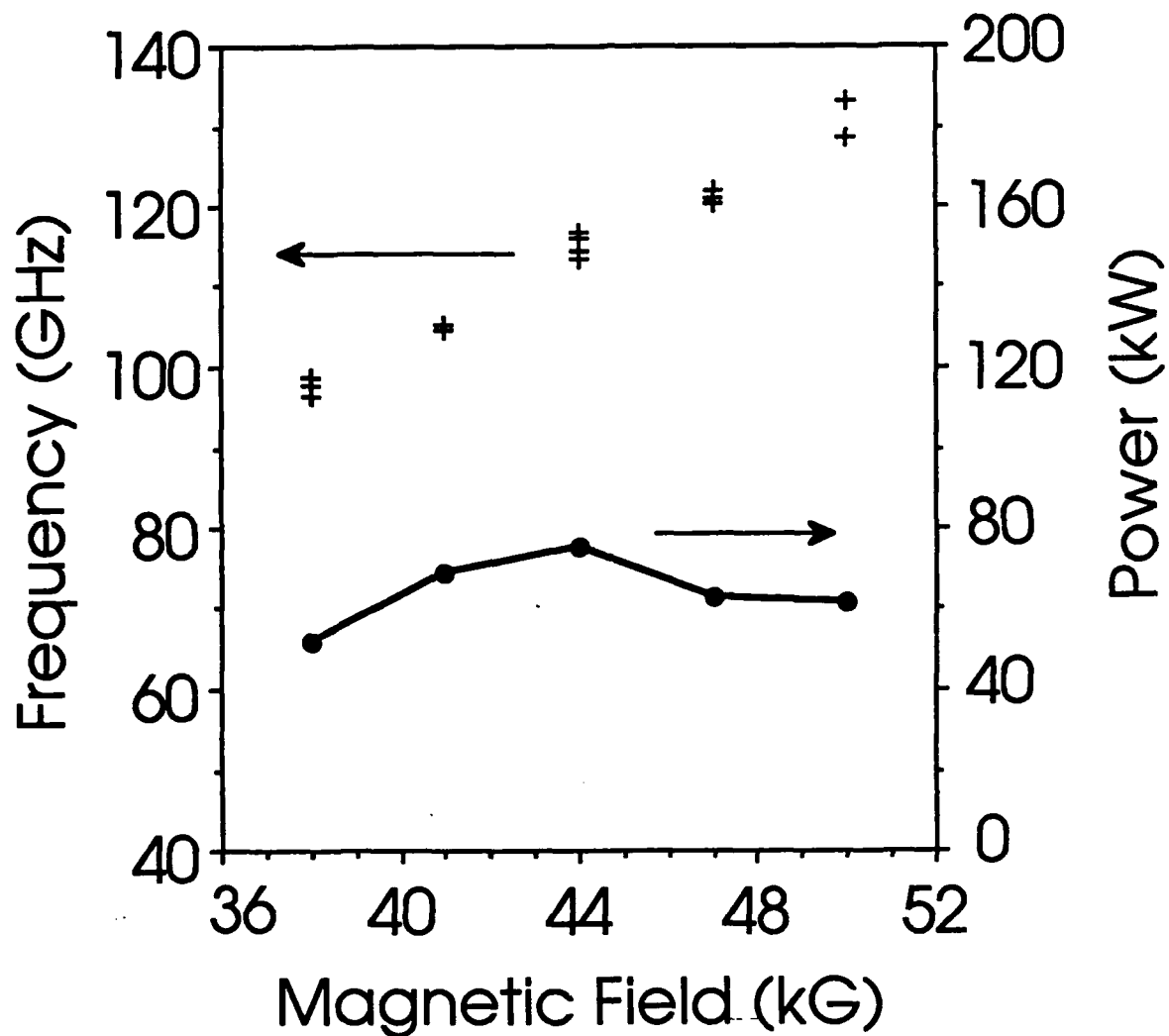


Figure 34 Frequency tuning by magnetic field variation. The oscillation frequencies are shown by +’s and the output power is shown by the solid dots. The gun voltage and beam current 66.7 kV and 12 A, respectively.

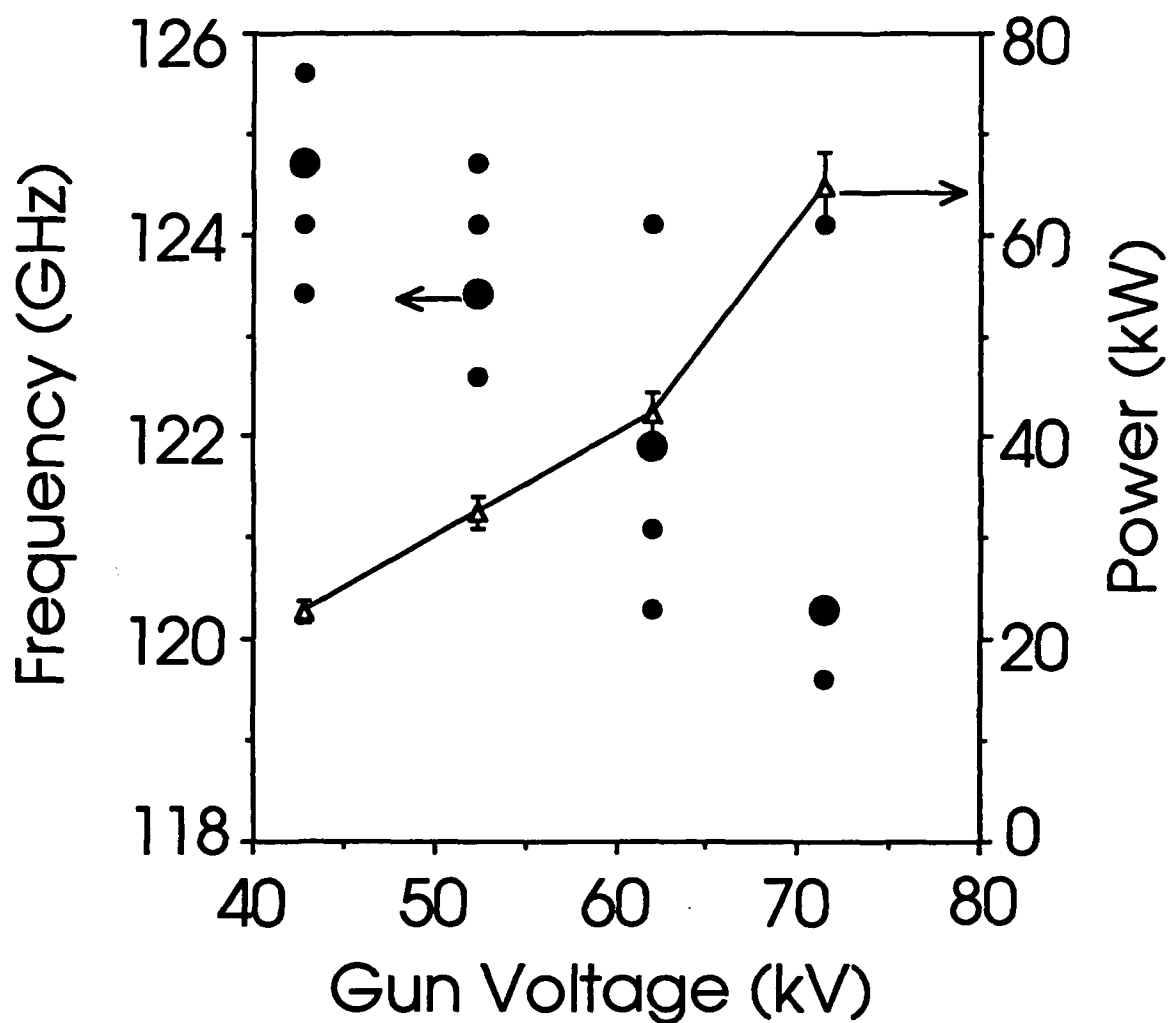


Figure 35 Frequency tuning with gun voltage variation for a magnetic field of 50 kG, a current of ~ 10 A and a 20 cm mirror separation. The oscillation frequencies are shown by the solid dots and the large dots indicate the dominant mode.

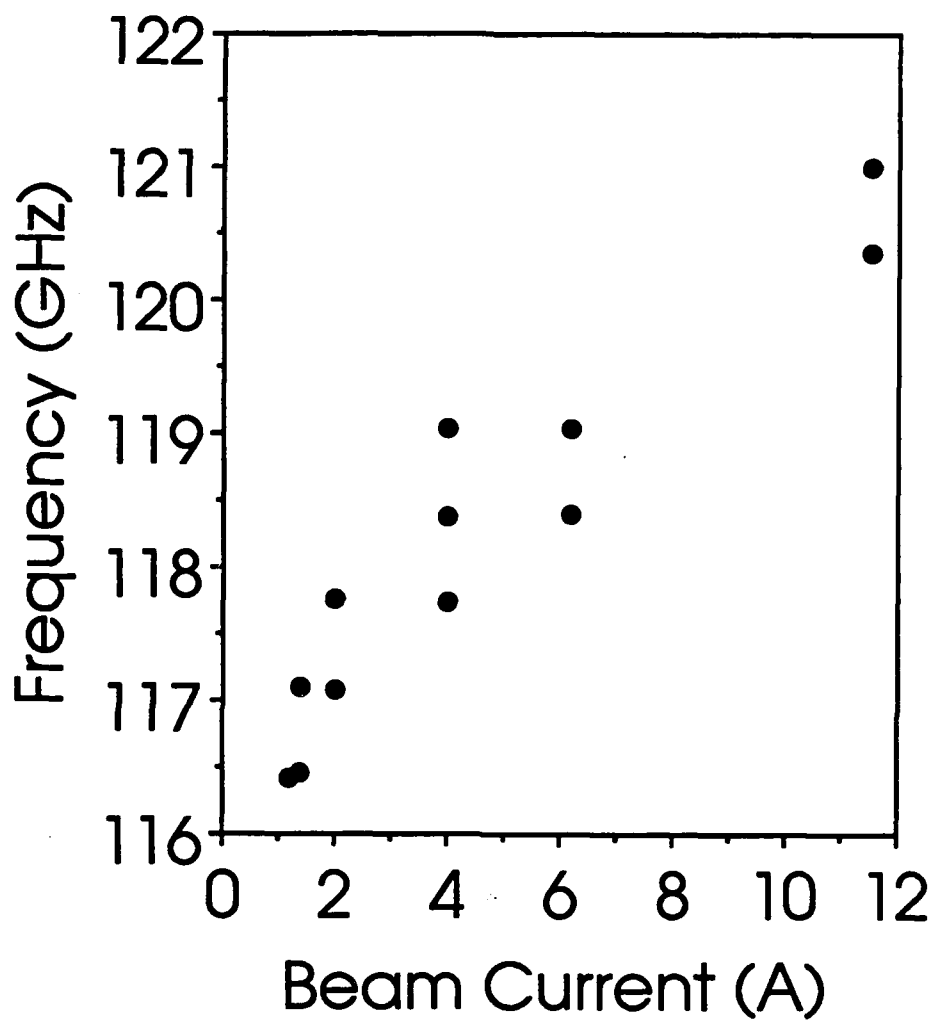


Figure 36 Mode frequencies as a function of current for a magnetic field of 47 kG with a 2% negative taper, a fixed voltage of 71.5 kV, and a 23 cm mirror separation.

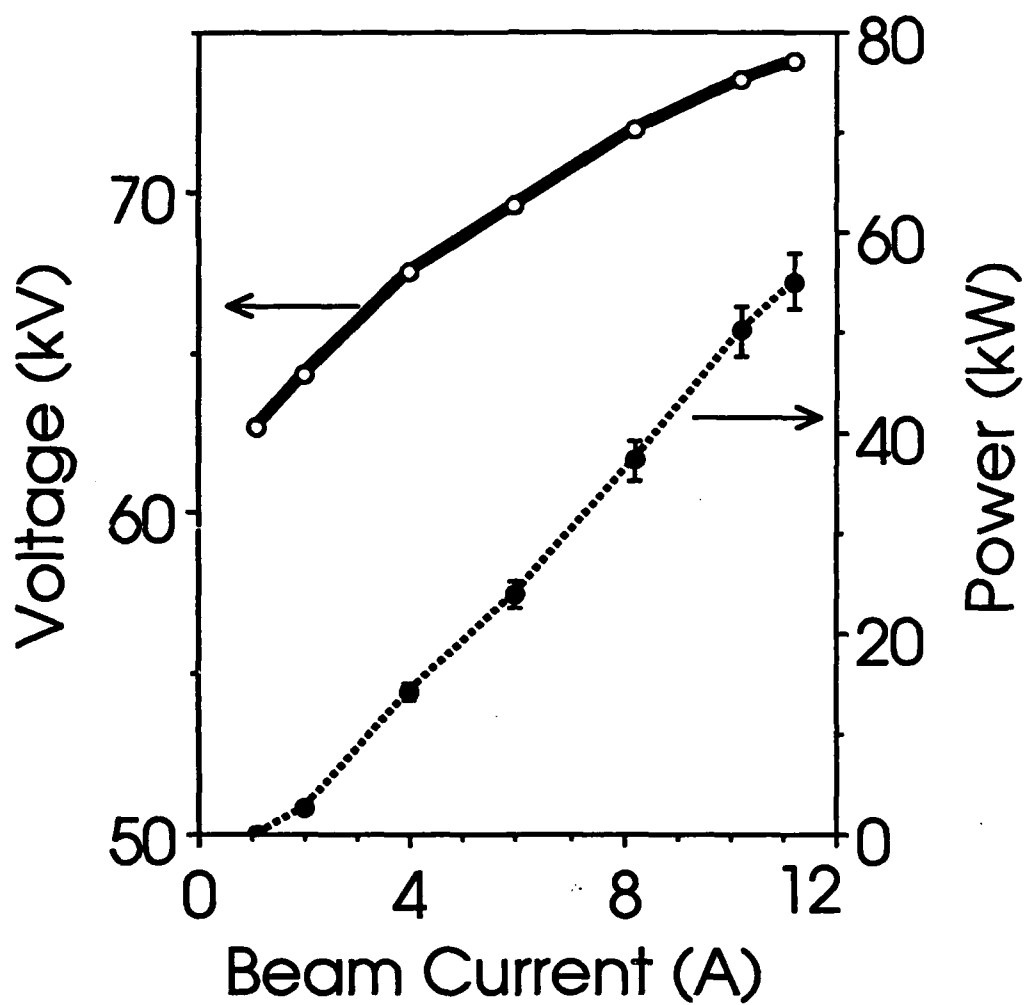


Figure 37 A region of single-mode operation in $V - I$ space. The magnetic field is 47 kG and the frequency is 119 GHz.

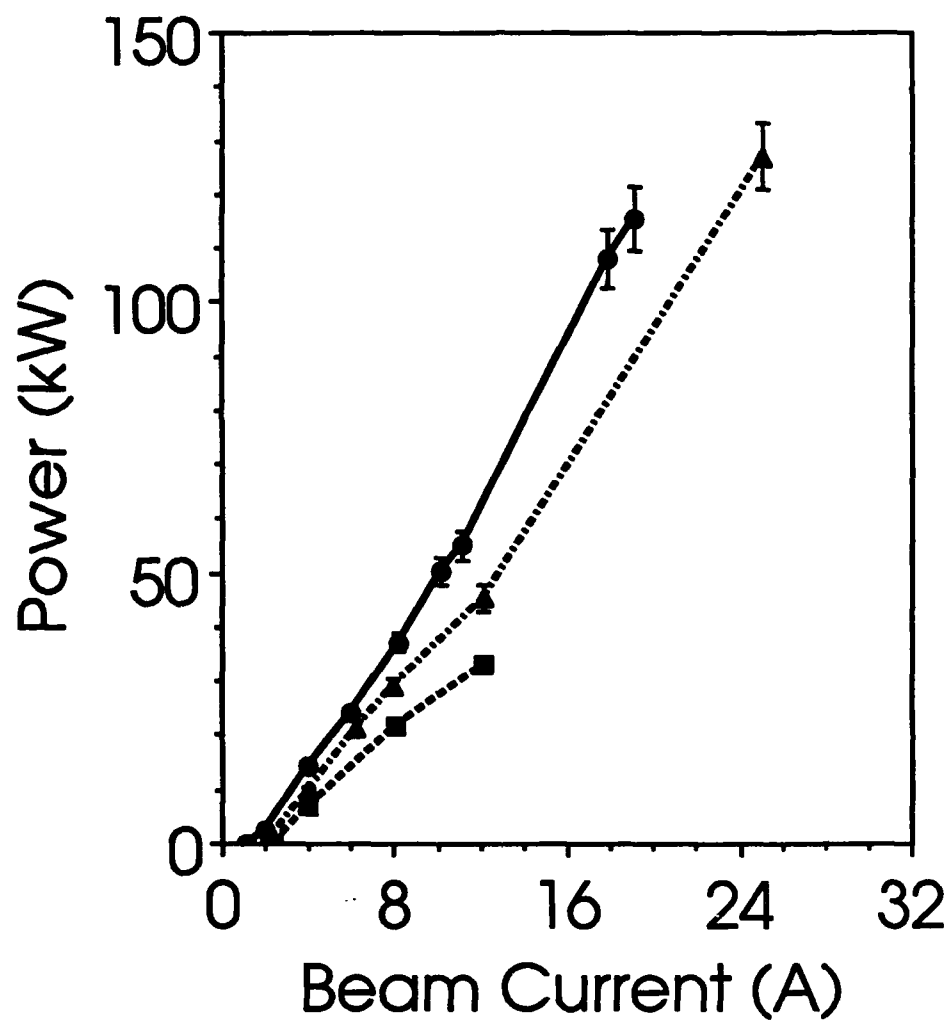


Figure 38 Output power for single-moded or near single-moded operation for a magnetic field of 47 kG and frequencies of 119–120 GHz. The mirror separation is 23, 25.5, and 28 cm for the solid dots, triangles, and squares, respectively.

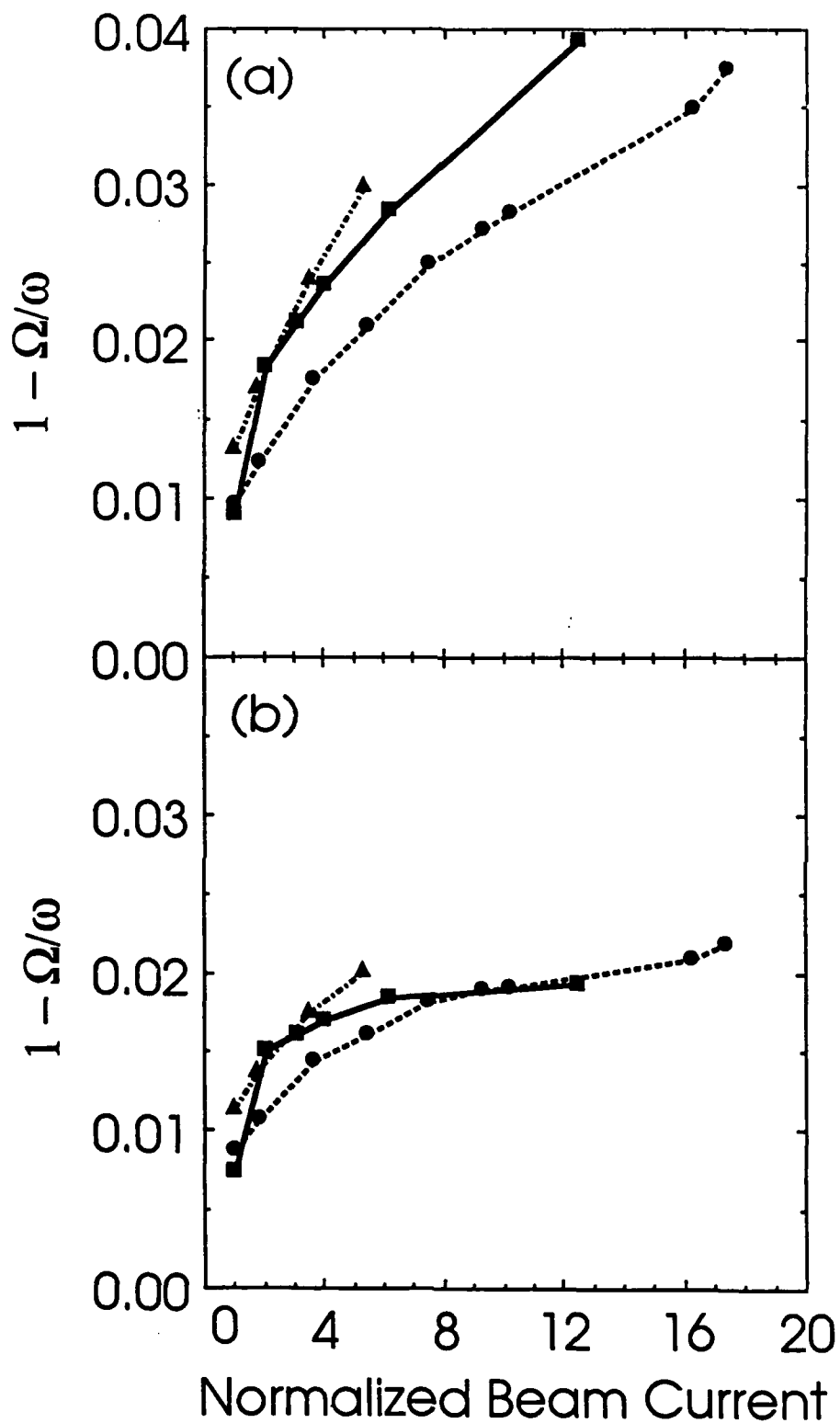


Figure 39 Resonance detuning dependence on beam current normalized to the threshold current. The detuning in (a) is uncorrected for space-charge effects, the data in (b) includes a space-charge correction. The solid dots, triangles, and squares correspond to the data shown in Figure 38.

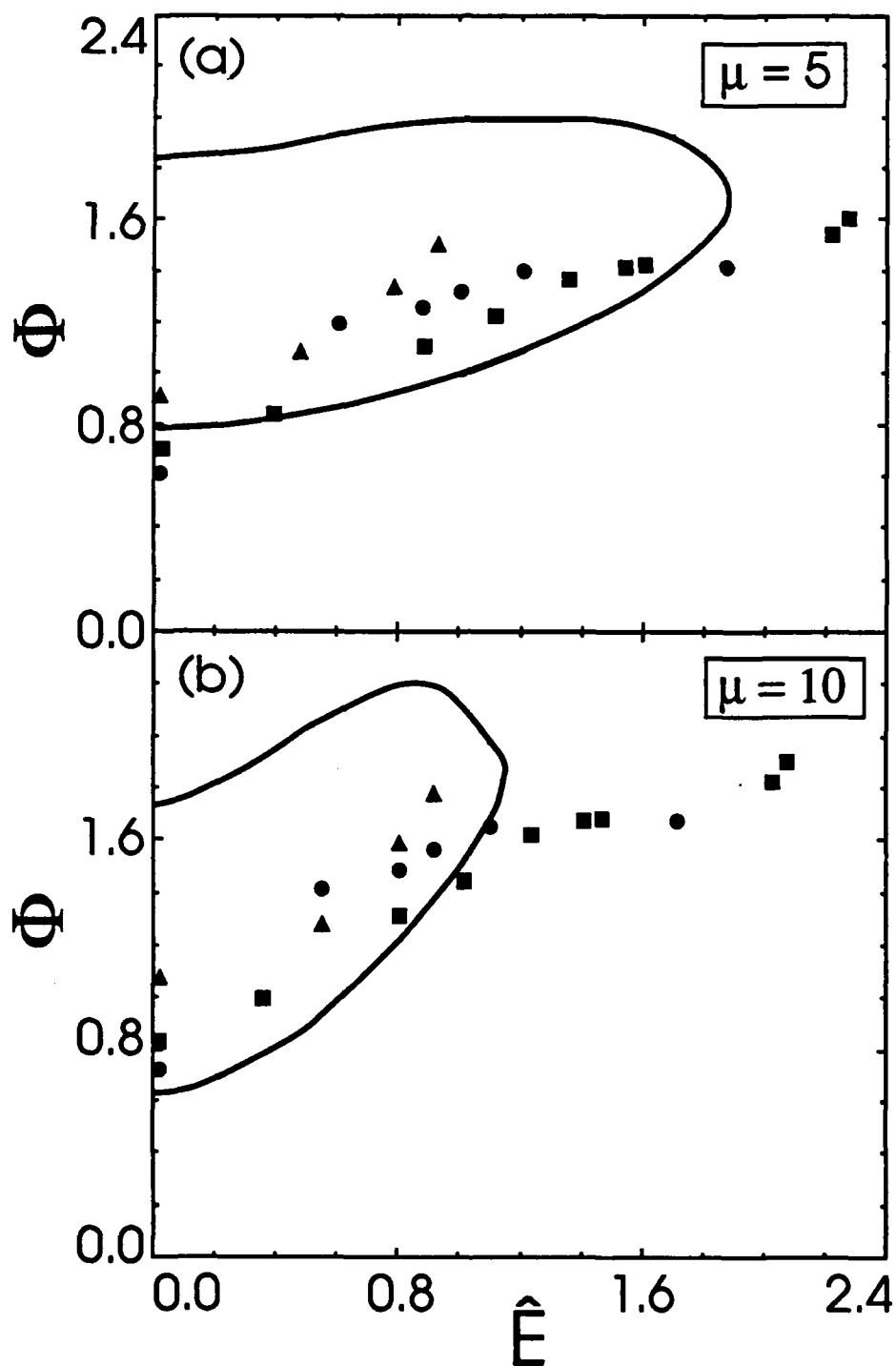


Figure 40 QOG normalized operating parameter space for (a): $\mu = 5$ ($\alpha = 0.65$) and (b): $\mu = 10$ ($\alpha = 1$). The solid dots, triangles, and squares correspond to the data shown in Figure 38. The solid curves indicate the boundary of the predicted region of stable operation.

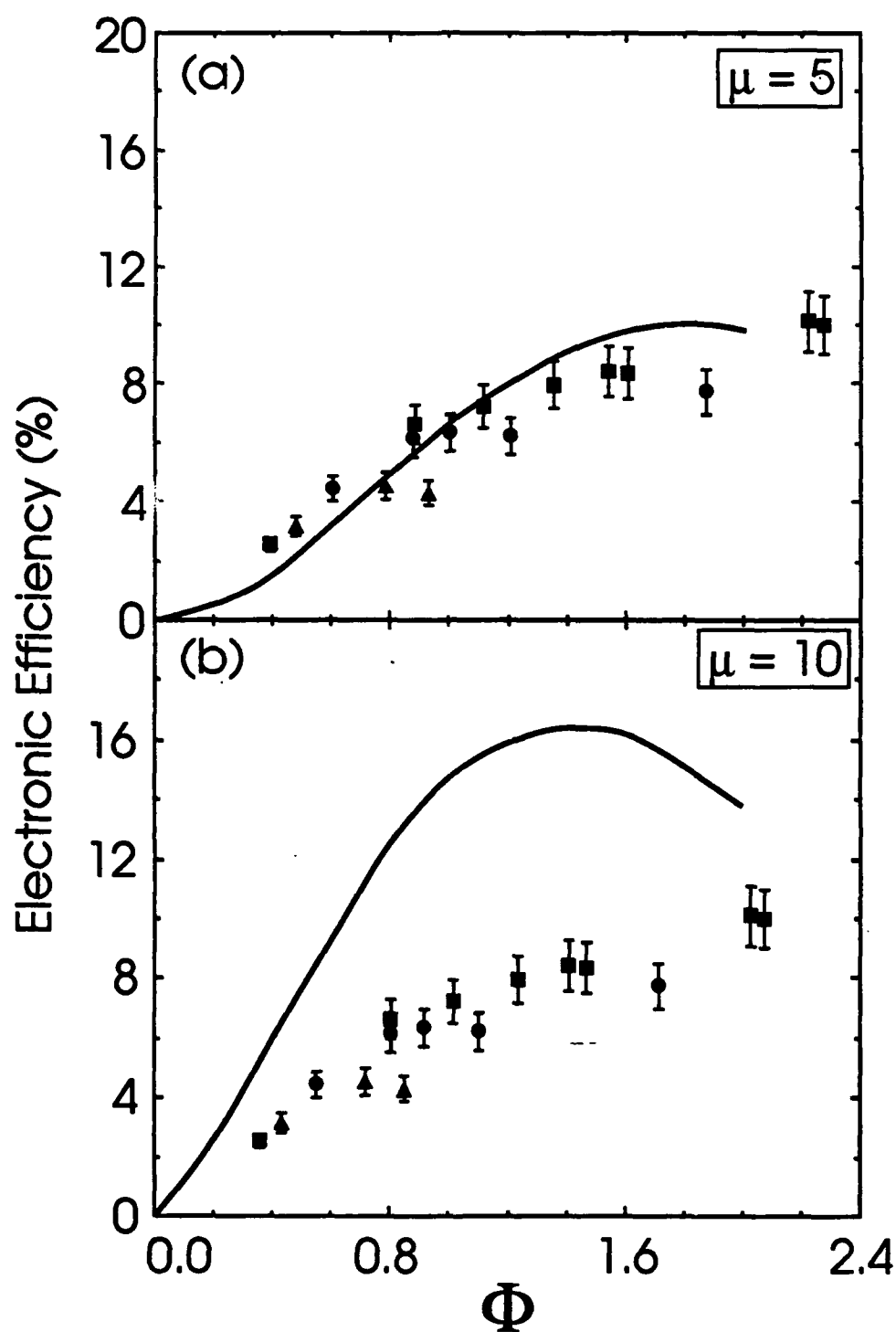


Figure 41 Comparison of theoretical and experimental electronic efficiencies for (a) $\mu = 5$ ($\alpha = 0.65$) and (b) $\mu = 10$ ($\alpha = 0.65$). The solid dots, triangles, and squares correspond to the data shown in Figure 38.

4740 DISTRIBUTION LIST

Air Force Avionics Laboratory AFWAL/AADM-1 Wright/Patterson AFB, Ohio 45433 Attn: Walter Friez	1 copy
Air Force Office of Scientific Research Bolling AFB Washington, D.C. 20332 Attn: H. Schlossberg	1 copy
Air Force Weapons Lab Kirkland AFB Albuquerque, New Mexico 87117 Attn: Dr. William Baker Dr. A.H. Guenter	2 copies 1 copy
Columbia University 520 West 120th Street Department of Electrical Engineering New York, N.Y. 10027 Attn: Dr. S.P. Schlesinger A. Sen	1 copy 1 copy
Columbia University 520 West 120th Street Department of Applied Physics and Nuclear Engineering New York, New York 10027 Attn: T.C. Marshall R. Gross	1 copy 1 copy
Cornell University School of Applied and Engineering Physics Ithica, New York 14853 Attn: Prof. Hans H. Fleischmann John Nation R. N. Sudan	1 copy 1 copy 1 copy
Creol-FEL Research Pavillion 12424 Research Parkway, Suite 400 Orlando, FL 32826 Attn: Dr. Luis R. Elias Dr. I. Kimel	1 copy 1 copy
Dartmouth College 18 Wilder, Box 6127 Hanover, New Hampshire 03755 Attn: Dr. John E. Walsh	1 copy

Department of Energy Div. of Advanced Energy Projects Washington, DC 20545 Attn: Dr. R. Gajewski	1 copy
Department of Energy Office of Energy Research Washington, D.C. 20545 Attn: C. Finfgeld/ER-542, GTN T.V. George/ER-531, GTN D. Crandall/ER-54, GTN Dr. David F. Sutter/ER-224, GTN	1 copy 1 copy 1 copy 1 copy
Defense Advanced Research Project Agency/DEO 1400 Wilson Blvd. Arlington, Virginia 22209 Attn: Dr. S. Shey Dr. L. Buchanan	1 copy 1 copy
Defense Communications Agency Washington, D.C. 20305 Attn: Dr. Pravin C. Jain Assistant for Communications Technology	1 copy
Defense Nuclear Agency Washington, D.C. 20305 Attn: Mr. J. Farber Dr. Leon Wittwer (RAAE)	1 copy 5 copies
Defense Technical Information Center Cameron Station 5010 Duke Street Alexandria, Virginia 22314	2 copies
General Atomics 13-260 Box 85608 San Diego, CA 92138 ATTN: Dr. J. Doane Dr. C. Moeller	1 copy 1 copy
Georgia Tech. EES-EOD Baker Building Atlanta, Georgia 30332 Attn: Dr. James J. Gallagher	1 copy
Hanscomb Air Force Base Stop 21, Massachusetts 01731 Attn: Lt. Rich Nielson/ESD/INK	1 copy

Hughes Aircraft Co. Electron Dynamics Division 3100 West Lomita Boulevard Torrance, California 90509 Attn: J. Christiansen J.J. Tancredi	1 copy 1 copy
Hughes Research Laboratory 3011 Malibu Canyon Road Malibu, CA 90265 Attn: Dr. R. Harvey Dr. R.W. Schumacher	1 copy 1 copy
KMS Fusion, Inc. 3941 Research Park Dr. P.O. Box 1567 Ann Arbor, Michigan 48106 Attn: S.B. Segall	1 copy
Lawrence Berkeley Laboratory University of California 1 Cyclotron road Berkeley, CA 94720 Attn: Dr. A.M. Sessler	1 copy
Lawrence Livermore National Laboratory P.O. Box 808 Livermore, California 94550 Attn: Dr. D. Prosnitz Dr. T.J. Orzechowski Dr. J. Chase Dr. W.A. Barletta Dr. D.L. Bix Dr. R. Briggs Dr. E.T. Scharlemann	1 copy 1 copy 1 copy 1 copy 1 copy 1 copy 1 copy
Los Alamos National Scientific Laboratory P.O. Box 1663, MSJ 564 Los Alamos, NM 87545 Attn: Dr. Brian Newnam	1 copy
Los Alamos Scientific Laboratory P.O. Box 1663, AT5-827 Los Alamos, New Mexico 87545 Attn: Dr. T.J.T. Kwan Dr. L. Thode Dr. C. Brau Dr. R. R. Bartsch	1 copy 1 copy 1 copy 1 copy

Massachusetts Institute of Technology	
Department of Physics	
Cambridge, Massachusetts 02139	
Attn: Dr. G. Bekefi/36-213	1 copy
Dr. M. Porkolab/NW 36-213	1 copy
Dr. R. Davidson/NW 16-206	1 copy
Dr. A. Bers/NW 38-260	1 copy
Dr. K. Kreischer	1 copy
Dr. B. Danby	1 copy
Dr. G.L. Johnston	1 copy
Massachusetts Institute of Technology	
167 Albany St., N.W. 16-200	
Cambridge, Massachusetts 02139	
Attn: Dr. R. Temkin/NW 14-4107	1 copy
Spectra Technologies	
2755 Northup Way	
Bellevue, Washington 98004	
Attn: Dr. J.M. Slater	1 copy
Mission Research Corporation	
Suite 201	
5503 Cherokee Avenue	
Alexandria, Virginia 22312	
Attn: Dr. M. Bollen	1 copy
Dr. Tom Hargreaves	1 copy
Dr. J. Pasour	1 copy
Mission Research Corporation	
1720 Randolph Road, S.E.	
Albuquerque, New Mexico 87106	
Attn: Mr. Brendan B. Godfrey	1 copy
SPAWAR	
Washington, D.C. 20363	
Attn: E. Warden	
Code PDE 106-3113	1 copy
Capt. Fontana	
PMW 145	1 copy
Naval Research Laboratory	
Addressee: Attn: Name/Code	
Code 1000 - Commanding Officer	1 copy
Code 1001 - T. Coffey	1 copy
Code 1200 - Capt M.A. Howard	1 copy
Code 1220 - Security	1 copy
Code 2628 - TID Distribution	22 copies
Code 4000 - W. Ellis	1 copy
Code 4000 - D. Nagel	1 copy
Code 4700 - S. Ossakow	26 copies

Code 4700.1 - A.W. Ali	1 copy
Code 4710 - C. Kapetanakos	1 copy
Code 4740 - Branch Office	25 copies
Code 4740 - W. Black	1 copy
Code 4740 - A. Fliflet	1 copy
Code 4740 - S. Gold	1 copy
Code 4740 - A. Kinhead	1 copy
Code 4740 - W.M. Manheimer	1 copy
Code 4740 - M. Rhinewine	1 copy
Code 4770 - G. Cooperstein	1 copy
Code 4790 - B. Hui	1 copy
Code 4790 - C.M. Hui	1 copy
Code 4790 - Y.Y. Lau	1 copy
Code 4790 - P. Sprangle	1 copy
Code 5700 - L.A. Cosby	1 copy
Code 6840 - S.Y. Ahn	1 copy
Code 6840 - A. Ganguly	1 copy
Code 6840 - R.K. Parker	1 copy
Code 6840 - N.R. Vanderplaats	1 copy
Code 6850 - L.R. Whicker	1 copy
Code 6875 - R. Wagner	1 copy

Naval Sea Systems Command
 Department of the Navy
 Washington, D.C. 20362
 Attn: Commander
 PMS 405-300

1 copy

Northrop Corporation
 Defense Systems Division
 600 Hicks Rd.
 Rolling Meadows, Illinois 60008
 Attn: Dr. Gunter Dohler

1 copy

Oak Ridge National Laboratory
 P.O. Box Y
 Mail Stop 3
 Building 9201-2
 Oak Ridge, Tennessee 37830
 Attn: Dr. A. England

1 copy

Office of Naval Research
 800 N. Quincy Street
 Arlington, Va. 22217
 Attn: Dr. C. Roberson
 Dr. W. Condell
 Dr. T. Berlincourt

1 copy
 1 copy
 1 copy

Optical Sciences Center University of Arizona Tucson, Arizona 85721 Attn: Dr. Willis E. Lamb, Jr.	1 copy
Physics International 2700 Merced Street San Leandro, California 94577 Attn: Dr. J. Benford	1 copy
Physical Science Inc. 603 King Street Alexandria, VA 22314 ATTN: M. Read	1 copy
Princeton Plasma Plasma Physics Laboratory James Forrestal Campus P.O. Box 451 Princeton, New Jersey 08544 Attn: Dr. H. Hsuan Dr. D. Ignat Dr. H. Furth Dr. P. Efthimion Dr. F. Perkins	2 copies 1 copy 1 copy 1 copy 1 copy
Raytheon Company Microwave Power Tube Division Foundry Avenue Waltham, Massachusetts 02154 Attn: N. Dionne	1 copy
Sandia National Laboratories ORG. 1231, P.O. Box 5800 Albuquerque, New Mexico 87185 Attn: Dr. Thomas P. Wright Mr. J.E. Powell Dr. J. Hoffman Dr. W.P. Ballard Dr. C. Clark	1 copy 1 copy 1 copy 1 copy 1 copy
Science Applications, Inc. 1710 Goodridge Dr. McLean, Virginia 22102 Attn: Adam Drobot P. Vitello D. Bacon C. Menyuk	1 copy 1 copy 1 copy 1 copy
Science Research Laboratory 15 Ward Street Somerville, MA 02143 Attn: Dr. R. Shefer	1 copy

Stanford University Dept. of Electrical Engineering Stanford, CA 94305 Attn: Dr. J. Feinstein	1 copy
Stanford University High Energy Physics Laboratory Stanford, California 94305 Attn: Dr. T.I. Smith	1 copy
Stanford University SLAC Stanford, CA 94305 Attn: Dr. Jean Labacqz	1 copy
TRW, Inc. One Space Park Redondo Beach, California 90278 Attn: Dr. H. Boehmer Dr. T. Romisser Dr. Z. Guiragossian	1 copy 1 copy 1 copy
University of California Physics Department Irvine, California 92717 Attn: Dr. G. Benford Dr. N. Rostoker	1 copy 1 copy
University of California Department of Physics Los Angeles, CA 90024 Attn: Dr. A.T. Lin Dr. N. Luhmann Dr. D. McDermott	1 copy 1 copy 1 copy
University of Maryland Department of Electrical Engineering College Park, Maryland 20742 Attn: Dr. V. L. Granatstein Dr. W. W. Destler	1 copy 1 copy
University of Maryland Laboratory for Plasma and Fusion Energy Studies College Park, Maryland 20742 Attn: Dr. Tom Antonsen Dr. John Finn Dr. Jhan Varyan Hellman Dr. W. Lawson Dr. Baruch Levush Dr. Edward Ott Dr. M. Reiser	1 copy 1 copy 1 copy 1 copy 1 copy 1 copy 1 copy

University of Tennessee Dept. of Electrical Engr. Knoxville, Tennessee 37916 Attn: Dr. I. Alexeff	1 copy
University of New Mexico Department of Physics and Astronomy 800 Yale Blvd, N.E. Albuquerque, New Mexico 87131 Attn: Dr. Gerald T. Moore	1 copy
University of Utah Department of Electrical Engineering 3053 Merrill Engineering Bldg. Salt Lake City, Utah 84112 Attn: Dr. Larry Barnett Dr. J. Mark Baird	1 copy 1 copy
Director of Research U. S. Naval Academy Annapolis, Maryland 21402-5021	1 copy
U. S. Army Harry Diamond Labs 2800 Powder Mill Road Adelphi, Maryland 20783-1145 Attn: Dr. Howard Brandt Dr. Edward Brown Dr. Stuart Graybill Dr. A. Kehs Dr. J. Silverstein	1 copy 1 copy 1 copy 1 copy 1 copy
Varian Associates 611 Hansen Way Palo Alto, California 94303 Attn: Dr. H. Huey Dr. H. Jory Dr. Kevin Felch Dr. R. Pendleton Dr. A. Salop	1 copy 1 copy 1 copy 1 copy 1 copy
Varian Eimac San Carlos Division 301 Industrial Way San Carlos, California 94070 Attn: C. Marshall Loring	1 copy
Yale University Applied Physics Madison Lab P.O. Box 2159 Yale Station New Haven, Connecticut 06520 Attn: Dr. I. Bernstein	1 copy